MICROFLUIDIC EMULSIFICATION

A Dissertation

by

PENG HE

Submitted to the Office of Graduate Studies of
Texas A&M University
in partial fulfillment of the requirements for the degree of

DOCTOR OF PHILOSOPHY

December 2011

Major Subject: Chemical Engineering

Microfluidic Emulsification

MICROFLUIDIC EMULSIFICATION

A Dissertation

by

PENG HE

Submitted to the Office of Graduate Studies of
Texas A&M University
in partial fulfillment of the requirements for the degree of

DOCTOR OF PHILOSOPHY

Approved by:

Chair of Committee,	Zhengdong Cheng
Committee Members,	Debjyoti Banerjee
	Arul Jayaraman
	Victor Ugaz
Head of Department,	Charles Glover

December 2011

Major Subject: Chemical Engineering

ABSTRACT

Microfluidic Emulsification. (December 2011)

Peng He, B.E., University of Science and Technology of China

Chair of Advisory Committee: Dr. Zhengdong Cheng

This dissertation investigates the emulsification of aqueous liquid in immiscible organic liquid in various microfluidic environments, and addresses both experimental characterization and theoretical interpretation of the dynamics and design guidelines, as well as an application of microfluidic emulsification in fabrication of disk-like colloidal particle suspensions for studying its sedimentation behavior.

In an attempt to understand the dynamics of drop formation in flow-focusing microfluidic channels, especially for an explanation of a transition from unique drop size to bimodal oscillating drop sizes as observed in the experiments, numerical simulation is developed to use the volume-of-fraction method to model the drop formation, and the simulation results help to interpret the transition in the theory of saddle-node transition in drop formation, as well as show the importance of selecting proper orifice length in flow-focusing microfluidic channel design.

The electric technique for controlling of microfluidic emulsification is explored by a detailed study on low-frequency alternating-current electro-flow-focusing (EFF) emulsification in microfluidic channels. It is found that the droplet size variation is not a monotonic function of the electric field as in the case of direct-current EFF emulsification, which originates from the relaxation oscillation of the flow rate through the Taylor cone, and a power-law droplet size distribution was obtained at the voltage ramping-up stage. This emulsification process was modeled in analog to the charge

accumulation and release in a resistor-capacitor electric circuit with an adjustable resistor, and the simulated data exhibit good agreement with the experiments.

As an application of the microfluidic emulsification, a method of fabricating disk-like wax colloidal particle suspensions using electrospray is reported. Based on this technique, the first measurement of the hindrance function for sedimentation and creaming of disk-shaped colloids via the analytical centrifugation is reported. Disks align with the external flow right above the volume fraction of a few percent and this effect is extremely sensitive to the aspect ratio of disks. Due to this alignment effect, disk sedimentation/creaming demonstrate distinct trends in dilute and semi-dilute region.

DEDICATION

To my parents.

ACKNOWLEDGEMENTS

It is a rewarding experience of pursuing my doctor degree in Texas A&M University and having Prof. Zhengdong Cheng as my research supervisor. Besides his broad knowledge in various physical and chemical subjects, his profound and keen insights into complicated problems are great and essential help for me to finish the journey of these research topics. As a good mentor, he also helps me form good habits in many aspects of personality during the graduate life which would be an invaluable and enduring memory for the future.

I want express my grateful acknowledgments to Prof. Victor Ugaz, Prof. Arul Jayaraman, and Prof. D. Banerjee for the guidance and stimulations in research; Prof. Michael Bevan and Prof. Hung-Jue Sue for the inspiring discussion; Prof. Shantz, Prof. Jeong, and Prof. Cremer for their support in experiments.

I also gracefully appreciate to current and former members of Complex Fluids Group for their helpful advices and constant contributions. Many thanks to Dr. Gang Liang and Dr. Orla Wilson for their technical assistances at Material Characterization Facility; Dr. Inho Lee, Dr. Richard Beckham, Dr. Dazhi Sun, Dr. Qingsheng Wang, Dr. Xin Qu, Dr. Zuyi Huang, Dr. Xiaole Wang, and many other friends for their help. I want to express sincere gratitude to Dr. Jingyi Shen for her spiritual advice and practical guidance.

Finally, thanks to my parents for their encouragement and support, and to my wife, Weiwei Wang for her patience and love.

NOMENCLATURE

AC	alternating current
CFD	computational fluid dynamics
DC	direct current
DLVO	Derjaguin-Landau-Verwey-Overbeek
EFF	electro-flow-focusing
ES	electrospray
FF	flow focusing
PDMS	polydimethylsiloxane

TABLE OF CONTENTS

Page

LIST OF FIGURES

FIGURE Page

FIGURE Page

FIGURE Page

LIST OF TABLES

1. INTRODUCTION

1.1. Microfluidic Emulsification

The rapidly increasing interest in the application of miniaturization of chemical and biological instrumentation motivates the developments of highly integrated "lab-on-a-chip" systems [1-15]. One of the most exciting scientific developments of recent years is the microfluidic system, which provides many advantages compared to conventional industrial laboratory equipment. The “dreams” used to appear in the scientific fictions have become true that on stamp-sized devices highly integrated addressable channel networks with various functionalities can be created in an unprecedented automation. The reduced size in the microfluidic systems makes them suitable for mobile laboratories, while the reduced cost allows them to be disposable after many sensitive tests. Microfluidic systems also give new problems to the well-studied topics in fluid dynamics [13, 16-22], since the very small scales makes it very sensitive to the surface properties and the interplay of multiple physical effects become significant such as pressure gradients and capillarity.

Microfluidics has emerged as a cutting-edge technique featuring its capability of manipulating small amount of fluids (10^{-9} to 10^{-18} liters) [15]. A typical microfluidic chip consists of microchannels (1 to 100 μm in diameter) in connection with large pools of liquid supply, driven by syringe pumping system, and integrated with sensors and valves for dynamic control.

The microfluidic chip offers a variety of means of handling small volumes, filtering, synthesis, and high-sensitive analysis. Upon scaling-down and optimization, the conventional system could be entirely miniaturized onto a micro-scale chip and performed in a parallel manner, hence greatly increases the processing speed.

This dissertation follows the style of *Physical Review Letters.*

Microfluidic system only needs a small aliquot of sample in the operation. This inherent merit makes microfluidic a natural partner to chemistry and biology where a large quantity of sample is either too expensive or inaccessible. For example, in drug discovery, these microsystems offer reduced reagent consumption, high sample throughput and rapid chemical kinetics. It is also possible to mimic the *in vivo* microenvironment of cells in microfluidic channels by patterning the cells and/or culture medium in 2D or 3D structure [5]. This will help to improve the prediction of *in vivo* cell functions using the *in vitro* cell experiments.

One catalyst for the rising of microfluidics is molecular and cell biology. There are great demands for analytical methods with higher throughputs, higher sensitivity and resolution than the conventional methods. A revolution in these directions could greatly benefit many fundamental techniques in drug discovery, e.g., high-throughput screening, bioanalysis, single-cell manipulations, and toxic tests.

Microfluidics, in particular the PDMS-based (PDMS: Polydimethyl-Siloxane) microfluidics, offers a natural fit to these demands. PDMS-based devices currently dominate the study in microfluidics. On one hand, it is easy to design and fabricate PDMS devices, and the cost of materials and equipment is relatively low (e.g., cleanroom is not necessary) compared to other microfabrication approaches. On the other hand, PDMS has an outstanding optical transparency, a low toxicity to biomolecules, and a high permeability to oxygen and carbon dioxide, thus it is an ideal culture medium to be applied for cell growth, perturbation, and observation. Therefore, PDMS-based microfluidic devices have gained large popularity, and a lot of advances have been made towards biological applications.

The microfluidic devices could be utilized to improve the conventional well-plate system to achieve the high-throughput cell-arrays [23, 24]. A scalable experimental platform combining the microfluidic addressability with quantitative fluorescent imaging has been developed to obtain real-time characterization of gene expression in living cells. This approach could analyze hepatic inflammation by acquiring ~5000 single-time-point

measurements in each automated experiment [23]. Besides the bulk experiments in cell behavior study, single cell manipulations (e.g., trapping, releasing, separation, and sorting) have been invented, and single cell arrays have been demonstrated as well. A microfluidic bioreactor has been implemented to conduct a long-term observation and to regulate the bacteria behavior via the feedback from the bacteria population [25]. Combinations of optical detecting and optical trapping techniques with microfluidics also have their unique value. Optical tweezers could trap and move individual cells inside the microfluidic channels and enable the study of rapid cytological responses of living cells with respect to the environmental changes. Because the trapped cells are not in physical contact with the apparatus, this method allows a contaminant-free working condition owing to the reduced disturbance [26, 27].

Cell culture patterning is another cutting-edge topic in microfluidics. With cell culture medium patterned in 3D structures, it is promising to produce artificial extra-cell-matrix (ECM) and mimic in vivo cell microenvironment. The mimic microenvironment will be crucial to improve the prediction of drug functions in human body by *in vitro* experiments [28]. Scanning confocal or conventional fluorescence microscopy could be used to polymerize the photocurable materials delivered into a microfluidic channels, and monolithic 3D structure could be fabricated and spatially aligned using tens of different materials [29]. Another impressive experiment comes from UC Berkeley where ordered single cell array is achieved without chemical treatment of surfaces [30]. The cells were loaded by flowing into microfluidic channels, and then trapped and protected from shearing force by arrays of molded PDMS wells. Cell-cell communications by contact or diffusion are controllable in this device, and single cell study of metabolism and drug toxicity could be facilitated (see **Figure 1**).

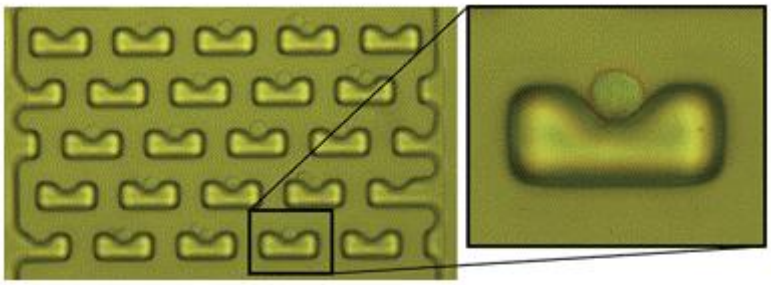

Figure 1 Single-cell array of molded PDMS wells for biological study [30]. Reproduced by permission of The Royal Society of Chemistry.

Materials other than PDMS have also been exploited for their potential significance in biology. One example is a recirculation flow system that is developed to accelerate the DNA microarray hybridization in a microfluidic device made of laminating Mylar and glass [31]. Microfluidic channels can be integrated with semiconductor to create a compact disposable optical-trapping microchip [32]. Electromagnetic field is also a powerful tool for manipulating living cells. For example, prototype of single molecule sorting and steering is realized with electrical field on silica substrate [33]. Hybrids of microfluidic channel and CMOS (Complementary Metal–Oxide–Semiconductor) chip bring the speed and programmability of IC (Integrated Circuit) chip to biology and aim to produce a universal cell manipulator (**Figure 2**) [34]. One drawback of the PDMS devices is their swelling in common chemical solvents, which hinders their applications in organic chemical synthesis. One counterpart is a solvent-resistant microfluidic DNA synthesizer based on PFPE (Per-Fluoro-PolyEther) [35]. Although only a small batch of DNA was produced in the preliminary experiment, it is hopeful to be combined with other biochemical amplification methods to realize the whole gene synthesis, sequencing and screening on a single chip.

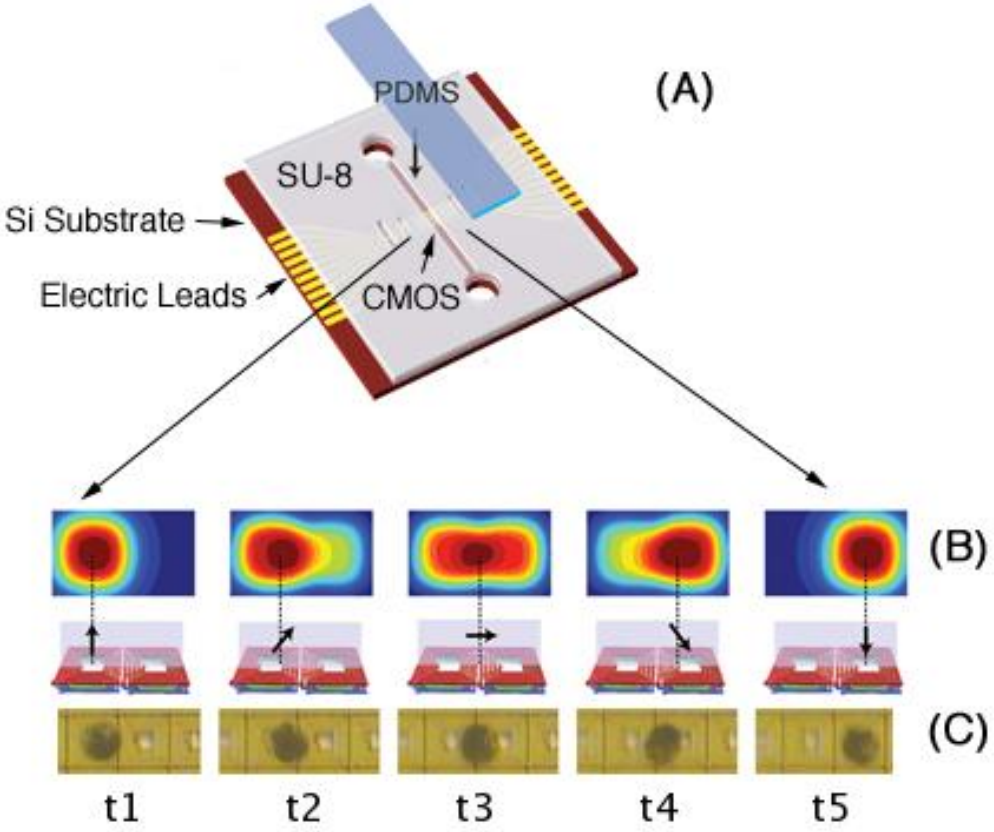

Figure 2 CMOS/microfluidic hybrid cell manipulator. (A) Schematic. (B) Time-dependent magnetic field patterns, arrows showing force direction. (C) A single magnetically tagged cell is trapped and moved using the magnetic field [34]. Reproduced by permission of The Royal Society of Chemistry.

Generating a stable concentration gradient of desired chemicals is an important step for various applications in chemistry and biology, especially for the study of chemotaxis and the toxic test of cell responses in drug discovery. Due to the intrinsic laminar flow characteristic inside microfluidic channels, the convective transport of chemicals along the channel is much faster than the diffusive transport across the channel width. Hence, the microfluidic channel is an ideal tool to generate and maintain stable concentration gradients.

The simplest way to create a concentration gradient is to flow solutions of different concentrations simultaneously into the microchannels at the same speed. The side-by-side streams will establish a stable concentration gradient that will not be disturbed by the diffusive flux in a relatively long distance. While some successful applications have been made in this fashion, it will always produce sigmoidal concentration profiles, and be sensitive to the flow speed and the position along the channels. The Whitesides group at Harvard has introduced a successful device getting around these difficulties [36]. The key is to use a gradient-generating network of microchannels that typically has a pyramidal shape. The network is fed with two source solutions that are split and delivered to the outlet in N streams forming a concentration profile. This pyramidal network was later modified to deliver complicated shapes, such as exponential, linear or parabolic profiles [37]. In the modified design, the number of splitting-and-mixing stages only logarithmically increases with the number of scales in the outlet gradient, with respect to a linear increase of stages with the number of scales in the original "Harvard" design. Thus, the modified design allows a much more compact array and provides a better gradient resolution. The chemical gradient can also be applied to pattern biomolecules (e.g., proteins, oligonucleotides, artificial polymers) on surfaces (**Figure 3**) [38]. This method could be useful to immobilize the biomolecules, to study the migration and polarity of cells, and to help screening the phenotypes.

Emulsions are usually produced in a mixture of two immiscible fluids, where one substance (the dispersed phase) is suspended in the other (the continuous phase) as droplets. In macroscopic systems, emulsions are typically formed either by mechanical agitation or strong shearing viscous stress on the dispersed fluid in mixers. However, such resulting emulsions usually suffer from a wide size distribution.

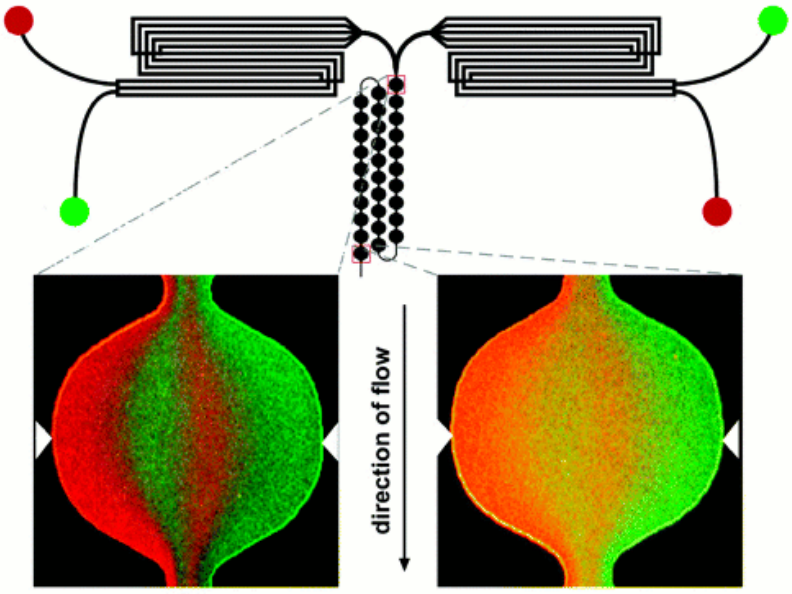

Figure 3 Chemical gradient generated in microfluidic networks [38]. Reprinted (adapted) with permission from X. Jiang *et al.*, *Anal. Chem.* **77**, 2338 (2005). Copyright (2005) American Chemical Society.

The formation of droplets inside microchannels is a unique component in microfluidics. It extends the continuous flow in microfluidics to a discrete manner and permits additional controls and manipulations on the sample liquid. It could be a powerful tool to improve the current techniques, e.g. cell-arrays [10, 24, 30], mass spectroscopy [39], protein crystallization [38], micro-mixers and micro-reactors in organic synthesis [40]. Since the development of soft-lithography [41, 42] and flow-focusing technique [43], it has been very simple for people to generate uniform droplets in nanoliter size in a frequency as high as kHz.

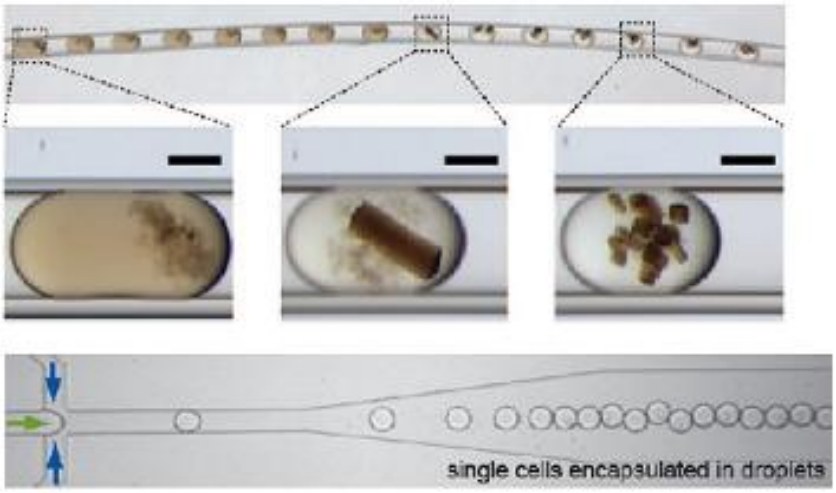

Figure 4 Examples of various droplet-based microfluidic systems [12, 44, 45]. With kind permission from Springer Science+Business Media: "Engineered 3D tissue models for cell-laden microfluidic channels", Y. S. Song et al., Anal. Bioanal. Chem. **395**, 185 (2009).
.

These small droplets are perfect candidates for micro-reactors (e.g. see **Figure 4**). Their high surface-to-volume ratio allows a very rapid thermal transfer while their tiny size permits a very fast mixing (usually in a zigzag channel or electrical field) promoting a homogeneous micro-environment for chemical reactions. Furthermore, in the steady laminar flow along the microchannels that is typical in microfluidics, the position of each individual droplet exactly corresponds to an individual time point, labeling the residence time since the mixing or reaction started as the droplet was formed. Naturally, observing the temporal variation of a reaction can be done in space. The kinetics of the whole reaction can be obtained at a single time. This kind of experiment has been performed in a matter of a few milliseconds. Another interesting example is the Phase Chip [46]. It includes many distinct components that can controllably vary the amount of water inside droplet and thus adjust the solute concentration. Protein crystallization rates are enhanced inside the manipulated droplets, as well as the kinetics of nucleation and growth through. These novel techniques and applications express the advantage of droplet-based microfluidics on chemical analysis and protein crystallization.

Early experiments of droplet-based microfluidics only applied simple regulations on the flows and droplets, thus the droplets moved passively in the flow field, where their motions were basically controlled by the channel network geometry for the most of the time. To realize complex microfluidic platforms that eventually lead to the total analysis system and micro-factory on-chip, people are seeking versatile means to integrate compact and effective control modules into microfluidic systems, e.g., using electrical field to manipulate or separate droplets [39, 47, 48]. Previously, novel designs and regulations in microfluidic platforms were mainly based on intuition and trial-and-error. As more and more components are integrated into the system, the complexity exponentially increases and the mass-production in microfluidic platforms calls for standardization and modularization of individual components. In recent years, the theoretical study and computational simulation in microfluidic channels rapidly increase [49-51], which will pave the way to the rapid development and optimization of microfluidic networks for industrial applications.

Besides the adjustment and external confinements on the microfluidic channels, new research opportunities could also come from the droplets themselves. Compared to the continuous flow, the plenty of interfaces present in the emulsions is a special characteristic in the droplet-based microfluidics. By tailoring the surface property of the droplets, a large number of new features could be assigned to the multi-phase emulsion systems (e.g. see **Figure 5**). Uniform double and triple emulsion droplets have be generated using a clever design in microcapillary device [45, 52]. The core-shell geometry of these multiple emulsion droplets provides various useful utilizations, such as producing microcapsules to protect the living cells or building microstructure to mimic the in vivo environments.

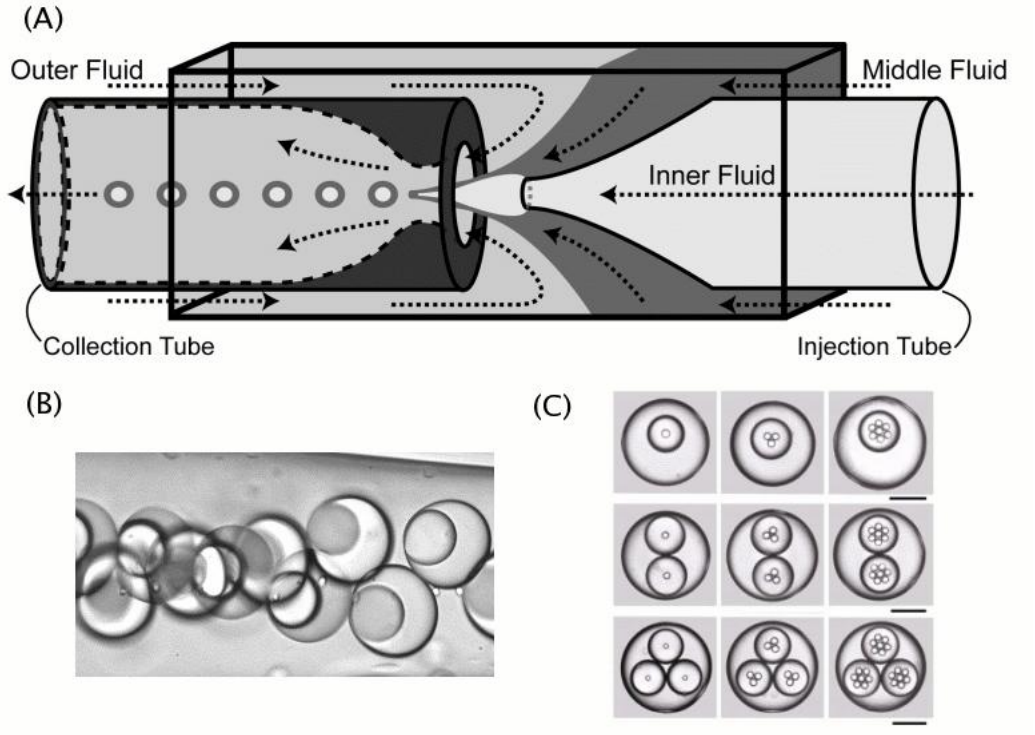

Figure 5 Multiple-emulsion capillary device. (A) Geometrical setup. (B) Double emulsion droplets [45]. Reprinted with permission from AAAS. (C) Triple emulsion droplets [52]. Reprinted with permission from Cambridge University Press.

Extensive studies have been dedicated to examine the physics behind droplet formation. The most common example of immiscible fluids is oil and water. If water is dispersed within an external oil phase, suspensions of small emulsions will form, however minimization of surface energy in a closed system will promote coalescence of distinct droplets on contact into one continuous volume [1]. A suspension of stable emulsions may be created by the use of an emulsifier or stabilizer, which is typically some form of surfactant, whose molecules have a water-soluble (hydrophilic) head and an organic-soluble (hydrophobic) tail. Stabilizers work to sufficiently lower the surface tension forces at the emulsion boundary compared to the external viscous forces. This barrier against coalescence permits the emulsion to persist long after the shear has been stopped

and gives rise to many important products such as foods, cosmetics, and paints. The stability and dynamics of droplet behavior in viscous mediums have been extensively reviewed, most notably by Stone [13]. Physics of emulsion formation mechanisms and resulting size distributions have been studied extensively [1, 13, 15, 47]. Some important dimensionless numbers are summarized in **Table 1**.

Table 1 Comparison of common dimensionless numbers in the study of emulsification process. The meaning of parameters: a−characteristic length, ρ−density, U−characteristic velocity, μ−viscosity, k_B−Boltzmann constant, T−temperature, σ−surface tension, and g−gravitational acceleration (of earth).

$\frac{\text{inertial force}}{\text{viscous force}}$	$\frac{\rho a^2 U^2}{\mu U a} = \frac{\rho U a}{\mu}$ (Reynolds number)
$\frac{\text{viscous force}}{\text{Brownian force}}$	$\frac{\mu U a}{k_B T / a} = \frac{\mu U a^2}{k_B T}$ (Péclet number)
$\frac{\text{inertial force}}{\text{surface tension force}}$	$\frac{\rho a^2 U^2}{\sigma a} = \frac{\rho U^2 a}{\sigma}$ (Weber number)
$\frac{\text{viscous force}}{\text{surface tension force}}$	$\frac{\mu U a}{\sigma a} = \frac{\mu U}{\sigma}$ (Capillary number)
$\frac{\text{viscous force}}{\sqrt{\text{inertial} \bullet \text{surface tension force}}}$	$\frac{\mu U a}{\sqrt{\rho U^2 a^2 \bullet \sigma a}} = \frac{\mu}{\sqrt{\rho \sigma a}}$ (Ohnesorge number)
$\frac{\text{gravitational force}}{\text{surface tension force}}$	$\frac{a^3 g \Delta\rho}{\sigma a} = \frac{a^2 g \Delta\rho}{\sigma}$ (Bond number)

Microfluidics enables precise manipulation of fluids at small length scales, and presents opportunities to control and apply emulsification processes to problems in biology and manufacturing. Microfluidic devices have been fabricated to generate stable monodisperse emulsions that can be used for nanoscale synthesis of proteins and assembling inorganic matrices for drug delivery. Within these devices, pressurized immiscible fluids may be combined at a junction of two or more microchannels, combining crossflow and viscoelastic shear to rapidly generate droplets at regular periodicity. The pioneering work in this field has demonstrated that spatial and temporal instabilities in immiscible fluid systems at small length scales may lead to the controlled formation of dynamic, metastable droplet patterns. The size of droplets in microfluidic systems may range from nanometers to microns in diameter, and can be controlled by device geometry and hydrodynamic flow characteristics. Production is very rapid ($\sim 10^2$ -10^4 Hz in single nozzle devices) and droplet sizes are consistent (variation on diameter ~2-5%).

In the area of pressure-driven microfluidics, an extension of Stoke's analysis to a spherical drop or bubble carried by an immiscible fluid is given by the drag force. For bubbles or drops, the shear stress on the surface induces an internal motion, which results in a decrease of the drag coefficient. Equivalently, in the droplet-based microfluidic systems, this recirculation can be exploited in micromixers and discrete chemical reactors [53]. Since each droplet functions as a batch reactor moving along a channel, the reaction time corresponds to the length traveled by the droplet. Consequently, sampling of droplets at different spatial locations can be used to deduce chemical kinetics, provided that the local micromixing is faster than the chemical reaction rate. Recent interest in microfluidic emulsion technology has focused on the physics of droplet formation, the application of droplets for particle manufacturing, and droplet manipulation techniques.

Important researches of microfluidic emulsion technology are briefly reviewed, as an introduction to this field. Using a "T" junction layout, Ismagilov et al. [44, 54] have

adapted a crossflow microfluidic device design as a basis for many droplet based research performed to combine multiple fluid reagents into single droplets for use as microreactors. A few of the notable studies include: the production studies to explore the effects of at varying Reynolds and Capillary numbers of the continuous phase, as well and the effects of mixing efficiency as a function of viscosity, in the generation of droplets [18, 55, 56]. Higuchi et al. [57] have adapted the analysis of Thorsen [4, 14] to consider the effects of various continuous and emulsified flow rates in polymethyl methacrylate (PMMA) plates with etched microchannels networks. They manufactured serial junctions to get double emulsions (water in oil in water emulsions, or vice-versa). A crucial technique required for the success of microfluidic double emulsion is the selective modification of hydrophobic channel surfaces into hydrophilic ones, in order to allow inverse oil-in-water droplets to be formed. Seki et al. [58, 59] demonstrated a rapid emulsification device to produce droplets in very good size uniformity using etched parallel groves in silicon devices aligned with a drop-off ledge. Anna et al. [43] considered the many droplet production modes available at various liquid-liquid flow rates through an inline flow-focusing device.

The early experiments of microfluidics only applied simple regulation on the flows and droplets, thus the droplets move passively in the flow field for most of the time. This is dominantly controlled by the channel network geometry. To realize complex applications in microfluidic channels that eventually lead to the total analysis system and micro-factory on-chip, people are seeking versatile means to integrate compact and efficient controls into microfluidic systems, e.g. using electrical field to do the manipulation or separation of droplets. The control of local mixing, droplet movement and droplet residence time distributions creates additional opportunities for applications in materials synthesis, in particular for continuous particle self-assembly. The ability to control transport, merging, and splitting of drops affords the opportunity to realize programmable systems for studying and implementing reaction networks hydrodynamically controlled systems. Link et al have designed channel networks and features to allowing geometrically mediated breakup of large droplet plugs into smaller

ones [48, 60]. Lee et al. [34, 61] have designed various channel geometries to achieve control of high- speed droplet fission, fusion, sorting, and rearranging in the microfluidic networks, including channels to trap problematic satellite droplets. Electro-hydrodynamics may be used to manipulate droplets, as an alternative to the previously discussed pressure or flow rate controlled systems. Microelectrode arrays with programmed electric fields create dielectrophoretic and electrowetting forces transporting droplets, merging droplets, and splitting droplets in microfluidic equivalents of microprocessors [39]. Several researchers using electro-hydrodynamic (EHD) forces, most importantly Ward et al. [62], Xuan et al. [63], and so on, have been investigating the use of incorporated electrodes and use of local electrical fields in microfluidic devices to "digitally" generate and manipulate individual emulsions.

Previously, novel designs and controls in microfluidic platform are mainly based on trial-and-error and intuition. As more and more components integrated into the system, the complexity exponentially increases and the mass-production in microfluidic platform calls for standardization and modularization in the individual components. In recent years, the theoretical study and computational simulation in microfluidic channels rapidly increase. These theoretical and numerical approaches will pave the way to rapid development and optimization of microfluidic networks for industrial applications.

Besides the adjustment to the microfluidic channels and external confinement, the new research opportunities could also comes from the droplets themselves. Compared to the continuous flow, the existence of interfaces in the emulsions is a unique characteristic in droplet-based microfluidics. By tailoring the surface properties of the droplets, many new features could be assigned to the multi-phase emulsion systems. Uniform double emulsion droplets could be generated using a microcapillary device [64]. The core-shell geometry of these double emulsion droplets provides various useful applications, such as building microcapsules to protect the living cells or microstructure to mimic the *in vivo* environments.

Microfluidic emulsion technology has been adapted to the manufacture of monodisperse microspheres. Using the microfabricated parallel channel approach, Seki et al. have generated polymeric microspheres, with excellent monodispersity and surface quality, for use as liquid crystalline spacers [58]. They also adapted a solvent evaporation process in conjunction with the microchannels droplet generator to produce lipid microspheres, where evaporation of hexane from produced microspheres was used to reduce particle diameter in the final product. Xu et al. [65] have used microfluidic flow focusing to generate a variety of particle shapes from acrylate, through the dynamic curing of those liquid droplets,

The advantages in microfluidic technologies can also be utilized for the fabrication of non-spherical particles. One approach to fabricate particles in a microfluidic device is based on the capability of manipulating tiny volume of fluid in microchannels. Droplets are formed in the microchannels first as precursors for the final particles. Microfluidic channels can be designed in different sizes and shapes, to render the corresponding non-spherical shape to the colloidal particles [66]. Another approach is the combination of lithography and photochemistry to form non-spherical polymer particles [67]. Typically, a photo-mask with the desired patterns of particle shape is used as a template for the final polymer particles, which are formed by UV-initiated photo-polymerization of the monomer that flows periodically or continuously in the microfluidic devices. 2D and 3D polymer particles of desired shapes can be fabricated using this approach. A limiting factor of the photo-polymerization method is that for particles to be generated continuously at a high production rate, the photo-polymerization reaction has to be fast, restricting the use of the approach to a limited choice of materials.

1.2. Colloidal Suspensions

The term colloid originates from the Greek word “κολλα” meaning glue. In the 19th century, Thomas Graham coined this term to classify a type of matter which forms a dispersion or suspension, in contrast to a homogeneous solution when dissolved in a solvent. In several ways, colloidal dispersions show differences from real (homo-

geneous) solutions. Colloidal particles retain their identity in a suspension, while in a real solution, the solute usually no longer possesses its identity, e.g., when a salt is dissolved in water, the composition of the salt dissociates into anions and cations, and substantially change in property. Therefore, a colloidal suspension is a heterogeneous system.

Colloids generally refer to particles in size range of 1 nm to 10 μm (10−9–10−5 m), substantially larger than atoms or ordinary molecules so that the finer material structures can be ignored, but still small enough to exhibit Brownian motions. More broadly, any substance, including thin films and fibers, with at least one dimension in this general size range, can fall into the category of colloids. Colloidal systems often exist as dispersions of one material in another continuous phase, for example, solids in air like smoke particles, liquid in liquid like milk, or gas in liquid as the beer foams. A summary of the common colloidal systems is represented in **Figure 6**, and more detailed descriptions can be found in the prestigious textbook “Colloidal Dispersions” [68].

1.2.1. Historical Perspective

Colloidal systems have been observed and studied since about the seventeenth century, when alchemists produced sols using gold chloride solutions with reducing agents. One of the most groundbreaking observations of the colloidal behavior in a suspension is the Brownian motion, observed by Robert Brown (1773–1858) who studied the jiggling motion of particles in pollen grains suspended in water under a microscope. However, the molecular basis of Brownian motion was not settled until the early 20th century. Albert Einstein published his theoretical explanation of Brownian motion in terms of atoms [69].

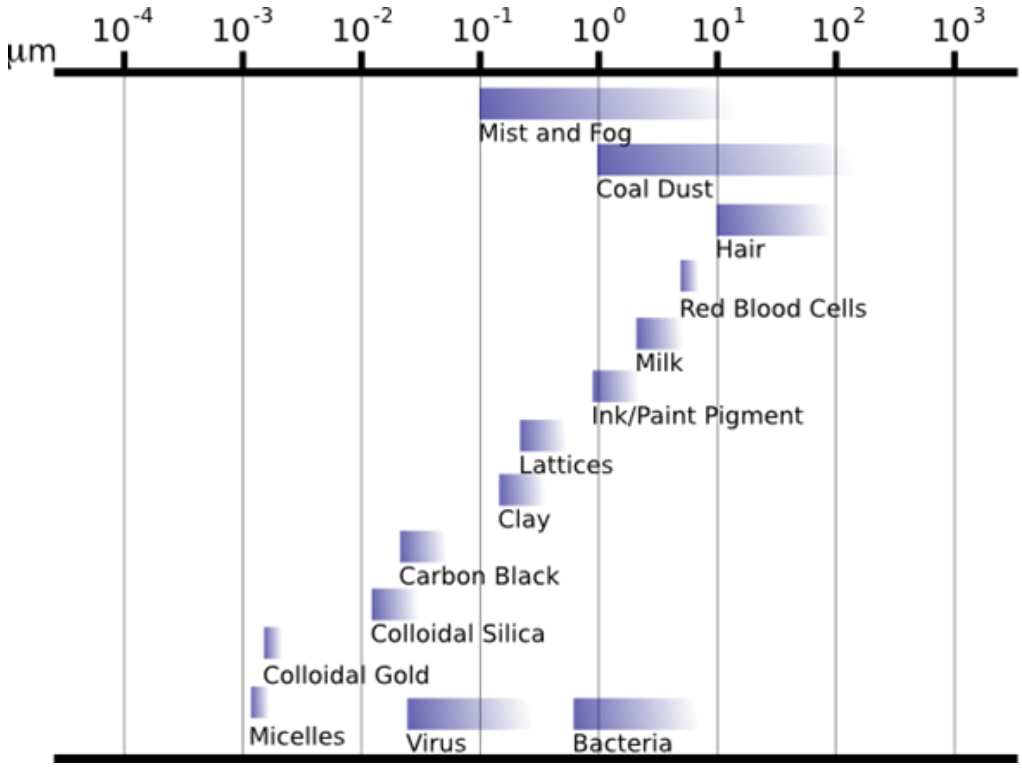

Figure 6 Scale chart of typical particle sizes in the colloidal domain [68, 70].

Simply speaking, Einstein estimated the Brownian motion of the particle, more specifically the root mean square displacement $\langle \Delta r \rangle$ as:

$$\langle \Delta r \ t \ \rangle = \sqrt{6Dt} \tag{1.1}$$

where t is the elapsed time and D is the diffusion coefficient. At a given temperature T, the diffusion coefficient can be determined as:

$$D = \frac{k_B T}{6\pi\eta a} \tag{1.2}$$

where k_B the Boltzmann's constant, η is the viscosity of the continuous phase fluid, and a is the radius of the spherical particle. After Einstein's theory, Perrin did the experimental work to test and verify Einstein's predictions (**Figure 7**), which is

summarized in his book “Brownian Motion and Molecular Reality” [71, 72]. Besides the observation of random diffusion of colloidal particles during Brownian motion, Perrin also verified the equilibrium concentration profile of dilute colloidal suspensions in gravitational field,

$$N\ Z\ \propto e^{-\frac{mgZ}{k_B T}} \tag{1.3}$$

where m is the mass of the colloidal particle, and Z is the height. The direct measurement of $N\ Z$ leads to the determination of Boltzmann's constant k_B, and eventually gives the value of Avogadro's constant N_A through the formula $k_B = R / N_A$ with the known value of ideal gas constant *R*. Einstein and Perrin's work actually showed that the particle motion can be predicted directly from the kinetic model of thermal equilibrium, and they solved the century-long dispute about John Dalton's atomic theory. Both of them earned the Nobel Prize of physics due to their work in the colloidal area.

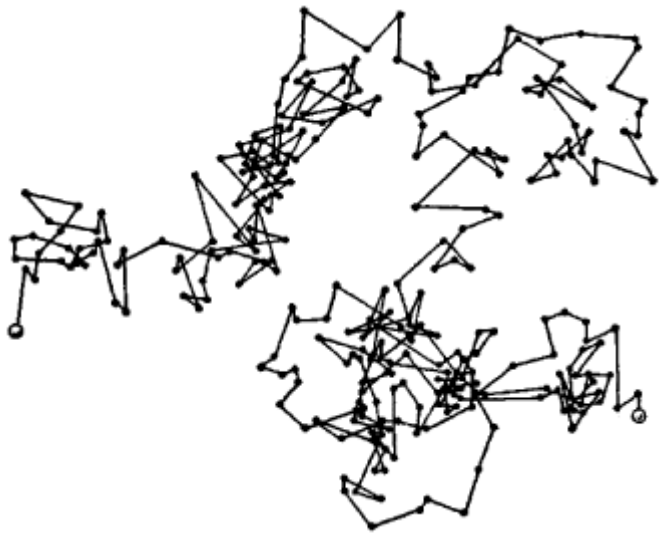

Figure 7 Tracings of the motion of colloidal particles under the microscope.

Besides the dynamics of colloidal systems, the interactions among colloidal particles are also the active topics in the last several centuries. The discovery of natural charges on colloidal particles can be dated back to early 19th century, when people observed the motion of clay particles in an electric field. Hardy [73] explained the coagulation effect of in colloidal suspensions, in which the added electrolytes suppress the effect of the charges on colloids, hence induced the aggregation. This work revealed the important connection between the stability of aqueous colloidal dispersions and the electrostatic repulsion. The theory for the screening of surface charge in the diffuse layer of counter-ions was presented by Gouy [74] and Chapman [75], in which they further attributed the thickness of the diffuse layer to the ionic strength of the solution. Smoluchowski provided the renowned formula for the surface electric potential [76], more appropriately the zeta (ζ) potential with respect to the electrophoretic mobility:

$$\mu = \frac{\zeta \varepsilon}{\eta} \tag{1.4}$$

where μ is the electrophoretic mobility, ε is the electric permittivity of the liquid and η is the viscosity.

After formal theoretical interpretation of colloid stabilization via the electrostatic repulsion formal in the early twentieth century, scientists continued on the investigation of the nature of the electrostatic force that causes destabilization of colloids and subsequent flocculation. The theory developed by Hamaker [77] obtained the attractive van der Waals interactions between colloidal particles by pairwise summation of the fundamental atomistic (Lennard-Jones) interaction potentials. This led to the representation of the total inter-particle interaction potential as the sum of the attractive van der Waals and the repulsive electrostatic interactions. After Hamaker's work, the first formal theory of colloidal stability was presented independently by Derjaguin and Landau [78] in the Soviet Union, and Verwey and Overbeek [79] in the Netherlands, during and after the World War II. The DLVO theory, named after these four scientists,

forms the basis of modern theoretical colloid science, and remains a cornerstone for theoretical elucidation of colloid transport phenomena.

1.2.2. Colloidal Phenomenon

Colloidal systems are characterized with small length scale but large ratio of surface area to volume. Generally speaking, for the spherical particles of diameter d, as the particle becomes smaller, the surface area per unit volume of the particle increases as $6/d$. Thus, in colloidal systems, not only the standard body forces, but also the surface forces become important. Due to the dominant surface forces, a special class of phenomena is related to the colloidal systems, which are often termed "colloidal phenomenon". Hence, it is important to study the interactions among the surfaces of dispersed particles or at the interfaces between the dispersed phase and the dispersing medium. In the following sections, the effect of shape and particle-particle interaction will be briefly discussed regarding to the subjects of this thesis.

Depending on their shape, colloids are usually categorized either as isotropic or anisotropic. Isotropic colloids usually refer to spherical colloids with homogeneous functionality, which are one of the ubiquitous types in nature. It is easy to synthesize in the laboratory, and also convenient to predict and analyze in theory. Many methods have been developed by researchers to synthesize ordered structures of spherical colloids with accurate control. The characterization and dynamics of spherical suspensions are also extensively measured. Anisotropy of colloidal particle is often referred to the heterogeneity of either shape or functionality of the particle [80]. Anisotropy introduced due to shape heterogeneity is often known as anisometricity, and the common examples includes colloidal rods, fibers, ellipsoids and disks etc. (see **Figure 8**) The anisometricity of colloids gives them more dynamic degrees of freedom than spherical colloids, causing the change in the interaction between these colloids with their surroundings as well as the inter-particle forces. Not only the structure but the rheology and dynamics of the colloidal suspensions are also greatly dependent upon the shape and degree of anisometricity of the colloidal particles.

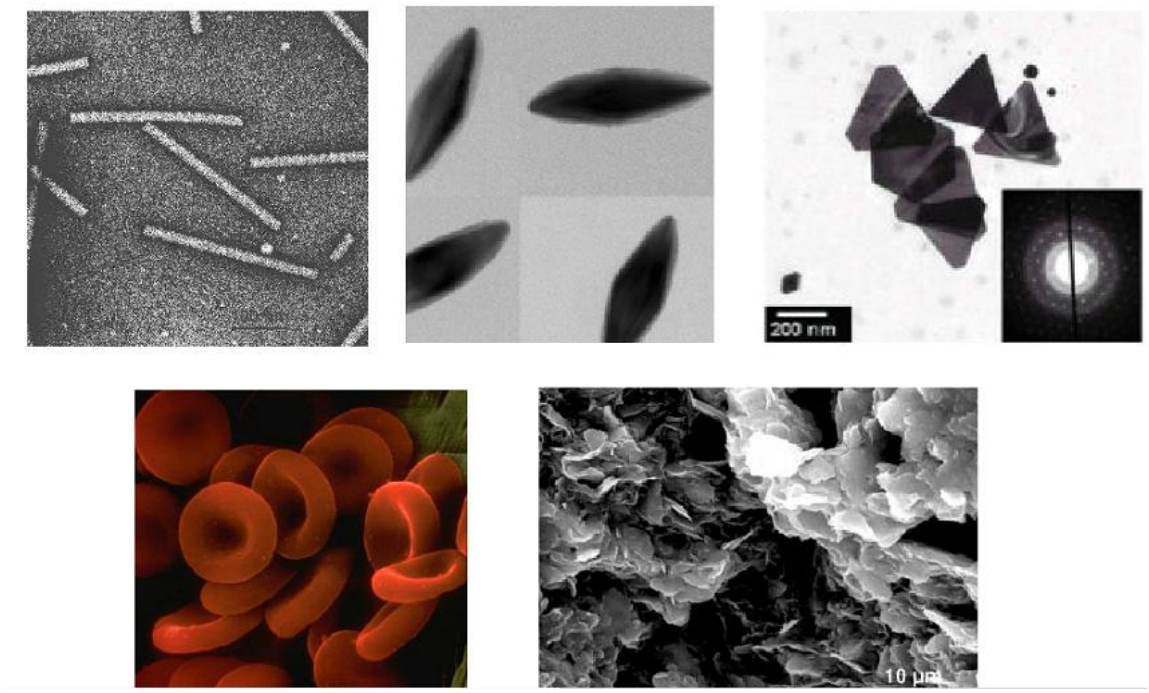

Figure 8 Examples of anisotropic colloids. (a) tobacco virus [81]. Reprinted with permission from AAAS. (b) pyramid-shaped gold nanoparticles[82]. Reprinted (adapted) with permission from V. F. Puntes, D. Zanchet, C. K. Erdonmez, and A. P. Alivisatos, J. Am. Chem. Soc. 124, 12874 (2002). Copyright (2002) American Chemical Society. (c) triangular nanoparticles[83]. Reprinted with permission from AAAS. (d) human red blood cells[84]. With kind permission from Springer Science+Business Media: " Blood Cell Interactions and Segregation in Flow", Y. S. Song et al., L. L. Munn, and M. M. Dupin, Ann. Biomed. Eng. 36, 534 (2008). (e) clays[85]. Reprinted from " Revised state diagram of Laponite dispersions" P. Mongondry, J. F. Tassin, and T. Nicolai, J. Colloid Interface Sci. 283, 397 (2005), with permission from Elsevier.

Rod-shaped colloids are the most studied anisotropic colloids. For colloidal rods the anisometricity is usually measured by the aspect ratio of the rod, i.e. the ratio between the length and the diameter. Studies of colloidal rod suspensions have indicated that rods can assemble into structures that cannot be found for spherical colloidal suspensions, such as the bundle during the fiber settling. Unlike spheres which required high volume fraction to maintain a networked structure, at low volume fractions rods can make gel structures. In the study of dynamics for colloidal rod gels, it was observed that rod-gels

with higher aspect ratios showed restrained dynamics compared to smaller aspect ratios [86]. Rods can assemble into liquid crystal structures, too, with interesting optical properties [87]. In the study of intrinsic viscosity in the rods suspensions, it is found that at a particular shear rate the intrinsic viscosity decreases with increasing aspect ratios [88].

One benefit of colloidal system above molecular systems is that colloids can be easily observed using optical microscopy, and directly manipulated, due to the relatively large size and slow moving speed. Their interactions can be easily adjusted, and the phase behavior of colloids is hence altered by the intrinsic interactions between them. Typical forces present in colloidal suspensions include gravitational, diffusive, electrostatic, and hydrodynamic [68]. Many factors may have impacts on these forces, such as particle size and shape, surface charge, ambient temperature, and so on. The physical state of the suspensions is thus dictated by the characteristics of the particle-particle interactions, switching from fully random dispersed to long-range ordered. The concentration of colloidal suspensions also significantly affects the forms of structures they can exhibit. Low concentrations generally cause a dispersed phase, and in a contrast, with the balance of attractive and repulsive forces at sufficiently high concentrations, colloids systems can present ordered phases [89, 90]. Intermediate and high concentrations in the colloidal systems with large inter-particle interactions may result in aggregation or jammed structures (glass state) [91].

Various forces that occur in the colloidal systems include:

- gravitational forces;
- thermal (Brownian) forces;
- electric forces;
- surface tensions;
- viscous forces; etc.

Conventional forces as the gravitational body force still works on a colloidal particle, which is of the order $a^3 g\Delta\rho$ where g is the gravitational acceleration and $\Delta\rho$ is the density difference between the dispersed and the continuous phase. a represents the characteristic length (e.g. the diameter) of the colloidal particle, and is used throughout Section 1. Due to the movement of the bulk particles, an inertial force also comes into play which is of the order $\rho a^2 U^2$. Meanwhile, other microscopic forces show unique significance for the colloids, e.g. the Brownian force which demonstrates the thermal fluctuation of the particles which is of the order $k_B T / a$.

Regarding to the inter-particle forces, the first noticed is the London–van der Waals forces, which are of the order A/a. Here A is the Hamaker constant named after Hamaker [77], which is a function of the properties of both the dispersed and continuous phases,

$$A = \pi^2 C \rho_1^* \rho_2^* \tag{1.5}$$

where ρ_1^* and ρ_2^* are the number density of atoms in two interacting particles and C is the coefficient defined in the particle-particle pair interaction:

$$w(a) = -\frac{C}{a^6}. \tag{1.6}$$

The London–van der Waals forces are effective only up to several hundred angstroms. When the interactions are too far apart, the dispersion potential decays faster than $1/r^6$; where is called the retarded regime. Although their working distance is in the atomic scale, but a collective effects of such forces among the colloidal particles can lead to the force between macroscopic bodies known as the dispersion force.

Another important force is the electric force between two particles, which can be derived from Coulomb's law and is of the order $\varepsilon\psi_s^2$, where ε is the dielectric permittivity of the

continuous phase and ψ_s is the surface electric potential. For the colloidal particles, bubbles, or droplets immersed in fluids, the charges distribution on and among the particles is often described as an electrical double layer (EDL). EDL is a structure that refers to two parallel layers of charge surrounding the colloids (see **Figure 9**).

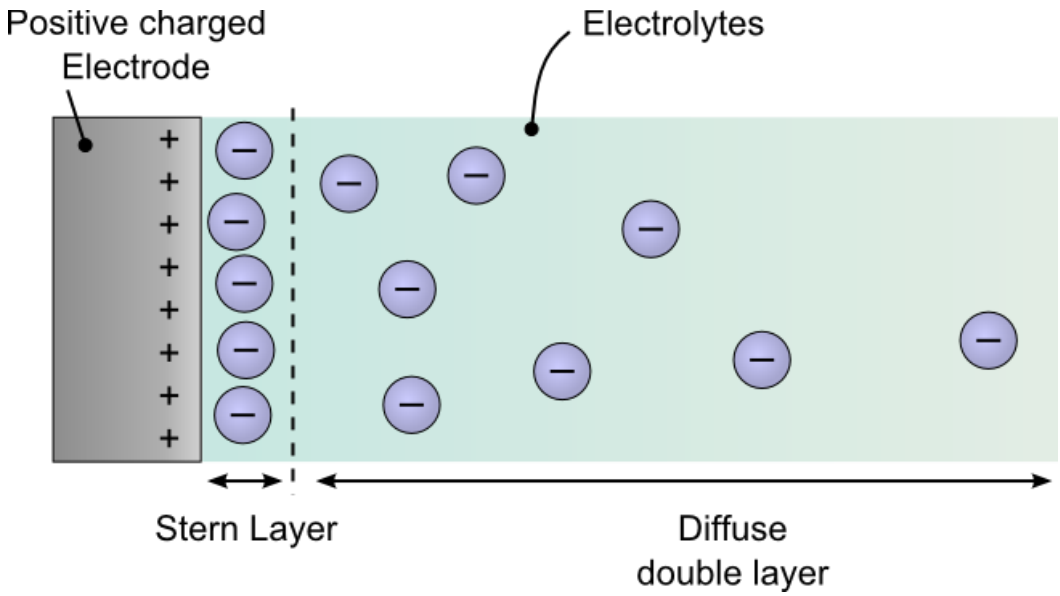

Figure 9 Electric double layer structure.

The first layer, which is close to the particle surface, comprises of ions adsorbed directly onto the colloids due to the inherent charge of the material. The second layer, which is further away, is composed of ions attracted towards the surface charge via the Coulomb force, and they are often electrically screening the first layer. The first layer is usually firmly packed near the colloids surface, and is often termed Stern layer after physicist Stern. The second layer is often loosely associated with the object, because the free ions can move in and out this layer due to the influence of electric attraction and thermal motion. Thus the second layer is also termed the diffuse layer, and the outer boundary of the diffuse layer is often termed slipping plane.

The EDL plays a fundamental role in many real-world systems. For instance, the stable milk dispersions can exist only because fat droplets are covered with an EDL that prevents their coagulation into butter. EDL also exists in practically all heterogeneous fluid-based systems, such as blood, paints, inks, ceramic slurries and cement slurries.

In terms of the surface charge properties of colloids, people often use zeta potential as the measurement scale. Zeta potential is defined as the electric potential in the interfacial double layer at the location of the slipping plane versus a point in the bulk fluid far away from the interface, i.e., zeta potential is the potential difference between the continuous fluid phase and a stationary layer of fluid attached to the dispersed particle. Empirically, a value of 25 mV (either positive or negative) can be taken as the scale that separates low-charged surfaces from highly-charged surfaces. The significance of zeta potential is that people can refer to its value as indicators of the stability of colloidal dispersions. The zeta potential indicates the degree of repulsion between adjacent, similarly charged particles in dispersion. For molecules and particles that are small enough, a high zeta potential will render stability, i.e. the solution or dispersion will resist aggregation. When the potential is low, the attractive forces exceed the repulsive forces and the whole dispersion tends to break and flocculate. Therefore, colloids with high zeta potential (negative or positive) are viewed as electrically stabilized while colloids with low zeta potentials tend to coagulate or flocculate.

The total effect of both attractive and repulsive interactions among colloidal systems is summarized in the DLVO theory [78, 79]. DLVO theory suggests that the stability of a particle in solution depends upon the total potential energy function. It is assumed that the total potential energy U_T is the balance of several competing contributions:

$$U_T = U_A + U_R + U_S \tag{1.7}$$

where U_A and U_R are the contribution of attractive and repulsive interactions, respectively, and U_S is the potential energy due to the dissolution, which is usually merely taking a very small portion to the total potential energy over the last few

nanometers of separation. The balance between U_A and U_R is much more important and it affects over a much larger distance.

$$U_A = -\frac{A}{12\pi d^2} \tag{1.8}$$

where A is the Hamaker constant as defined above and d is the displacement between two particles. The repulsive potential U_R usually requires a more complex function form:

$$U_R = 2\pi\varepsilon a\zeta^2 e^{-\kappa d} \tag{1.9}$$

where ε is the permeability of the solvent , κ is the inverse Debye length, a function of the ionic composition, and ζ is the zeta potential.

DLVO theory suggests that the stability of a colloidal system is determined by the sum of these van der Waals attractive (U_A) and electrical repulsive (U_R) forces that exist between particles as they approach each other due to the Brownian motion. This theory assumes that an energy barrier resulting from the repulsive force prevents two particles from touching to each another (see **Figure 10**). However, if the particles possess an energy level high enough, they could collide with sufficient energy to overcome that barrier, the attractive forces will pull them into contact and herein they stick strongly and irreversibly together. Therefore, if the particles have a sufficiently high repulsion, the dispersion will resist flocculation and the colloidal system will be stable. However if a repulsion mechanism does not exist, then flocculation or coagulation will eventually take place.

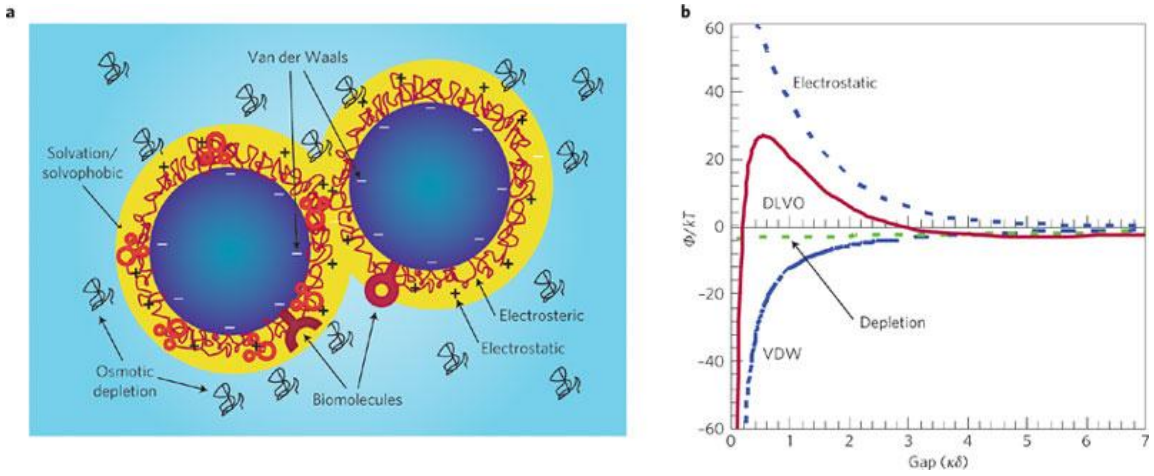

Figure 10 Illustrative description of DLVO theory. Van der Waals force and depletion force are attractive while the electrostatic forces are repulsive over a typical length scale. The DLVO theory in colloid science considers the sum of these forces: φ, interaction potential; k_B, Boltzmann constant; T, thermodynamic temperature; κ, inverse Debye length; δ, separation distance. Reprinted by permission from Macmillan Publishers Ltd: Nature Materials (reference [92]), copyright (2009).

In colloidal systems, especially the liquid-liquid systems such as emulsions, surface tension and viscosity play important roles in their interactions. Surface tension arises from the interaction between the two phases represented by the particle and the continuous medium. This force is of the order γa, where γ is the surface (interfacial) tension of the particle in the medium. The fluid (continuous phase) viscosity gives rise to a viscous force of the order μUa where μ is the viscosity of the continuous phase and U is the particle velocity through the continuous phase.

The impact of colloidal phenomenon is many-folds. Traditional industries, such as in the field of ink, paint and ceramics, highly depend on colloidal suspension in their production [93, 94]. Applications of colloidal systems are also valuable in the areas close to our daily life, like in personal care products, food and pharmaceuticals [68, 86, 88, 92, 95, 96]. The fascinating behavior of colloids has long been of interest to the scientific community. Colloidal particles attract scientific interests in several ways. The study on

colloids accompanied with many fundamental breakthroughs in the scientific history, like for the properties of light [97], and the understanding of Brownian motions and atomic structures [72]. Nowadays, colloidal science stems new branches in the interdisciplinary topics such as material science and biology. The knowledge of colloids can be used in producing advanced materials like photonic band-gap materials, microelectronics, chemical sensors and energy transfer materials [95, 96, 98]. The small size of the colloidal particles provides a significant surface area to volume ratio and therefore their behavior becomes crucial to understand many biological activities, since the cell often possesses the colloidal size.

1.2.3. Discotic Colloids

Discotic colloids are rarely visited in the anisotropic particle family. Following Onsager's seminar introduction of the phase transition of anisotropic particles to the scientific community [90], many research has been conducted on the rods and spheroids. Discotic colloids, however, still have not attracted enough attention. It is not difficult to find examples of disk-like particles in nature, such as red blood cells (RBC), clay particles, and asphaltenes. However, reports are scarce on the synthesis of uniform discotic colloids, which so far has been restricting the experimental investigation of disks (see **Figure 11**). Recently, there are various attempts in the synthesis and characterization of discotic colloids. Here, we summarize some significant works and discuss some future directions in this emerging frontier.

The synthesis of disk particles can be achieved by controlling key parameters (reactants, template, reaction conditions, etc.) to elect the disk morphology in contrast to naturally existing disks. The synthetic disks could have the advantages of known composition, uniform size and shape, prescribed aspect ratio, and tailored surface properties. They are of special interest in serving as model systems to study liquid crystal phase transitions. Several novel synthesis processes toward colloidal disks will be briefly discussed in Section 1 according to their principles of shape formation (see **Figure 11**). The discussion lays down a foundation for the understanding of disk self-assembly,

composite materials and rheology. A variety of chemical methods has been successfully applied for the syntheses of nanocrystals with controllable size distribution. The ability to tune the shape of the nanocrystals is of great interest to fundamental research and industrial applications. Alivisatos and co-workers [82] presented their method to synthesize hcp-Co nanodisks and comprehensively investigated the mechanism of nanocrystals shape control via selective adsorption of surfactants, in which an organic molecule is used to inhibit the crystal growth in a particular direction (**Figure 11**A).

Hence, disk formation results from the prohibition of growth along a unique axis, while rod formation will be preferred if the growth along a particular axis is stimulated. The parameters contributing to the high yield of disk nanocrystals (up to 85%) and a narrow size distribution include the chain length and the functional groups of surfactants, the choice of solvents, and the timing of reactant injection. The aspect ratio ρ (long dimension divided by short dimension) varied with particle sizes. It changed from $\rho \approx 2$ to $\rho \approx 9$ to $\rho \approx 22.5$ as the particle size increased. Korgel and co-workers [99] extended this selective adsorption concept and used solvent-less thermolysis of a copper alkylthiolate molecular precursor to fabricate the CuS nanodisks with aspect ratio around 2.7:1 and diameter-polydispersity of 15 % (**Figure 11**B).

Another chemical approach to obtain the nanoplatelets is controlled precipitation. Renowned research was conducted by Lekkerkerker and his co-workers [100-103]. They sought for a model system with short-range repulsion to exploit the liquid crystal phase transitions by increasing volume fraction. Gibbsite $Al(OH)_3$ nanocrystals were prepared by hydrothermal treatment of the acidic aluminum alkoxide solution and grafting a modified polyisobutene for steric stabilization (**Figure 11**D). In a good solvent, such as toluene, the nano-crystalline platelets suspensions exhibited long-term stability. The diameter- polydispersity of gibbsites was around 17% after fractionation and the aspect ratio was approximately 11. Similar method was used by Rennie and co-workers [104] on $Ni(OH)_2$ nanocrystals with polyacrylate as stabilizer, producing nanodisks with diameter-polydispersity 14% and aspect ratio 9.

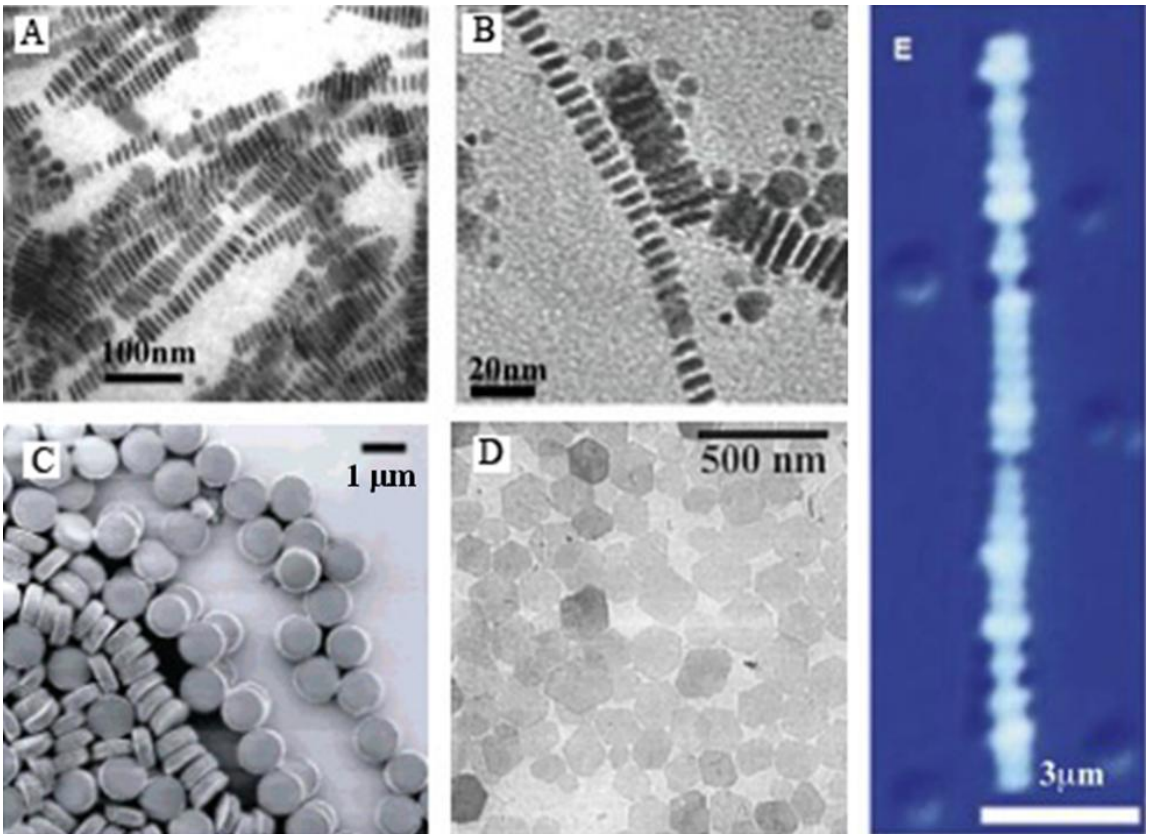

Figure 11 Various methods to synthesize discotic colloidal particles. (a) hcp [82]. Reprinted (adapted) with permission from V. F. Puntes, D. Zanchet, C. K. Erdonmez, and A. P. Alivisatos, J. Am. Chem. Soc. 124, 12874 (2002). Copyright (2002) American Chemical Society. (b) CuS [99]. Reprinted (adapted) with permission from M. B. Sigman Jr et al., J. Am. Chem. Soc. 125, 16050 (2003). Copyright (2003) American Chemical Society. (c) lithography [105]. Reprinted (adapted) with permission from S. Badaire, C. Cottin-Bizonne, W. Joseph, A. Yang, and A. D. Stroock, J. Am. Chem. Soc. 129, 40 (2007). Copyright (2007) American Chemical Society. (d) precipitated gibbsites. Reprinted by permission from Macmillan Publishers Ltd: Nature (reference [102]), copyright (2000). (e) wax [106, 107]. Reprinted with the permission of the American Physical Society, copyright (2002).

Different material and methods has been exploited to synthesize colloidal disk of microns in diameter. Mason and Cheng et al. [106-108] used a high temperature emulsification method to produce polydisperse wax droplets stabilized in water by SDS, which transformed into disks at low temperature (**Figure 11**E). The mechanism of this

shape transformation is believed to be related to the rotator phase and surface freezing of α-eicosene. These micron-sized colloidal disks have the advantage of low-cost, high production rate, easy preparation and convenient observation by optical microscopy. The monodispersity could be well controlled by the emulsification techniques, so it could serve as a model system to study the liquid crystal phase behavior.

Along with the emerging of micro-electro-mechanic-system (MEMS) technologies, the lithography process has been applied into the engineering of colloidal particles with anisotropic geometry. A generalization of this lithographic method will apply to materials that are not accessible through synthetic approaches. The molded shape by the mask offers a greater freedom in design and a greater accuracy in shape control. The aspect ratio can be tuned in the fabrication procedures by changing the thickness of the deposited layer. Recently, Stroock and co-workers [105] have used this method to produce uniformed colloidal disks (**Figure 11**C). Mason et al. [109, 110] developed the pillar-based and well-based deposit-particle-templating (De-PT) technique at low cost in instruments, and they can produce monodisperse disks and complex shapes such as the "colloidal alphabet soup". The use of lithography to define the particles in a versatile inorganic material opens the possibility of adding distinct physical attributes, such as magnetism, electrical conductivity, and fluorescence, to the individual colloids, but the disadvantage is the low yield at the state of the art.

Spherical colloids display a great variety of physical processes such as crystallization, melting and glass formation while anisotropic particles can have an even richer phase behavior. They can have more phase transitions than crystal-to-liquid and liquid-to-gas, and most interestingly, they can exhibits liquid crystal phases. Liquid crystals represent a special type of material which can exhibit the properties of both liquid and solid states with long-range crystalline order. The building blocks of these liquid crystals are often rods or plates, such that they have additional orientational degrees of freedom and can have alignment in the sense of a large scale, which accounts for the extra phase transitions.

Liquid crystals (LC) can be divided into thermotropic, lyotropic and metallotropic phases. Thermotropic and lyotropic LCs often consist of organic molecules. Thermotropic LCs exhibit a phase transition into the LC phase during the change of temperature. Lyotropic LCs exhibit phase transitions as a function of both temperature and concentration of the LC molecules in a solvent (typically water). Metallotropic LCs are composed of both organic and inorganic molecules; their LC transition depends not only on temperature and concentration, but also on the inorganic-organic composition ratio.

Liquid-crystal phases can be classified into many types, such as nematics, smectics, cholesterics, and discotics (see **Figure 12**) based on the different alignments. Typically, liquid crystal materials consist of rod-shaped units, which are called calamitic mesogens, as well as disk-shaped units, which are then called discotic mesogens. In most cases calamitic mesogens have the tendency to orient themselves along their longest axis. The first discotic liquid-crystal molecule was discovered with a benzene ring as the core surrounded by six alkyl chains in 1977 by S. Chandrasekhar [111]. Since then, a large number of discotic mesogens has been found. Disc-shaped molecules tend to orient along their short axis and often to lie on top of each other forming either discotic nematic phase, which represents only orientational ordering, or discotic columnar phase, which represents orientational and positional ordering.

In 1949, Lars Onsager [90] explained the reason behind the alignment of rod-like and disk-like colloids and proposed that minimization of Helmholtz free energy of the system was the leading factor to the phase separation at higher volume fractions. In particular, his insight shows that the entropy alone can favor (nematic) alignment of the colloids at relatively low concentrations in a system, while it is the increase of the total entropy because of the loss of orientational entropy in combination with the (larger) increase in excluded volume entropy in such systems that stabilize the nematic state.

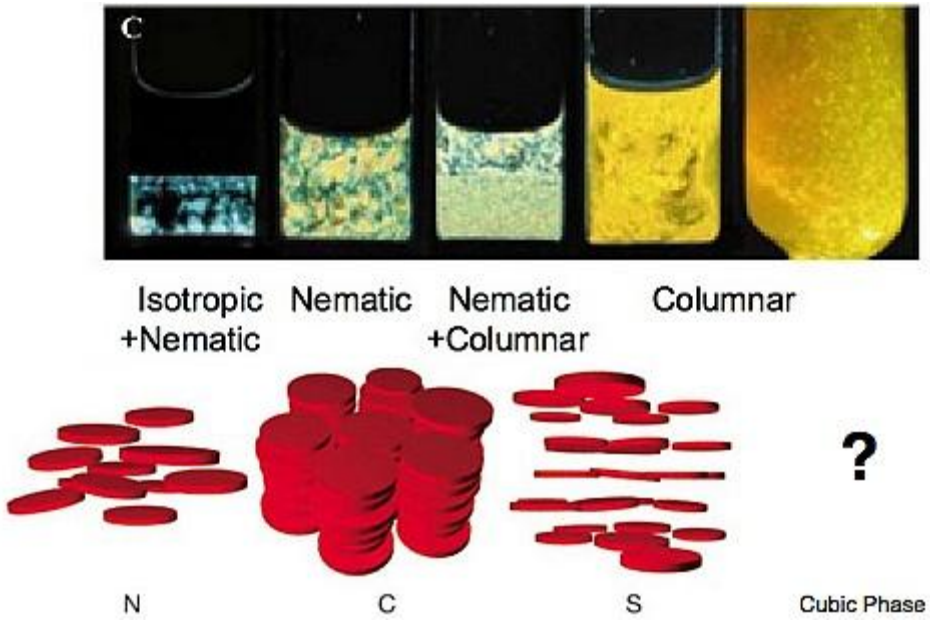

Figure 12 Liquid crystal phases formed by discotic colloids. Reprinted by permission from Macmillan Publishers Ltd: Nature (reference [102]), copyright (2000).

The applications of colloidal systems are often dependent on their behaviors when flowing in suspensions. For example, viscosity is a very important factor in the drilling fluid. Many industrial applications utilize a large amount of anisotropic particles, particularly clay particles. To study the rheological properties of colloidal suspensions, it is important to elucidate the hydrodynamic interactions of colloids. The theoretical work on the motion of disk particles in low Reynolds number flow dated back to 1960s [112-114]. In a series of work by Brenner and Cox, the Stokes resistance of the disk-like particles was calculated and the coupling of translation and rotation was considered. The results were generalized for the calculation of force and diffusivity of disk particles, which facilitated the study of rheology [21]. Recently, Brady et al. [115] pointed out that the aspect ratio of probe disks significantly affect the particle-tracking microrheology experiments in colloidal dispersions. The knowledge of the concentration dependence of viscosity in platelet suspensions is less exploited than spheres because of the limitation from polydispersity. Philipse et al. [101] investigated the intrinsic viscosity

in a nearly-hard plate dilute suspensions by rheometer measurement and dissipative particle dynamics (DPD) simulation. Their measurement yielded the intrinsic viscosity which provides an alternative way to characterize the number-averaged aspect ratio in the platelets suspensions and is simpler than the TEM/XRD method. The high-order coefficients in volume fraction virial expansion combined with the DPD simulation results supported the approximate hard-plate properties of gibbsite platelets.

Sedimentation is another vital method to characterize rheological properties in material research and processing. The sedimentation coefficient measured by van der Kooij and co-workers [100, 101] were used to calculate the second viral coefficient of the platelets which characterizes the inter-particle interaction potential. Theoretical and experimental efforts are still needed for the sedimentation measurement of disk particles, particularly with uniform particles. The hindrance functions (reduction of sedimentation velocity as a function of concentration) need to be characterized for monodisperse and polydisperse disk. Sedimentation can also be utilized to identity phase transitions and the equation of state [85].

A stimulating motivation to study disk-like particle rheology comes from the interest in human red blood cells (RBC) (e.g. see **Figure 13**). RBCs are soft deformable disk-like cells. Because the blood vessel system is not as regular as the pipeline system, but rather has complex fractal structure, the deformation and flowing properties of red blood cells are crucial for them to pass the narrower segment of the vessel and get to their destination. The whole blood rheology has been investigated by physiologists in the early stage [116], while the relevance of RBC deformability to the blood flow was later emphasized [117]. Recently, with the developing of micro-scale analytical techniques, the experimental study on RBC becomes much more convenient and quantitative. A series of optical manipulations have been performed on the human red blood cells by laser tweezers [118-122]. The flow and deformation of red blood cells has been observed in microfluidic channels resembling the vascular system [84, 123]. A few simulations are also conducted on RBC flow and deformation in spite of the difficulty deriving from

the non-Newtonian properties of blood [124, 125]. These works demonstrate vast kinds of RBC properties including viscoelasticity, adhesion, deformation of membrane etc. and the meanings of these properties to biological investigations and medical treatments.

Colloidal disks can come from different materials, inorganic and organic, are used to provide a variety of properties. These methods offer model systems for investigation of liquid crystal phase transitions. A few experimental observations of the isotropic-nematic and nematic-columnar transition verified the predictions of the theories and simulations. However, diameter and thickness polydispersity in current systems still raise many questions to theories, and better model systems are demanded with further efforts in experiments. The study of columnar stacking of nanoplatelets could have potential value in the research of solar cells [83]. As abundant examples in the nature, the clay-polymer composites exhibit a great potential of novel materials of better performance at low cost. Meanwhile, the study of red blood cell and similar particles with the help of micro-fabrication extends the research of colloidal disks to new interdisciplinary fields.

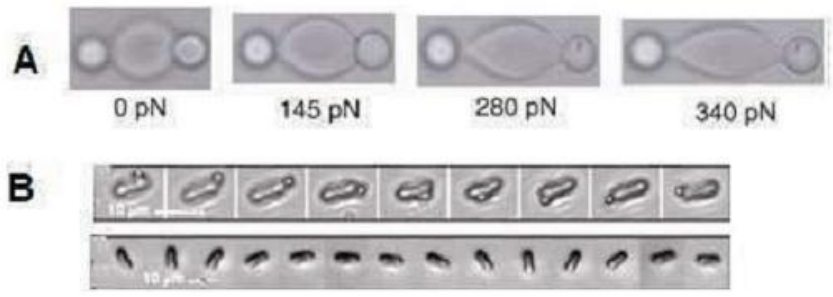

Figure 13 Rheological experiments on human red blood cells. A) Deformation of the stretched red blood cells at different loadings [118]. Reprinted from "Mechanics of the human red blood cell deformed by optical tweezers" M. Dao, C. Lim, and S. Suresh, J. Mech. Phys. Solids 51, 2259 (2003), with permission from Elsevier. B) Red blood cells in shear flow. (Top) Rotation of a bead stuck on the membrane of a tank-treading RBC. (Bottom) Tumbling RBC [123]. Reproduced by permission of The Royal Society of Chemistry.

1.3. Dissertation Overview

The primary object of this dissertation is to investigate the emulsification phenomena in microfluidic channels, in particular the flow-focusing design. Using experimental techniques, together with numerical simulation and modeling, the combining of AC electric field with microfluidic flow-focusing, as well as the dynamics of droplet formation in flow-focusing are discussed. The experiments of making disk-like colloidal particles using similar emulsification technique, and the characterization of its settling behavior, are also discussed as an example of applications.

In Section 2, in an attempt to understand the dynamics of drop formation in flow-focusing microfluidic channels, especially for the transition from periodic dripping to chaotic dripping observed in the experiments, numerical simulation is developed to use the VOF (volume of fluid) method to model the drop formation process, including a User-defined function accounting for electric repulsion to avoid coalescence in the simulation. Using this simulation technique, the experimental data are first confirmed with numerical results, then the principle behind the mode transition is discussed with regard to the critical length in saddle-node bifurcation of drop formation, and in the end the effect of varying orifice design is tested numerically and suggestions of design are given.

In the Section 3, we first explored the low-frequency AC Electro-Flow-Focusing (EFF) technique for controlling of droplet formation. This is the extension of previous work on DC Electro-Flow-Focusing [7], and the following topics are measured experimentally: (1) the relationship between the droplet size distribution and the electric field (voltage) variation; (2) the different variations of droplet size in different waveforms. The different behavior with regard to DC Electro-Flow-Focusing is compared, and this emulsification process was modeled in analog to the charge accumulation and release in an RC electric circuit with an adjustable resistor, and the simulated data are compared with the experiments.

The phenomena related to the behavior of discotic colloidal suspensions are addressed in Section 4. Various methods for the fabrication of disk-like colloidal particle are described in the first place. After that, the characterization methods are briefly introduced, including dynamic light scattering and analytical centrifugation. Following that, the sedimentation measurement of discotic colloidal suspensions are preformed at a wide range of concentrations. The highlight is a hindrance function for a wide range of volume fractions during the sedimentation of disk-like colloidal suspensions.

Finally, the concluding remarks are given.

2. DYNAMIC MODES OF DROP FORMATION IN MICROFLUIDICS

2.1. Summary

Microfluidics received a high popularity in the recent decade as its application in particle synthesis, micro-reactors and chemical analysis. Currently, the principle of design and monitor microfluidic devices stays at the empirical level, commonly only rules of thumbs are available for guidance. In a flow focusing microfluidic device, a water stream is stretched by a viscous force to a sharp tip and breaks into drops of uniform size at regular time intervals. At a critical capillary number, it is observed that a frequency doubling to bimodal drop production occurs. A rich dynamic bifurcation, including chaos, was observed with decreasing capillary number or varying water flow rate. The saddle-node bifurcation of the stretch of the water tip accounts for these nonlinear dynamics. In this computer simulation, it is aimed to investigate into more insight in the droplet formation inside microchannels, and the original motivation of this comes from experimental observation of droplet size oscillation in microfluidic channels. The results may help better understand and design flow-focusing microfluidics for applications such as cell encapsulation and particle synthesis.

2.2. Introduction

Drop formation is a phenomenon that can be found everyday from the dripping faucet in kitchen or bathroom. The scientific investigation of drop formation can be traced back to a few centuries ago when French scientist noticed the water stream flowing out of a faucet breaks into drops, and explained the mechanisms behind it as gravity and external forces [16]. It is realized later by Young and Laplace that the surface tension also serves an important role as the destabilizing agent [21]. Ever since then, the study of drop formation is active in many subjects of dynamics and physics. The dripping faucet has served as a paradigm of chaotic dynamics from the beginning of modern chaos theory [18], and recent studies have focused on the singularity formation in free-surface flows

[126, 127]. The study of dripping faucet provides analogical models for similar phenomenon of drop formation processes like that of raindrops. Due to the similar dimensional scale and low flow rate, it is also a very helpful model for understanding the droplet formation in microfluidics, which is the motivation in this thesis. Starting from the basic concept of bifurcation theory, the equilibrium and saddle-node transition in drop formation will be introduced in the following sections.

2.2.1. Bifurcation Theory

Bifurcation theory is the mathematical study of changes in the qualitative or topological structure of a given dynamical systems. A bifurcation occurs when a small smooth change made to the parameter values (the bifurcation parameters) of a system causes a sudden "qualitative" or topological change in its behavior [128].

With respect to the dynamic system in the form of differential equations, which is often formulated from the equations of motions in a physical system, the setting for these physical models is called the phase space, i.e., a point in the phase space corresponds to a state of the system. For a differential equation with initial condition at point $\boldsymbol{x}$ in phase space, the solution defines a curve passing through $\boldsymbol{x}$, and for all points in phase space, the collective of all these curves forms the phase portrait.

Phase portrait is a global (overview) picture of the qualitative character of the dynamic of the differential equation; hence it will depend on any parameter(s) in the equation or boundary condition. By varying these parameters, the phase portrait may deform slightly and reserve its qualitative feature, or it may suddenly change dramatically. Bifurcation theory studies these qualitative changes in phase portrait, like the appearance or disappearance of equilibrium, periodic orbits, etc.

It is useful to divide bifurcations into two principal classes: local bifurcations, which the drop formation is often attributed to, and global bifurcations, which will not be discussed in details here. The local bifurcation can be analyzed entirely through changes in the

local stability properties of equilibrium, periodic orbits, or other invariant sets as parameters cross through critical thresholds.

A local bifurcation occurs when a parameter change causes the stability of an equilibrium (or fixed point) to change. In continuous systems, this corresponds to the real part of an eigenvalue of an equilibrium passing through zero. The equilibrium is non-hyperbolic at the bifurcation point. The topological changes in the phase portrait of the system can be confined to arbitrarily small neighborhoods of the bifurcating fixed points by moving the bifurcation parameter close to the bifurcation point (hence 'local').

2.2.2. Saddle-Node Bifurcation

In the mathematical area of bifurcation theory a saddle-node bifurcation, is a local bifurcation in which two fixed points (or equilibrium) of a dynamical system collide and annihilate each other. The term “saddle-node bifurcation” is most often used in reference to continuous dynamical systems. In discrete dynamical systems, the same bifurcation is often instead called a fold bifurcation [128].

In mathematics, a saddle point is a point in the domain of a function which is a stationary point but not a local extremum. The name derives from the fact that in two dimensions the surface resembles a saddle that curves up in one direction, and curves down in a different direction (like a horse saddle or a mountain pass). In terms of contour lines, a saddle point can be recognized, in general, by a contour that appears to intersect itself. For example, two hills separated by a high pass will show up a saddle point, at the top of the pass, like a figure-eight contour line.

For a second-order linear autonomous systems, a critical point is a saddle point if the characteristic equation has one positive and one negative real eigenvalue. The normal form of a saddle-node bifurcation is:

$$\frac{dx}{dt} = r + x^2 \tag{2.1}$$

Here ***x*** is the state variable and *r* is the bifurcation parameter. If the phase space is one-dimensional, one of the equilibrium points is unstable (the saddle), while the other is stable (the node). If r < 0 there are two equilibrium points, a stable equilibrium point at $-\sqrt{-r}$ and an unstable one at $\sqrt{-r}$. At r = 0 (the bifurcation point) there is exactly one equilibrium point. At this point the fixed point is no longer hyperbolic. In this case the fixed point is called a saddle-node fixed point. If r > 0, there are no equilibrium points.

Before we move on the dynamic mode of droplet formation, let us first consider the equilibrium case of a pendant drop still attached to the faucet. When the flow rate is very small, the drop will not leave the faucet until its volume exceeds a threshold V_C. The pendant drop with a volume less than V_C is stable and axis-symmetric, and its shape is determined by minimizing the sum of its gravitational and surface energy subject to the constraint of constant volume, and leads to the well-known Laplace-Young equation. Quantitatively, the balance of constraint forces can be summarized into an equation in the vertical direction (**Figure 14**), along with kinematic equations for the shape of the interface, leading to the following system of dimensionless ODEs:

$$\frac{\mathrm{d}\theta}{\mathrm{ds}} = \frac{\cos\theta}{r} - z \tag{2.2}$$

$$\frac{\mathrm{dz}}{\mathrm{ds}} = -\cos\theta \tag{2.3}$$

$$\frac{\mathrm{dr}}{\mathrm{ds}} = \sin\theta \tag{2.4}$$

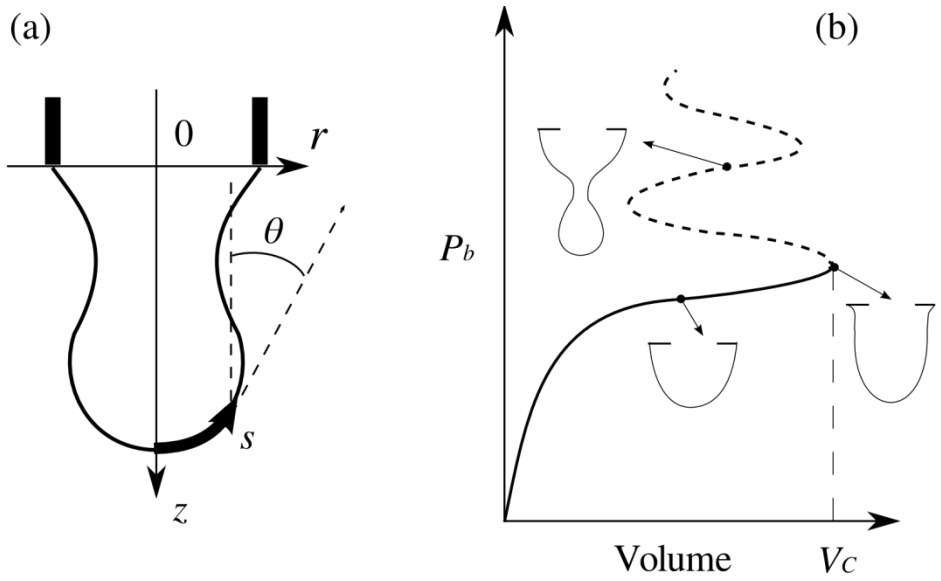

Figure 14 Scheme of the equilibrium of a pendant drop [149]. (a) geometric setup; (b) critical volume of the drop formation. Reprinted with permission from Z. Dogic, A. Philipse, S. Fraden, and J. Dhont, J. Chem. Phys. 113, 8368 (2000). Copyright (2000), American Institute of Physics.

Here the dimensional variables r, s, θ and z are depicted in (**Figure 14**). r and z are the horizontal and vertical coordinates, respectively. s is the coordinate along the interface curve, and θ is the angle between the tangential direction of the interface and the vertical direction. For the generality and simplicity of analysis, all the variables are made into dimensionless forms by the following scaling: all the dimensional variables are scaled by the capillary length $l_0 = \sqrt{\Gamma / g\rho}$, all the temporal variables are scaled by $t_0 = (\Gamma / \rho g^3)^{1/4}$, all masses scaled by $m_0 = \rho l_0^3$, and pressure scaled by $P_0 = \sqrt{\rho \Gamma g}$. Γ represents the surface tension of the fluid, and ρ is the density of the drop in a gravitational field g.

The boundary conditions at the bottom of the drop are $r(0) = 0$, $\theta(0) = \pi / 2$ and $z(0) = P_b$ where P_b is the unknown hydrostatic pressure at the bottom of the drop. For different values of P_b, equations (2.2)-(2.4) can be integrated as an initial value problem

till the boundary condition $r = R$ (we choose R=1 ; in dimensional terms $R = l_0$) is satisfied, and use a shooting method to determine P for a given drop volume. For later use, we scale $V = \pi r^2 \mathrm{dz}$. Of the various shapes of static pendant drops that exist for a given volume, shown in **Figure 14b**, only the branch starting at the origin with a positive slope is stable, so that there is a critical drop volume V_c at which the weight of the drop just balances the force due to surface tension. The instability when $V > V_c$ results from the "collision" of two stationary solutions, a stable one and an unstable one, and corresponds to a saddle-node bifurcation.

2.3. Experimental Observation

The device, sketched in **Figure 15** [17], was fabricated through soft lithography [42] using PDMS (poly-dimethylsiloxane) to replicate negative stamps made of SU8 photoresists, and sealed to a glass slide after plasma treatment. The depth of the channels is about 30 μm. The widths of the inlet and outlet channels are 100 μm. The orifice is 50x50 $\mu \mathrm{m}^2$ in the slide plane. The continuous phase is hexadecane with 1.5% Span80 as surfactants. It flows through two side channels. The water flows through the central inlet channel. Oil exerts shear forces to the water stream's end and stretches it to a sharp tip. The tip breaks into small drops resulting from the flow perturbation at the common exit orifice of the water and oil streams.

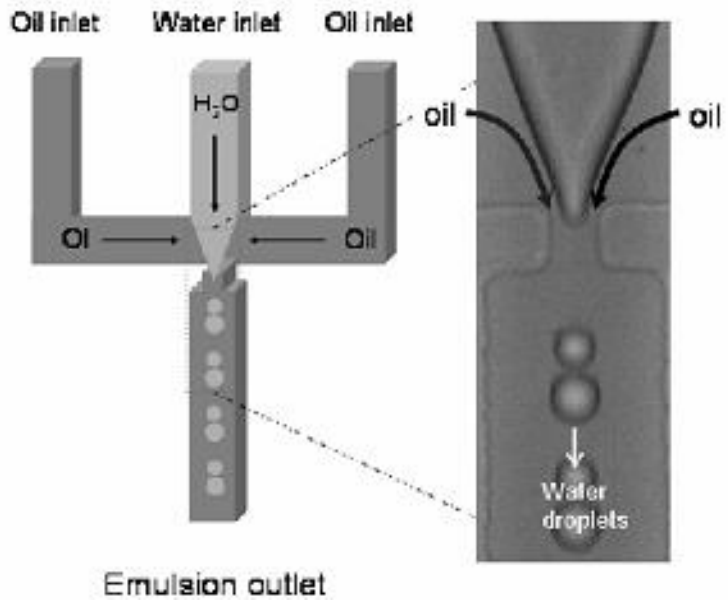

Figure 15 Schematic of the flow-focusing device. The widths for the water and oil inlet channels are 100 μm, and the heights are 30 μm. Zoom into the flow-focusing region of the device, the dimensions for the exit orifice are 50x50x30 μm^3. Adapted from [17] with permissions of the International Institute of Informatics and Cybernetics.

For a wide range of flow rates, the device produces emulsions at fixed oil flow rate of 1000 μl /hr. Drops of uniform size are obtained between water flow rate 265 μl /hr and 1000 μl /hr, as shown in **Figure 16**, and the size decreasing as water flow rate decreases. When the water flow rate is larger than 1000 μl /hr, the water tip stretches passing the orifice, and drops are produced further down through the propagation of Rayleigh instabilities, which is in the jet regime of the device and beyond the scope of this discussion here.

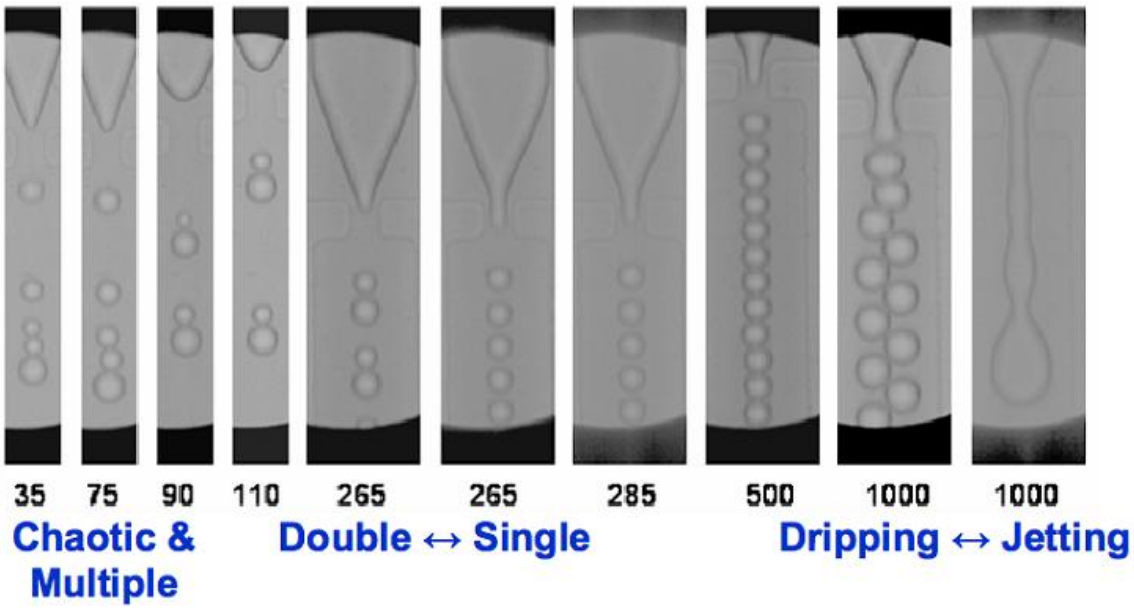

Figure 16 Micrographs of water drops at different water flow rates. Adapted from [17] with permissions of the International Institute of Informatics and Cybernetics.

At water flow rate 265 μl /hr, an interesting phenomenon takes place. Sometimes, the device makes sequentially a bigger drop and a smaller one, as shown in **Figure 16**. The device enters the bimodal regime. With further decrease of water flow rate, the size contrast increases. At 90 μl /hr, the size of the smaller drop differentiates again. The device bifurcates into the multi-period regime with decreasing water flow rate. Around 50 μl /hr the device enters the chaotic regime indicated by the broad drop size and separation variations. To quantify observations, a series of movies at different flow rates is taken for sufficient long time at high speed using a Phantom V5.0 CCD camera. Each frame of the movies is digitized using IDL (Research System, Inc.), and time separations between drops are measured with resolution up to 10 μs .

Figure 17 shows the complete topological structure of the dynamic states in the water verses oil flow rate plane. The transitions take place at relatively low oil and water flow rates. The overlapping of the period-1 and period-2 drop productions as indicated by the

small solid dots and stars in **Figure 17** shows the boundary of transition between them. At the lowest oil flow rate, the device goes back to period-1 regime.

2.4. CFD Simulation

In order to investigate the dynamics of transition in drop formation, multiphase flow CFD simulation is often employed to repeat the experimental results and explore the variables which are either missing or hard to probe during experiments. VOF model is one of the most powerful methods for such multiphase CFD simulation. The computational fluid dynamics (CFD) code ANSYS FLUENT (ANSYS Inc., 2009) was used in this simulation. The Volume of Fluid model (VOF) in FLUENT was applied to account for the two phases flow.

The VOF model can model two or more immiscible fluids by solving a single set of momentum equations and tracking the volume fraction of each of the fluids throughout the domain. Typical applications include the prediction of jet breakup, the motion of large bubbles in a liquid, and the motion of liquid after a dam break, and the steady or transient tracking of any liquid-gas interface.

The VOF formulation relies on the fact that two or more fluids (or phases) are immiscible. For each additional phase that you add to your model, a variable f, the volume fraction of the phase, is introduced in the computational cell. In each control volume, the volume fractions of all phases sum to unity. The fields for all variables and properties are shared by the phases and represent volume-averaged values, as long as the volume fraction of each of the phases is known at each location. Thus the variables and properties in any given cell are either purely representative of one of the phases, or representative of a mixture of the phases, depending upon the volume fraction values. In other words, if the volume fraction of one of the fluids in the cell is denoted as f_q, then the following three conditions are possible:

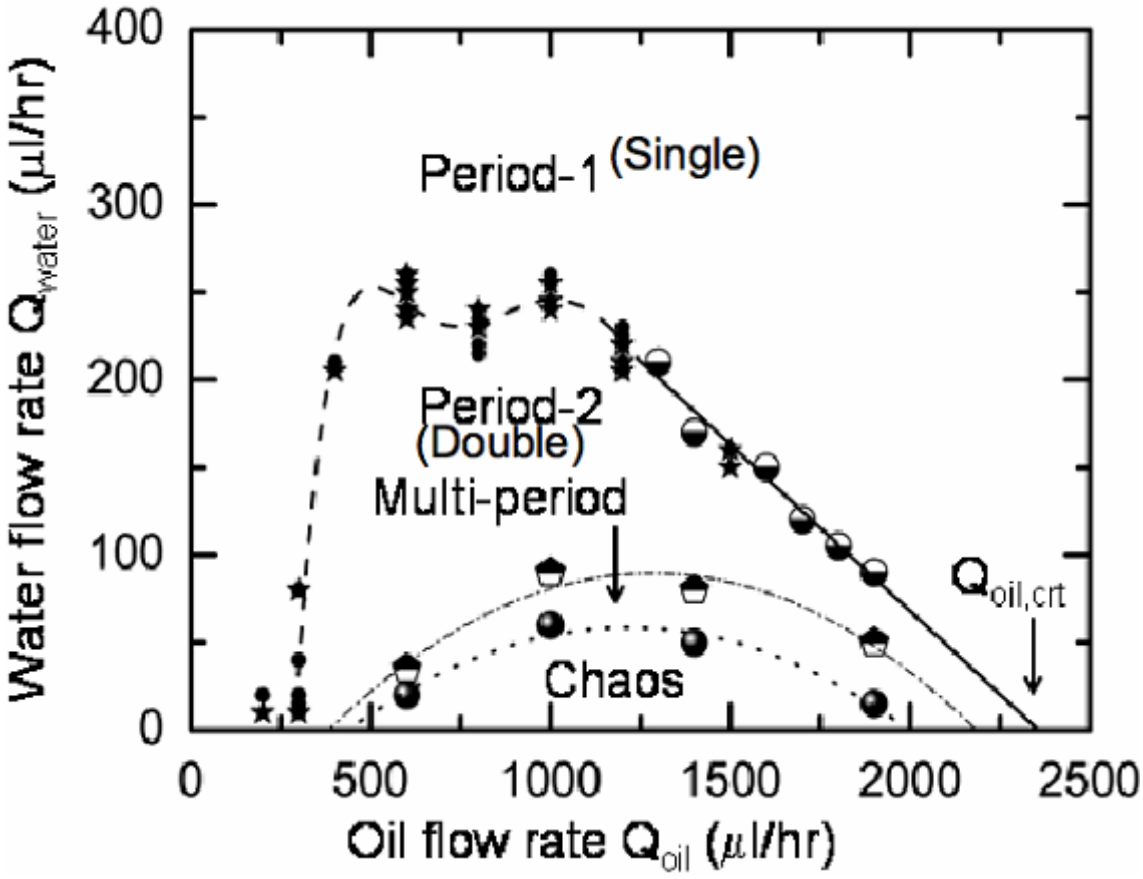

Figure 17 The transition diagram of droplet formation dynamics in the water vs oil flow rate plane. Lines are the guide for eyes for the boundaries between dynamic modes. Symbols are experimental data. Solid dots represent period-1 drop production. Stars represent period-2 drop production. Adapted from [17] with permissions of the International Institute of Informatics and Cybernetics.

$$\begin{cases} f = 0, \text{ The cell is empty of this fluid.} \\ f = 1, \text{ The cell is full of this fluid.} \\ 0 < f < 1, \text{ The cell contains the interface between two or more fluids.} \end{cases} \tag{2.5}$$

Based on the local value of f_q, the appropriate properties and variables will be assigned to each control volume within the domain. The discretization scheme treat these cells with the same interpolation as the cells that are completely filled with one phase or the other, rather than applying a special treatment.

The tracking of the interface(s) between the phases is accomplished by the solution of a continuity equation for the volume fraction of one (or more) of the phases. The control-volume formulation used in this simulation requires that convection and diffusion fluxes through the control volume faces be computed and balanced with source terms within the control volume itself.

In the approach of tracking interfaces between two immiscible fluids, the standard interpolation schemes are used to obtain the face fluxes whenever a cell is completely filled with one phase or another. Only when the cell is near the interface between two phases, the geometric reconstruction scheme is used. The geometric reconstruction scheme represents the interface between fluids using a piecewise-linear approach(**Figure 18**). In ANSYS FLUENT this default scheme is the most accurate and is applicable for general unstructured meshes. It assumes that the interface between two fluids has a linear slope within each cell, and uses this linear shape for calculation of the advection of fluid through the cell faces. The first step in this reconstruction scheme is calculating the position of the linear interface relative to the center of each partially-filled cell, based on information about the volume fraction and its derivatives in the cell. The second step is calculating the advecting amount of fluid through each face using the computed linear interface representation and information about the normal and tangential velocity distribution on the face. The third step is calculating the volume fraction in each cell using the balance of fluxes calculated during the previous step.

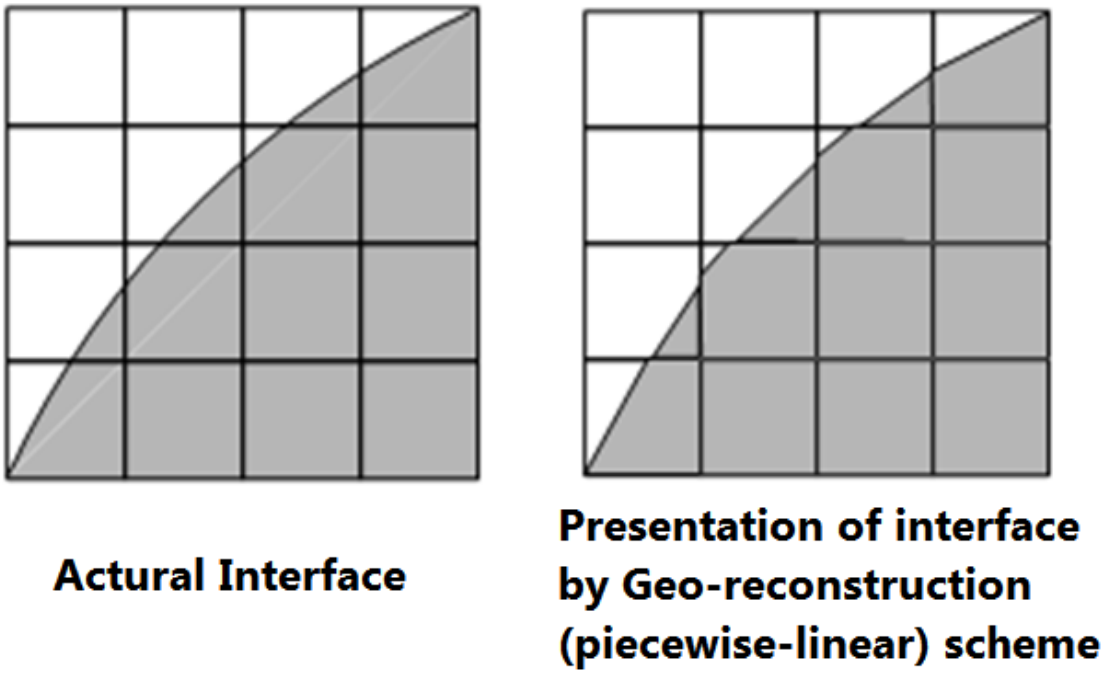

Figure 18 Scheme of interface tracking (geo-reconstruct) in the VOF simulation.

The properties appearing in the transport equations are determined by the presence of the component phases in each control volume. In a two-phase system, for example, if the phases are represented by the subscripts 1 and 2, and if the volume fraction of the second of these is being tracked, the density in each cell is given by

$$\rho = f_2\rho_2 + (1 - f_2)\rho_1 \ . \tag{2.6}$$

In general, for an n-phase system, the volume-fraction-averaged density takes on the following form:

$$\rho = \Sigma f_q \rho_q \tag{2.7}$$

All other properties (e.g., viscosity) are computed in this manner.

A single momentum equation is solved throughout the domain, and the resulting velocity field is shared among the phases. The momentum equation, shown below, is dependent on the volume fractions of all phases through the properties ρ and μ

$$\begin{cases} \nabla \cdot \mathbf{V} = 0 \\ \dfrac{\partial \rho \mathbf{V}}{\partial t} + \nabla \cdot \left(\rho \mathbf{V} \mathbf{V} \right) = -\nabla P + \rho g + \nabla \cdot \left(\mu \left(\nabla \mathbf{V} + \nabla^T \mathbf{V} \right) \right) + \mathbf{F}_s \end{cases} \tag{2.8}$$

The VOF model also includes the effects of surface tension along the interface between each pair of phases. The model can be augmented by the additional specification of the contact angles between the phases and the walls. Surface tension arises because of attractive forces between molecules in a fluid. Consider an air bubble in water, for example. Within the bubble, the net force on a molecule due to its neighbors is zero. At the surface, however, the net force is radially inward, and the combined effect of the radial components of force across the entire spherical surface is to make the surface contract, thereby increasing the pressure on the concave side of the surface. The surface tension model in ANSYS FLUENT is the continuum surface force (CSF) model. With this model, the addition of surface tension to the VOF calculation results in a source term in the momentum equation. To understand the origin of the source term, consider the special case where the surface tension is constant along the surface, and where only the forces normal to the interface are considered. It can be shown that the pressure drop across the surface depends upon the surface tension coefficient, σ, and the surface curvature as measured by two radii in orthogonal directions, R_1 and R_2:

$$p_2 - p_1 = \sigma \left(\frac{1}{R_1} + \frac{1}{R_2} \right) \tag{2.9}$$

where p_1 and p_2 are the pressures in the two fluids on either side of the interface. In ANSYS FLUENT, a formulation of the CSF model is used, where the surface curvature is computed from local gradients in the surface normal at the interface. The calculation of surface tension effects on triangular and tetrahedral meshes is not as accurate as on quadrilateral and hexahedral meshes. The region where surface tension effects are most important should therefore be meshed with quadrilaterals or hexahedra, and the latter is used in this simulation. The importance of surface tension effects is determined based on the value of two dimensionless quantities: the Reynolds number, **Re**, and the capillary

number, **Ca**; or the Reynolds number, **Re**, and the Weber number, **We**. For **Re** << 1, the quantity of interest is the capillary number:

$$Ca = \frac{\mu U}{\sigma} \tag{2.10}$$

and for **Re** >> 1, the quantity of interest is the Weber number:

$$We = \frac{\rho a U^2}{\sigma} \tag{2.11}$$

where U is the free-stream velocity. Surface tension effects can be neglected if **Ca** >>1 or **We** >>1.

2D and 3D geometry mesh are built according to the experimental setup shown in **Figure 15**. The tracking of the interface(s) between the phases is accomplished by the solution of a continuity equation for the volume fraction of one (or more) of the phases. The governing equations are discretized to algebraic equations by using a control-volume-based technique. The details of material properties, boundary conditions and solver settings are summarized in **Table 2** and **Table 3**, respectively. The calculation is done on the hydra supercomputer in TAMU, in parallel computation mode which is built in FLUENT, using 4-16 nodes according to the scale of different simulation cases.

Initial results of 2D and 3D simulations are shown in **Figure 19** and **Figure 20**. The 2D simulation cases generally catch the feature of the droplet formation mode transition, in which single mode, bimodal mode, and multiple mode are all shown. The problem with 2D simulation cases is that the tip shape is over-deformed which deviates greatly from the experimental results, and therefore the droplet size and water tip position are not accurate comparing with experimental results. The possible reasons of this deviation

Table 2. The settings of material properties and boundary conditions in the FLUENT simulation cases.

Name	Dispersed Phase (water)	Continuous Phase (oil)
Density	998.2 kg/m^3	773 kg/m^3
Viscosity	0.001 kg/(m*s)	0.003 kg/(m*s)
Surface tension	0.015 N/m	
Inlet velocity	0.017 m/s	0.075 m/s
Outlet	Zero gradient	
Wall contact angle	90 degree (water-wetting)	175 degree (oil-wetting)
Source term	A user-defined source term of force density is added to momentum variables (explained later), which value is zero on all boundaries, except for zero gradient boundary condition at outlet.	

Table 3. The settings of solver in the FLUENT simulation cases.

Name	Solver settings
Version	ANSYS FLUENT, 13.0.0, laminar, pressure-based solver,
Transient scheme	1st-order implicit
Gradient scheme	Green-Gauss cell based
Pressure-Velocity Coupling	Pressure-Implicit with Splitting of Operators (PISO)
Pressure	PREssure STaggering Option (PRESTO)
Momentum scheme	2nd-Order upwind
Source term scheme	2nd-order upwind
VOF scheme	Euler explicit, Courant number =0.25, Geo-Reconstruct scheme

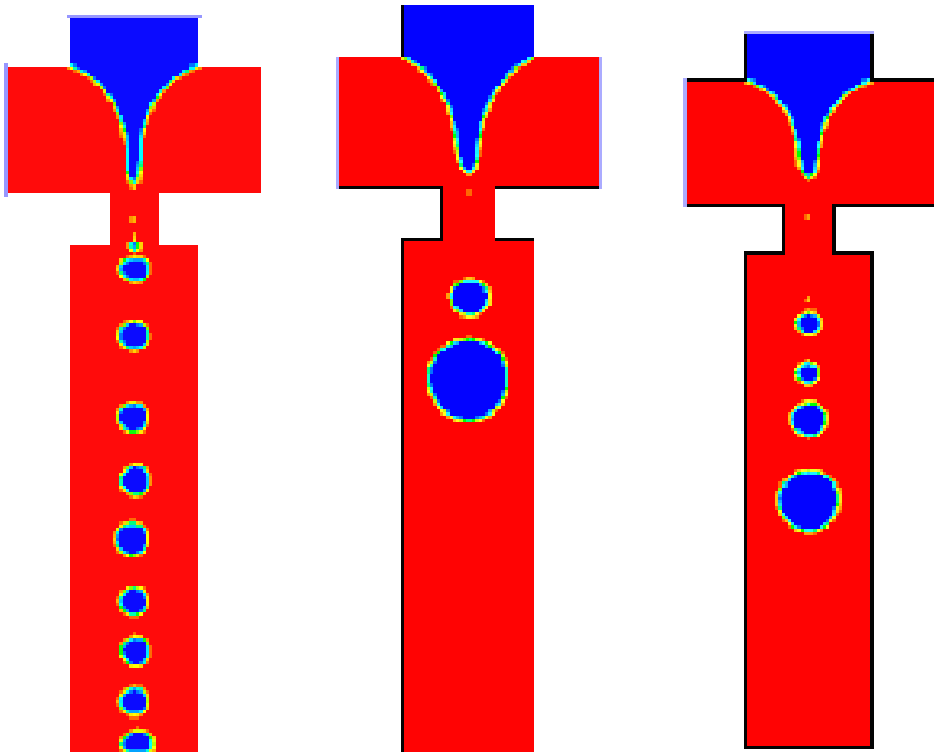

Figure 19 2D simulation results using ANSYS FLUENT. (left) uniform droplets; (middle) bimodal mode in which a pair of big and small droplet is generated periodically; (right) multiple mode in which a group of a leading big drop with several smaller drops are generated.

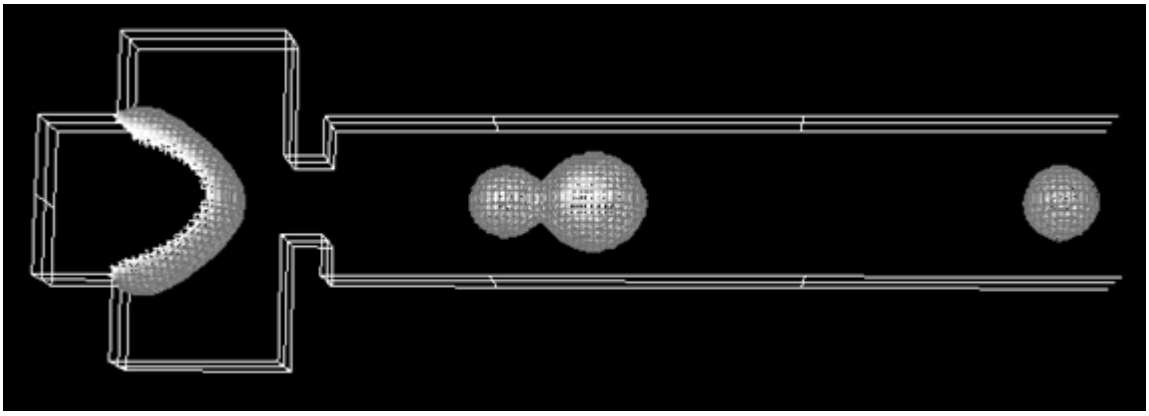

Figure 20 3D simulation results of bimodal droplet formation. Here, no repulsive force is added and therefore the big and the small drop coalesce.

in 2D simulation includes: 1) the ratio of channel height over channel width is close to 1, therefore the boundary effects of the vertical walls of the channel might not be negligible; and 2) the top surface (PDMS) and the bottom surface (glass) of the microfluidic channel has different wetting properties, and this information is missing in the 2D simulation cases; and 3) in addition, coalescence also occurs in the bimodal and multiple modes simulation cases, which does not happen in the experiments. To solve these problems, 3D simulation cases with correct surface wetting properties are built for the bimodal mode, which solve the first two problems, but still show unphysical coalescence. In the experiments, the coalescence of droplets are excluded because of the electrostatic repulsions between droplet surfaces, which is rendered by the surfactants (Span 80 in this study) added to the fluids. However, such electrostatic repulsive force are not built in the default ANSYS FLUENT algorithm, and adding such repulsive forces would be the key to solve the coalescence problem.

The classic theory of electrostatic screening (repulsion) is:

$$-\nabla^2 \Delta\phi(r) = \frac{1}{\varepsilon_0} Q\delta(r) - e\Delta\rho(r) \tag{2.12}$$

in which r is the distance from origin, ϕ is the electric potential, ρ is the number density of electrons at position r, Q represents a fixed point charge introduced at the origin which causes the screening (repulsion), $\delta(r)$ represents Dirac function, ε_0 is permittivity constant, and e is elementary charge constant, respectively. To simplify the above equation into a feasible form to use in FLUENT, Debye-Huckel approximation is adopted. Assuming the system is in thermodynamic equilibrium at room temperature, where the fluid particles all obey Maxwell-Boltzmann statistics, it will obtain:

$$e\Delta\rho \simeq \varepsilon_0 k_0^2 \Delta\phi, \tag{2.13}$$

and k_0 is defined as:

$$k_0 = \sqrt{\frac{\rho e^2}{\varepsilon_0 k_B T}} \tag{2.14}$$

and a parameter $\lambda_D \equiv 1/k_0$ is usually called Debye length, which characterizes the screening length resulted by the electrostatic environments. Plug (2.13) and (2.14) into (2.12), this approximation results in a Poisson equation of electrostatic repulsion:

$$\left[\nabla^2 - k_0^2\right]\phi(r) = -\frac{Q}{\varepsilon_0}\delta(r) \tag{2.15}$$

on which the following user-defined scalar (UDS) field ϕ is introduced to provide a extra source term in FLUENT algorithm to simulate the electrostatic repulsion forces:

$$\nabla^2\phi = k_0^2\phi - \rho_{UDS}(f). \tag{2.16}$$

In (2.16), f represents the VOF volume fraction as defined in (2.5); ρ carries the meaning of charge distribution on the drop surface, when $f < 0.5$, $\rho = \rho_0$, and when $f \geq 0.5$, $\rho = 0$; ϕ carries the meaning of electrostatic potential, and is used here as a "distance sensor". According to the calculations in [129], when $\phi k_0^2 / \rho_0 > 0.0006$, two spherical surfaces are close enough that their distance is close to the scale of the Debye length, hence a constant repulsive force density F would be added when this requirement is met to provide the repulsion and avoid coalescence. Because the charge distribution and electrostatic potential are hard to measure in the experiments, the values $\rho_0 = 1.0\times10^{-3}, k_0^2 = 2.5\times10^8, F = 1.8\times10^7$ N/m are selected by trial and error to best simulate the experiment results (see **Figure 21**). The following discussions are all based on this basic simulations setting with repulsion force by UDS. The simulation results are also validated by refining mesh size.

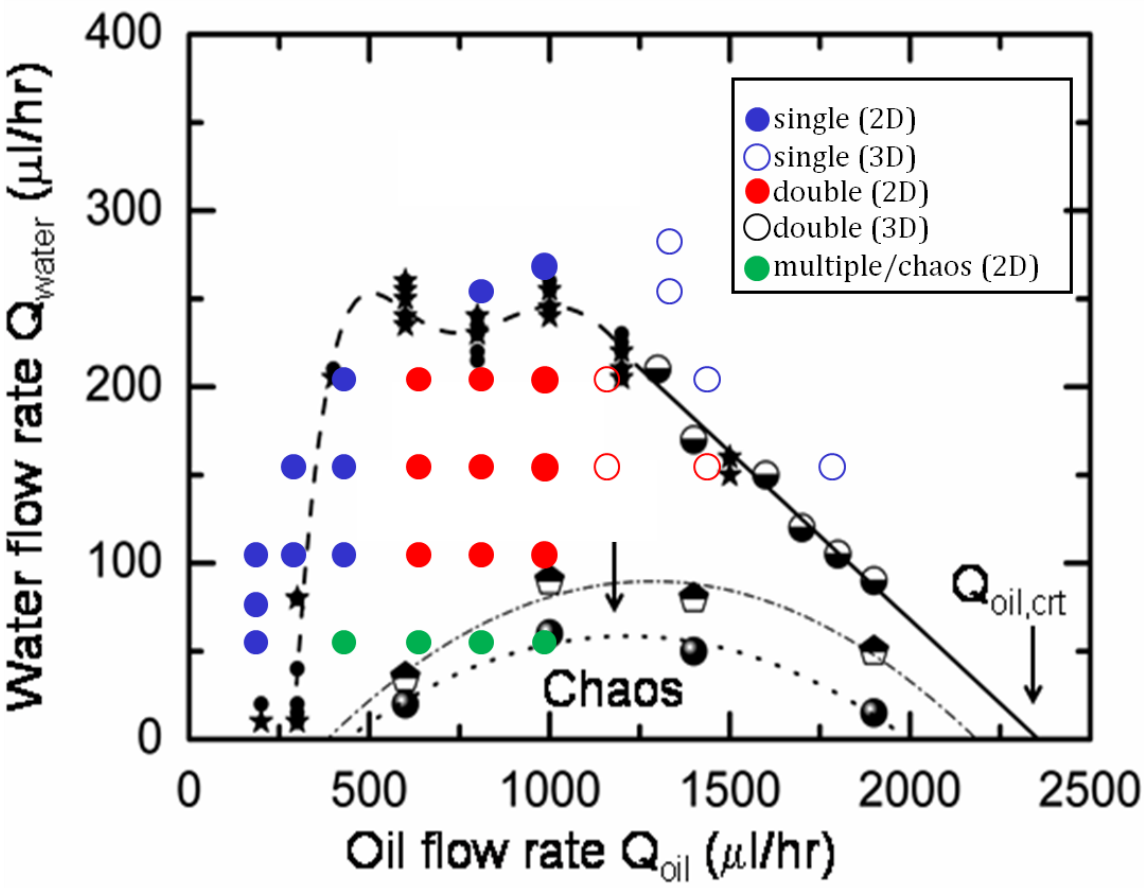

Figure 21 Plot of simulation data superposed on the transition diagram of droplet formation dynamics. Solid symbols correspond to 2D simulation results, and the empty symbols correspond to 3D simulation results. Different colors represent different drop formation modes.

2.5. Results and Discussion

The process of single-size formation of droplets in the flow focusing microfluidic device is shown in the evolving contour plots in **Figure 22**. The experimental visualization of two immiscible fluids in flow-focusing system is illustrated in **Figure 23** (top), and compared with the simulation results under the same geometry and conditions (bottom). As seen in the figure, the plot of the simulated results for droplet formation matches with the flow visualization of the experimental results. The simulation cases at low-Q_{oil} region ($Q_{oil} \leq 400\ \mu$L/hr) produce single droplet size at various water flow rates. The

simulation cases at medium-Q_{oil} region ($400 \leq Q_{oil} \leq 1200\ \mu$L/hr) mixed results depending on the water flow rates: single size ($Q_{water} \geq 250\ \mu$L/hr), double sizes ($250 > Q_{water} > 100\ \mu$L/hr), and multiple sizes ($Q_{water} < 100\ \mu$L/hr). In the high-Q_{oil} region ($Q_{oil} > 1200\ \mu$L/hr), similar as in the medium-Q_{oil} region, the single drop size is produced at higher Q_{water}, and double drop sizes are produced at lower Q_{water}, but the boundary of two drop formation modes shows a linear decline in the Q_{water}-Q_{oil} phase diagram, as indicated by the solid line in the experimental results.

The process of single-size formation of droplets in the flow focusing microfluidic device, as seen in the evolving contour plots in **Figure 22**, can be qualitatively described as follows. The whole process is split into three stages, (1) elongation, (2) pinch-off, and (3) retrieving. In the (1) elongation stage, the two immiscible fluids (oil and water) form an interface at the junction of the center inlet and side channels. The upper part of the water tip largely keeps the same shape which has a near linear boundary between oil and water pointing from water channel walls toward the orifice. The lower part of the water tip, near the orifice, keeps growing with feeding water flow, hence forms a pointing nose advancing into the orifice. The pointing nose roughly takes at least ¾ of the width in the orifice. The (1) elongation stage takes about half of the time in a typical cycle. After the nose of the water tip penetrating into the orifice, the outside oil flow exerts pressure on the water tip and a neck of the water tip appears in the orifice. As the neck is getting narrower and narrower in the orifice, the upper part of the water tip above the orifice also becomes squeezed and narrower. Meanwhile, the water tip continues to elongate into the channel after orifice, where a spherical drop forms and grows with the feeding water flow. Eventually, a single drop is pinched off at the neck of the water tip, and this pinch-off stage takes about ¼ of the time in a typical cycle. After the (2) pinch-off stage, the water tip quickly recoils back to a triangular shape, and starts the last stage of retrieving. This stage takes the last ¼ of the time in a typical cycle, and in this stage the water tip no longer elongates but retreats a bit from the entrance of the orifice to the middle of the intersection of the central and side channels. The shape of the water tip

changes from a pointing triangular shape to a rounder elliptical shape, and finally the tip restores to the original state and starts the next cycle of drop formation.

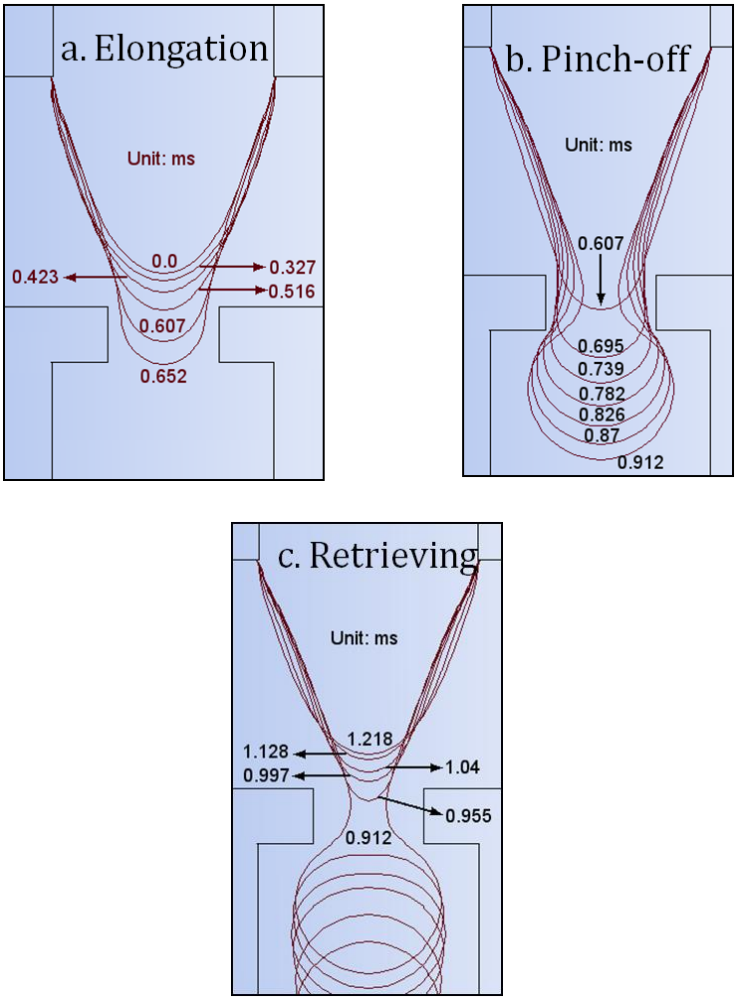

Figure 22 Evolving of the water tip contours in a typical cycle of single size drop formation. The contour lines are based on the simulation results in 2D cases at Q_{water} = 250 μL/hr and Q_{oil} = 1000 μL/hr. The whole process is split into three stages: (a) elongation, (b) pinch-off, and (c) retrieving. Numbers in the plot indicate the elapsed time of each contour line, starting from the beginning of the cycle and in the unit of milli-second (ms).

The process of double-size formation of droplets in the flow focusing microfluidic device is plotted in time-series frames in **Figure 23** and in the evolving contour plots in **Figure 22**. The process has similar (1) elongation and (3) retrieving stages, in which the water tip shape and length evolves in the similar manner, and also the time-elapses in these two stages take the similar percentage of the whole cycle as in the single-size mode. The difference from the single-size mode is that the pinch-off stage is split into two parts, (I) corresponding to the first bigger drop and (II) to the second smaller drop.

The pinch-off part (I) and part (II) as shown in **Figure** each takes about 1/8 of the time in a typical cycle of double-size drop formation. Comparing part (I) and part (II) in **Figure 24**, as well as the single size mode in **Figure 22**, the most significant differences are 1) the width of orifice opening occupied by the water tip, 2) the narrowing neck of the water tip, and 3) the location of drop pinch-off. For the occupation in the opening of the orifice, the single-size mode takes a great majority of the space in orifice, at least ¾ of the orifice width, and in part (I) the water tip occupies about ½ to ¾ of the orifice width during the drop formation of the first bigger one, less than the single-size mode, and in part (II) the water tip occupies less than ½ of the orifice width during the drop formation of the second smaller one, even less than that in part (I). Such difference between the single-size mode and the double-size mode is predictable since the water flow rate is smaller in double-size mode while oil flow rate is greater, the water tip will reasonably occupy less space of the orifice in the competing with outside oil flow. For the necking of the water tip and the pinch-off location, all the three pinch-off processes show that the narrowing neck starts to appear at the entrance of the orifice. However, the single-size mode and the part (II) in double-size mode share similar behavior that the neck of the water tip only shifts a small distance less than half of the length of the orifice, therefore the drop is pinched off nearly in the middle of the orifice. In contrast, in part (I) the neck of the water tip shifts from the entrance of the orifice to outside of the orifice, a distance longer than the length of the orifice, therefore the bigger drop is pinched off after the orifice, different from the smaller drop or the single-size mode.

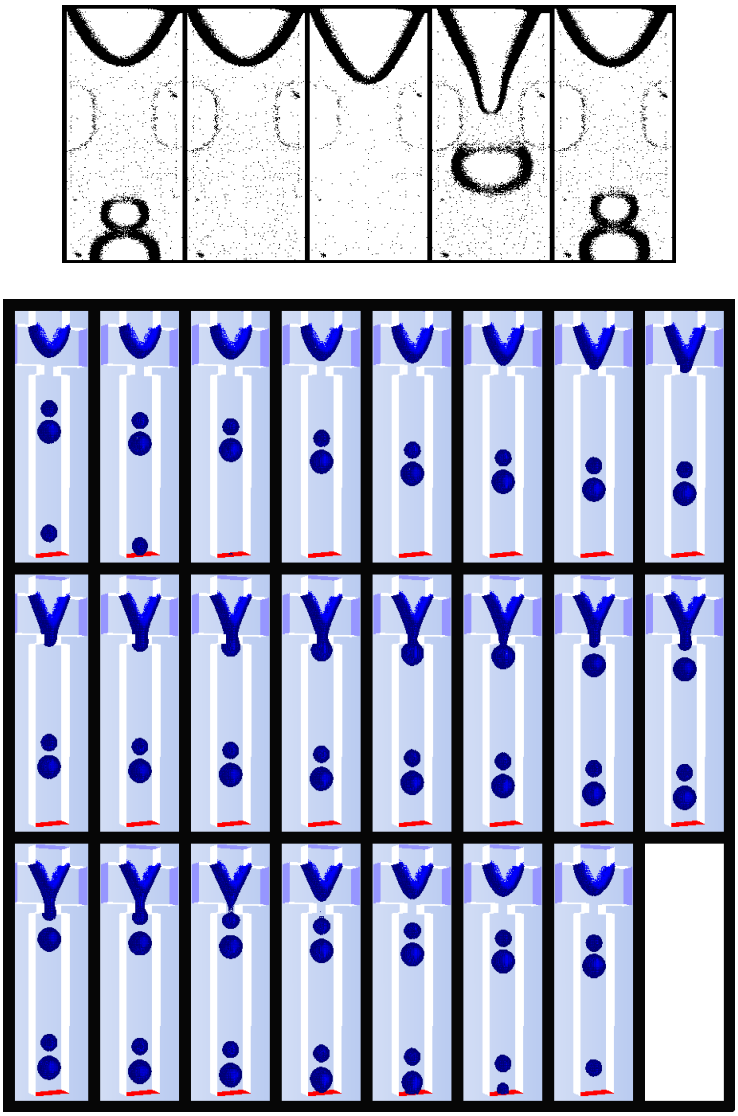

Figure 23. Serial frames of the double droplet oscillation as a function of time. (up) extracted from the experiments; (down) simulation results.

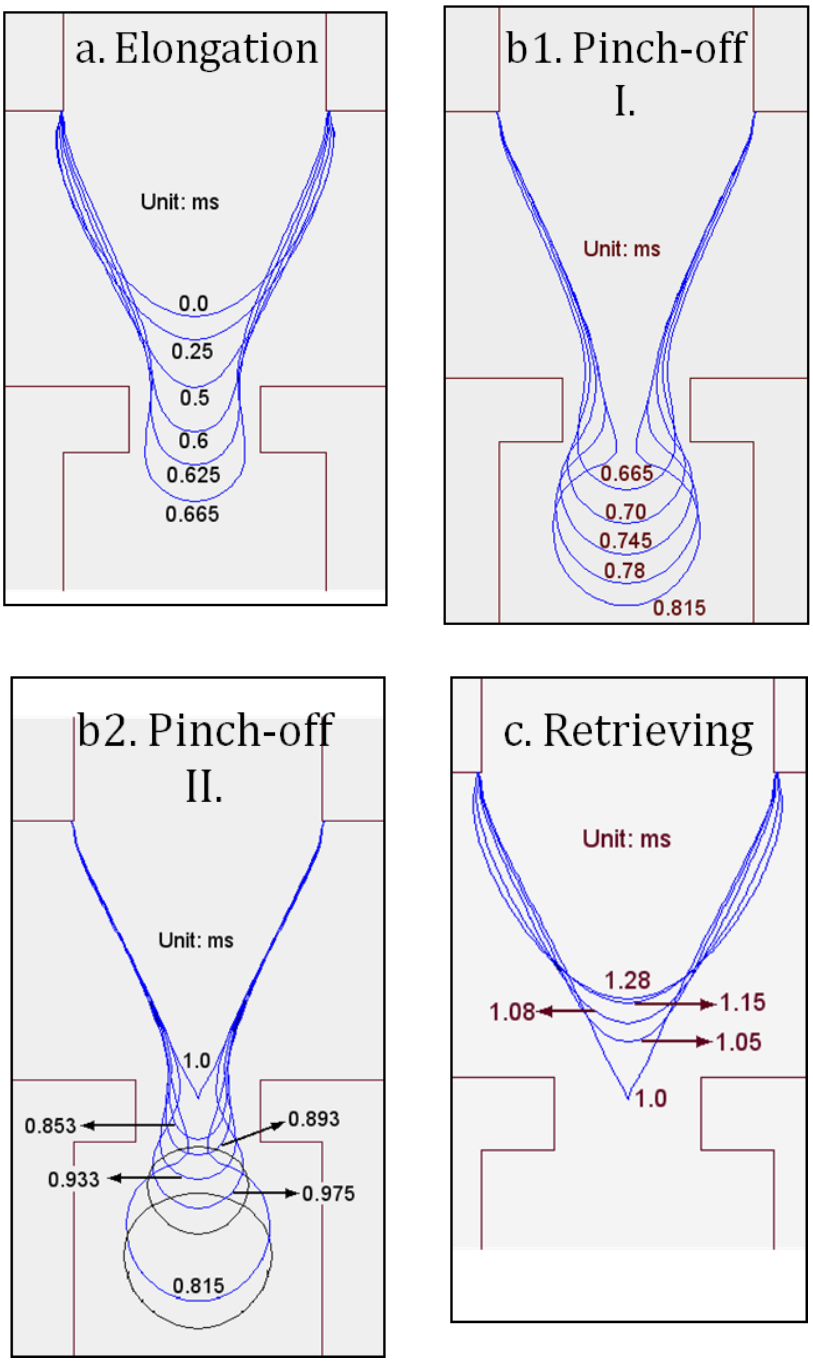

Figure 24 Evolving of the water tip contours in a typical cycle of single size drop formation. The contour lines are based on the simulation results in 3D case at Q_{water} = 150 μL/hr and Q_{oil} = 1200 μL/hr. The whole process is split into four stages: (a) elongation, (b1) pinch-off I., (b2) pinch-off II., and (c) retrieving. Numbers in the plot indicate the elapsed time of each contour line, starting from the beginning of the cycle and in the unit of milli-second (ms).

The different trends of droplet formation can also be reflected by their flow fields in the microchannel, as depicted by **Figure 25** and **Figure 26**. For the single-size mode, in the first subgraph of **Figure 25**, we can find that symmetrically there are two pair of vortex circulating in the water tip when the drop formation process begins, one pair is located at the corner of the water and oil input channel intersection, and the other is located in the pointing end of the water tip, near the middle of the intersection. The two pairs of vortex are independent to each other. The pair at the corner always exists in the whole process, which is induced by the sudden change of geometry and the beginning of contact between water and oil phases, and showing no relevance to the drop formation process. However, the pair of vortex in the end of tip periodically changes in the drop formation process. It initially shows up at the beginning of the process, but becomes smaller and smaller as the tip grows longer and approaches into the orifice (see the second subgraph of **Figure 25**) due to the confinement of the orifice and the squeezing of the oil flow. The dramatic change of flow pattern happens when the necking of water tip begins: the vortex in the end of tip disappears, replaced by a flow curved at the necking point, and the neck is getting narrower and narrower until the pinch-off. After the pinch-off the flow pattern changes back to have a pair of vortex, as shown in the third subgraph of **Figure 25**, and the size of the pair of vortex grows when the water tip retreats back to the original condition.

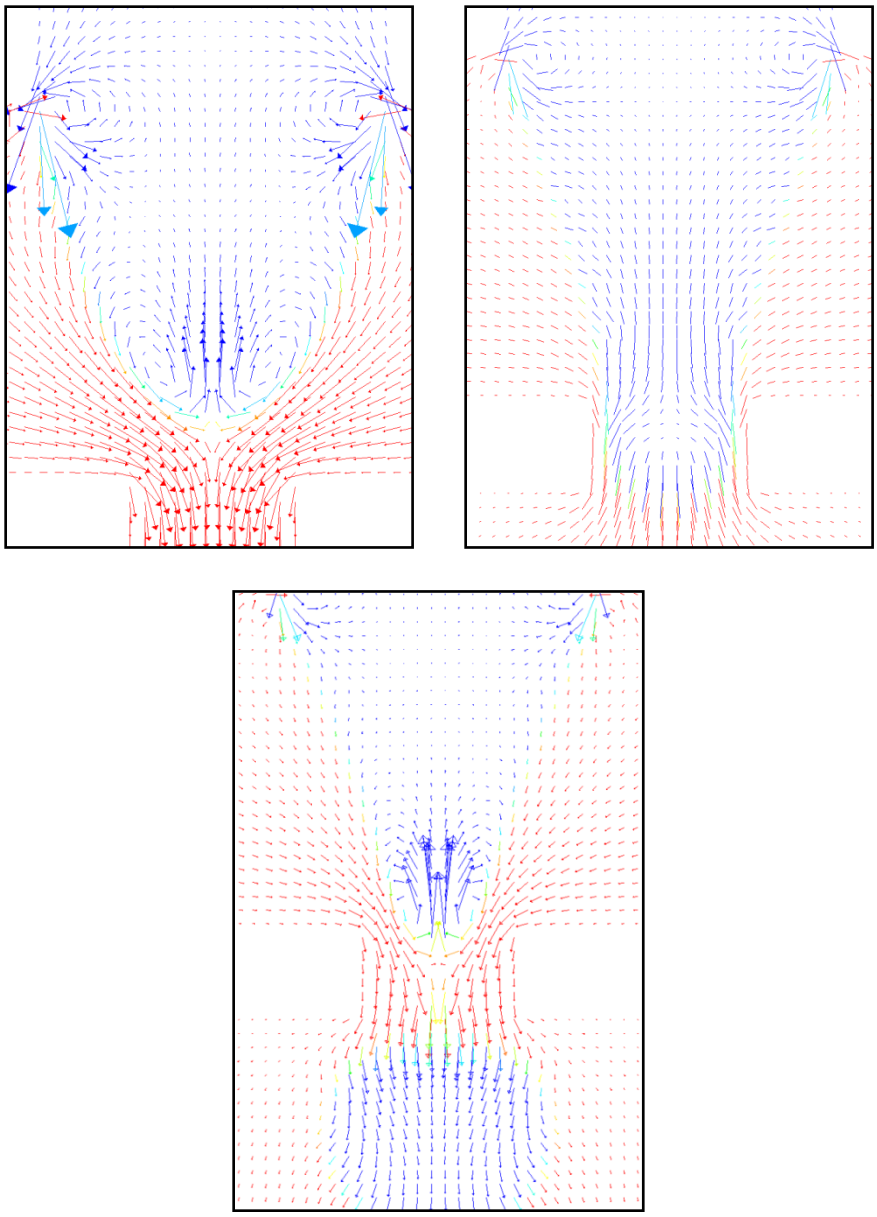

Figure 25 Velocity fields at different stages of single-size droplet formation corresponding to **Figure 22**. (top left) time = 0.0, (top right) time = 0.652, (bottom) time = 0.955

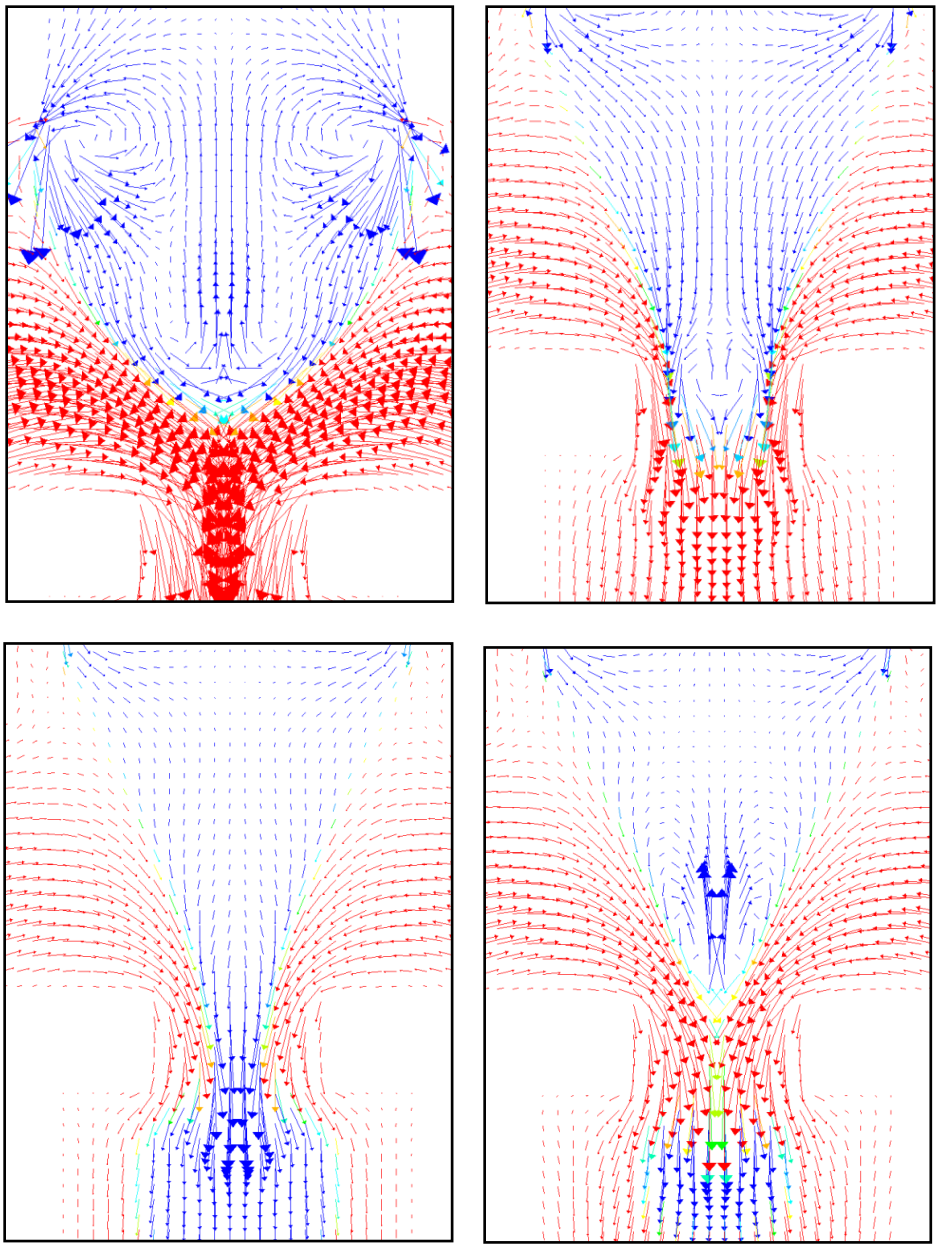

Figure 26 Velocity fields at different stages of double-size droplet formation corresponding to **Figure 22**. (top left) time = 0.0, (top right) time = 0.625, (bottom left) time = 0.815, (bottom right) time = 1.0.

Comparing to the single-size mode, the double-size mode has three different features. 1) In the beginning of the drop formation, the two pairs of vortex are not independent but

mingled together to form a complex circulation (see the first subgraph in **Figure 26**), which is probably due to the greater shear from the outside oil flow when the ratio of outside oil flow rate to inside water flow rate is bigger in this case. 2) Later, when the water tip is stretched and penetrates into the orifice region, the two pairs of vortex separate and the flow pattern is similar to the single-size mode. However, the vortex at the pointing ends of the water tip does not disappear at the same location as that in the single-size mode, i.e., there is still small vortex seen when the tip passes the orifice (see the second subgraph in **Figure 26**). This is corresponding to the previous analysis in the contour evolving, as the necking of the water tip travels to the downstream of the orifice, the transition of the flow pattern also happens later than the single-size mode, and in the downstream of the orifice. 3) After the pinch-off of the first bigger drop, the flow pattern switches back to have a pair of vortex. However, the water tip is now still in the stretched state, and confined in the orifice, therefore the size of the vortex is much small compare to that of the single-size mode (which pinched-off near the entrance of the orifice, and the after-pinch vortex is not confined by the orifice). Such small vortex cannot resist the outside oil flow, thus is quickly suppressed by the shear of the oil flow. In a similar flow pattern transition, the vortex in the end of the water tip disappears again and subsequently pinch-off of a second smaller drop. As the pinch-off of the second smaller drop is near the entrance of the orifice, the re-appearance of the after-pinch vortex is not confined by the orifice, similar to the single-size mode, which allows the retreating of the water tip and a reset in the system to begin the next cycle.

Another means to understand the difference between single-size and double-size modes is by the analysis of the pressure changes along with time, as shown in **Figure 27**. In the single-size mode as shown in the first plot of **Figure 27**: pressure quickly increase in (a) elongation stage, because the water tip penetrates into the orifice, competes and blocks the passage of the outside oil flow; in (b) pinch-off stage, the beginning of the necking inside the orifice opens up some space for the outside oil flow, therefore we can see a quick drop of pressure, which however is followed by a quick rising of the pressure because the spherical drop grows and blocks the exit of the orifice again until the pinch-

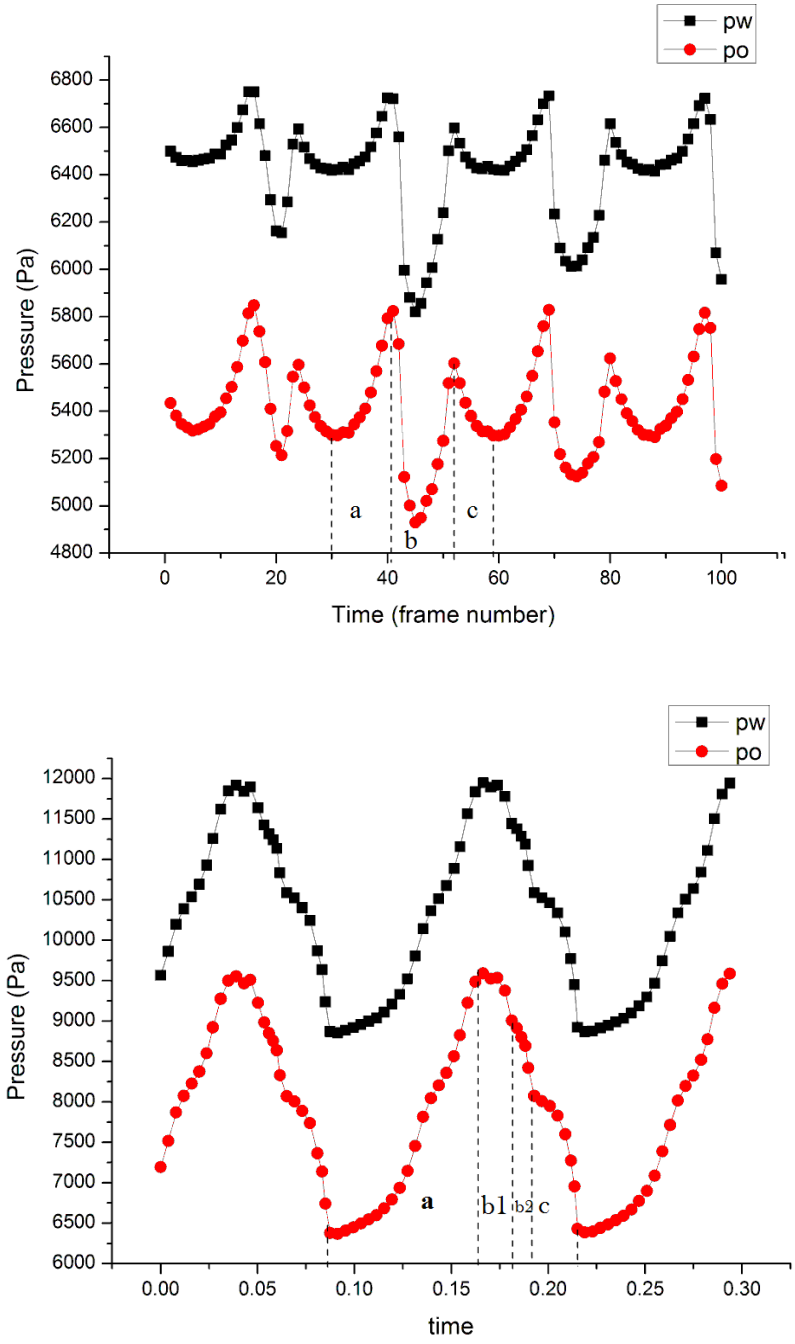

Figure 27 Pressure changes along time in the single-size mode (upper) and the double-size mode (bottom). The different stages corresponding to **Figure 22** and **Figure 24** is labeled in each subgraph.

off; and eventually the water tip has the (c) retrieving stage, in which we see a drop of pressure because the passage of the outside oil flow is no longer blocked at the orifice. In the double-size mode as shown in the second plot of **Figure 27**: the pressure undergoes a similar increase in (a) elongation stage; the (b1) pinch-off I. stage only has a small pressure drop comparing with the single-size mode because the tip is stretched much longer and the necking of the tip also travels to the downstream of the orifice, so the bigger drop is pinched off outside the orifice and the pinch-off doesn't open much passage for the oil flow in the orifice; only after the pinch-off of second smaller drop, the tip retreats and opens up the passage, and we see the final pressure drop back to the original state during (c) retrieving stage.

In a summary of the above analysis of the simulation results, the different deformation and elongation of the water tip under different flow rates result in different occupation of orifice space and pinch-off location, which in return change the outside oil flow and pressure, hence cause different drop sizes.

To study the dynamics in the droplet formation in flow-focusing microfluidic channels, the tip length l of the water stream is selected as a shape parameter to characterize the critical drop behavior, because the drop length strongly depends on the critical mode in this process, and also it is a convenient parameter to be observed and measured in both experiments and simulations. Previous study (**Figure 28**) shows that there is a critical length l_c, and if the water tip length $l < l_c$, a stable water tip shape can exists, but if $l > l_c$, no stable water tip shape could exist and it mush emit a droplet.

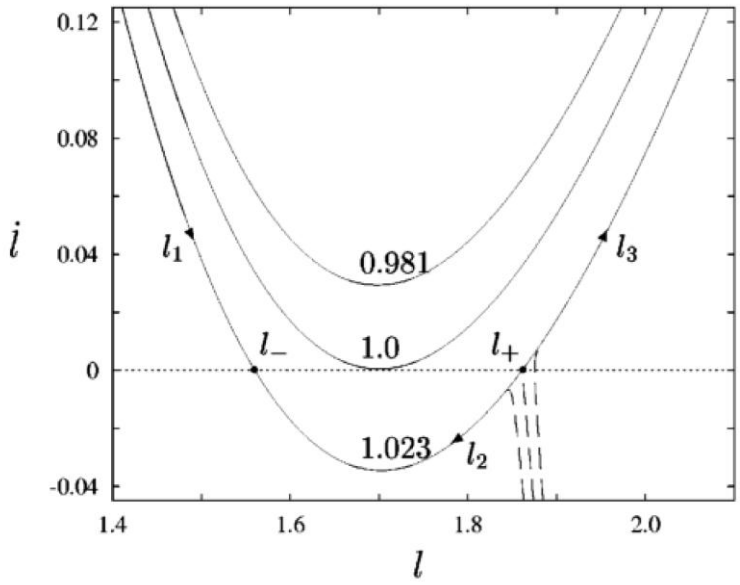

Figure 28 Rate of change of drop length versus drop length for viscous drop [130]. Long-time evolution (solid lines); short-time evolution for different elongated initial drop shapes (dashed lines). Values of dimensionless inverse capillary number is labeled. Reprinted with permission from J. Bławzdziewicz, V. Cristini, and M. Loewenberg, Phys. Fluid 14, 2709 (2002). Copyright (2002), American Institute of Physics.

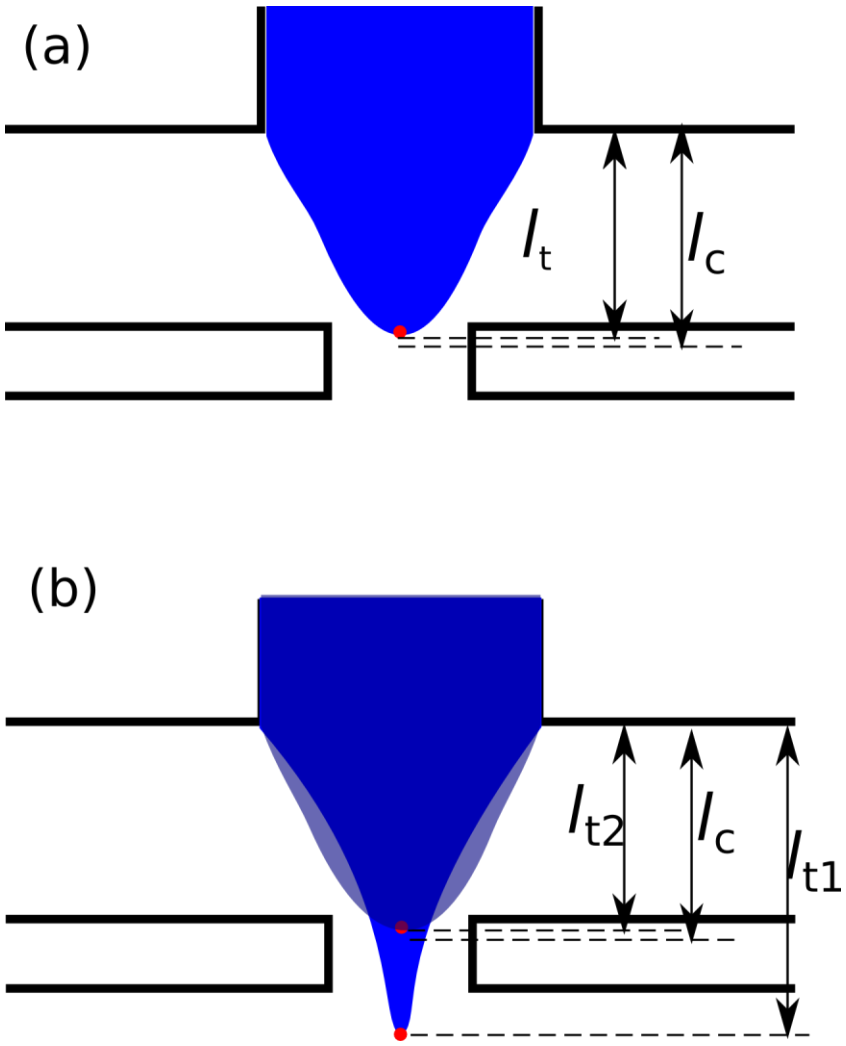

Figure 29 Sketches of the relationship between initial water tip length and critical length. (a) single-size dripping mode; (b) bimodal-size dripping mode.

With regard to the critical drop behaviors concerned in this study, the tip length l shows different patterns for the single-size dripping (before transition) and bimodal-size dripping (after transition), as explained in **Figure 29**. For the single-size dripping in flow focusing, the initial shape of the tip is almost fixed as observed in the experiments, and it shows a fixed initial position (labeled as l_t in **Figure 29a**) before the entrance of the orifice. Starting from length l_t, the water tip elongates and pinches off a droplet and after

the pinch-off the tip length remains around l_t without significant retreating. The whole system quickly returns back to initial conditions and with incoming water flow it starts the next cycle of droplet formation. Apparently, due to this stable pattern and according to the analysis above, this length l_t is smaller than the critical length l_c.

When the transition happens at reduced water flow rates, the velocity ratio between the outside oil flow and the inner water flow also increases, which results in increasing shearing exerted on the inner water tip, therefore the water tip is elongated much more than that in the single-size conditions (**Figure 29b**), and the shape of the water tip is no longer kept the same. A more deformed water tip propagates into the orifice, and a first drop is pinched off downstream near the end of the orifice. After the pinch-off, due to the increased elongation, the tip length l_{t1} (**Figure 29b**) is in the region of the orifice, still longer than the critical length l_c, hence the conditions is not fulfilled for the whole system to return back to starting point. Because the whole system is still in the unstable region in the saddle-node bifurcation analysis, the process of producing a second drop will be started instead of reset to the beginning of the first drop. Because the water flow rate is already reduced, it cannot support the second droplet size as big as the first one, and a smaller droplet is hence produced. After the pinch-off of the second smaller drop, the water tip length l_{t2} (**Figure 29b**) is further reduced and becomes smaller than critical length l_c, which allows the whole system to return back to original conditions and prepare for the next cycle.

Because the relationship between elongation and pinch-off of water tip with regard to the orifice is crucial to the drop formation mode, numerical studies are also conducted on varying orifice length in the flow-focusing channels at the same flow rates (**Figure 30**) to further investigate this impact. It is shown that by reducing the orifice length to half of the "normal" orifice ("normal" means the length as used in the experiments), at the same oil and water flow rates the droplet formation pattern is greatly changed. Only single-size dripping occurs which confirms the previous analysis, because the shorter orifice will not elongate the water tip as much as the normal orifice, therefore after pinch-off the

l_t will not exceed the critical length l_c, and the requirement is met to reset the whole system back to origin. In contrast to this, by doubling the orifice length, the bimodal pattern still occurs which is because the water tip is deformed more than that in the "normal" length, hence similarly needs to emit two drops for the water tip to retreat back to be smaller than l_c and reset the whole system. The flow fields under each orifice length condition are also shown in **Figure 31**, where it has the same behavior as analyzed in **Figure 25** and **Figure 26**. Based on this results, the orifice length needs cautious consideration in the design of the microfluidic flow-focusing channels since long orifice will tends to result in unstable droplet size, which is often avoided in various applications like particle synthesis and micro-chemical-analysis systems.

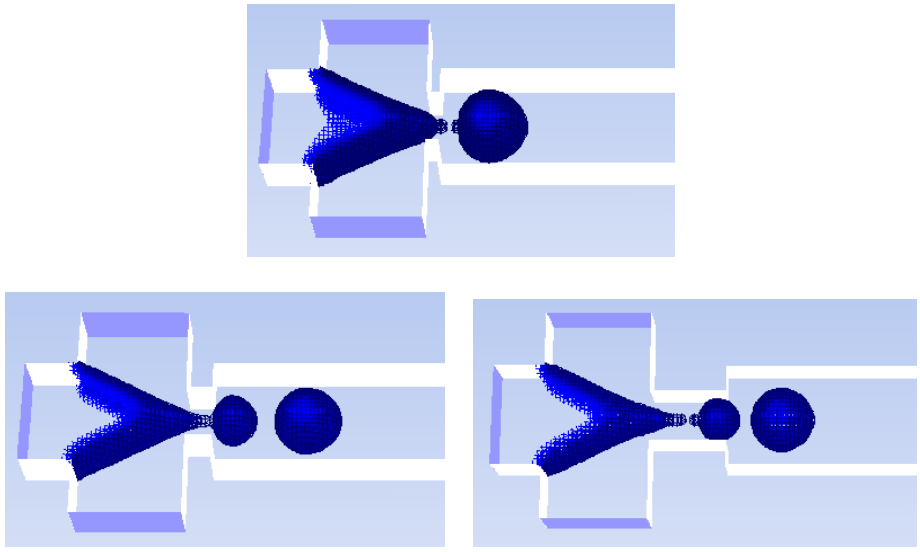

Figure 30 Numerical studies at various orifice length in flow-focusing droplet formation at the same flow rates. (upper) orifice length is half of that in experiments; (bottom left) normal orifice length as used in the experiments; (bottom right) long orifice length which is twice of that in the experiments.

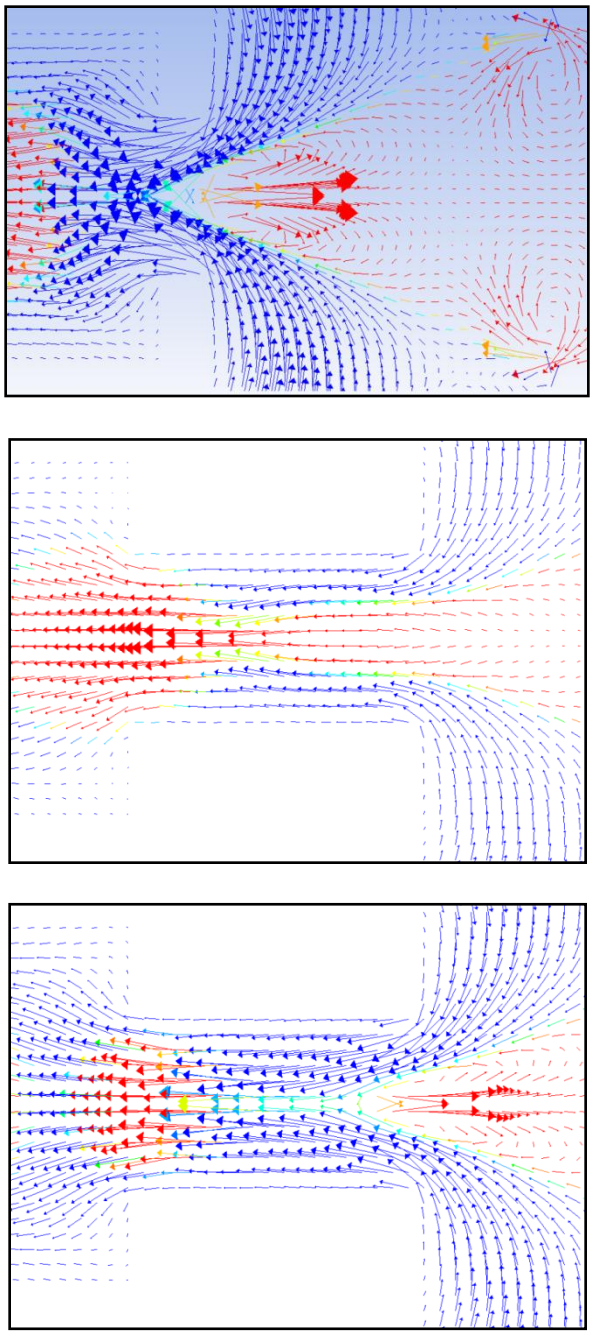

Figure 31 Flow field of various orifice length in flow-focusing droplet formation at the same flow rates. (upper) orifice length is half of that in experiments; (middle) normal orifice length as used in the experiments; (bottom) long orifice length which is twice of that in the experiments.

2.6. Conclusion

Microfluidics is increasingly received much attentions in the recent decade as its application in various scientific and engineering fields. The previous experimental observation of droplet size bimodal oscillation in microfluidic channels is confirmed by the simulation, and the numerical investigation of the dynamics of bimodal droplet break-up in the flow-focusing microchannel has revealed the evolution of water tip (the dispersed phase) with respect to a critical length which determines the saddle-node transition in the droplet formation. It is also found numerically that varying the orifice length in the channel design will have great impact in the patterns of the drop formation. The results may help the design and fabrication of microfluidic device, and improve the understanding of micro-scale flow behavior in related research.

3. AC ELECTRIC FIELD IN MICROFLUIDIC EMULSIFICATION

3.1. Summary

Applications of electric field, using either DC or high-frequency AC field, have shown many advantages in emulsification. We further develop this technique by a detailed study on low-frequency AC Electro-Flow-Focusing (EFF) microfluidic emulsification. Counter-intuitively, the droplet size variation is not monotonic with the electric field, in contrary to the DC-EFF emulsification. This phenomenon originates from a relaxation oscillation of flow rate through the Taylor cone. Particularly, a continuous droplet size decrease was obtained at voltage ramp-up stage. This emulsification process was modelled in analog to the accumulation and release of charges in an RC electric circuit with an adjustable resistor.

3.2. Introduction

Formation of droplets inside microchannels is an important component of microfluidics in various applications [1, 13, 15]. Flow focusing (FF) is a widely adopted method for monodisperse droplet generation in microfluidics, pioneered by Gañán-Calvo et al. [131] and Anna et al. [43]. It would be significantly beneficial if the droplet size could be tailored in a single device, especially for a liquid-liquid system of FF. Early experiments in drop-wise microfluidics simply varied flow rates or pressure for this purpose. Integrating electric fields into microfluidics has a great potential to rapidly control the droplet formation such as breaking, coalescence, and sorting [131-137].

Part of the data reported in this section is reprinted with permission from P. He, H. Kim, D. Luo, M. Marquez, and Z. Cheng, *Appl. Phys. Lett.* **96**, 174103 (2010).

Electrospray (ES) is an electro-hydrodynamic technique extensively used for mass spectrometry [138] and aerosol research [139]. ES and FF share many common advantages like robustness, simple set-up, large yield, as well as similar physical mechanisms such as jet formation and droplet pinch-off from a conic meniscus. Basaran et al. reported experiments and simulations on the electro-hydrodynamic tip streaming [132]. Gañán-Calvo et al. experimentally and theoretically explored the combination of ES and FF for aerosol production using a DC electric field [133, 134]. Chang et al. studied the cone stability and the morphology change in ES under a high frequency AC electric field [136, 137]. Mugele et al. integrated electrowetting into FF to study drop generation using an AC electric field [135]. So far, the majority of studies on an embedded AC electric field with FF used very high frequencies [135-137], and a low-frequency AC electric field is not well exploited in microfluidic emulsification. Here, we demonstrate the combination of a low-frequency AC electric field with FF for emulsification.

3.3. Experimental Setup

The water-in-oil emulsions were produced in an FF device under an AC electric field of triangular waveform (**Figure 32**), in a setup similar to our previous experiment [7]. We fabricated the polydimethylsiloxane (PDMS) device using soft lithography [42]. The source and ground electrodes were inserted into the PDMS in contact with the fluid to generate the electric field.

Distilled water was used as the dispersed phase (conductivity $K_W \sim 0.4\text{mS/m}$). Mineral oil (viscosity $\mu \approx 30\,\text{cP}$) with surfactant Span 80 (6% wt) was used as the continuous phase (interfacial tension $\sigma \approx 3\,\text{mN/m}$). Both water and oil were driven by syringe pumps (PHD2000, Harvard Apparatus, Holliston). Various flow rate settings were tested and they all showed the similar oscillation behavior. The results shown here are from flow rates $Q_W = 35\mu\text{L/hr}$ for water and $Q_O = 350\mu\text{L/hr}$ for oil. A high speed CMOS camera (Phantom V 4.2, Vision Research) was used to record videos of the

emulsification process. The water flow rate out of the Taylor cone, Q_j , is calculated using IDL® (ITTVIS, Boulder CO) by averaging the ratio (droplet volume)/(production time) over three neighboring droplets for each data point, where the error bar includes both measurement error and error from averaging (**Figure 33**, **Figure 34**, and **Figure 35**).

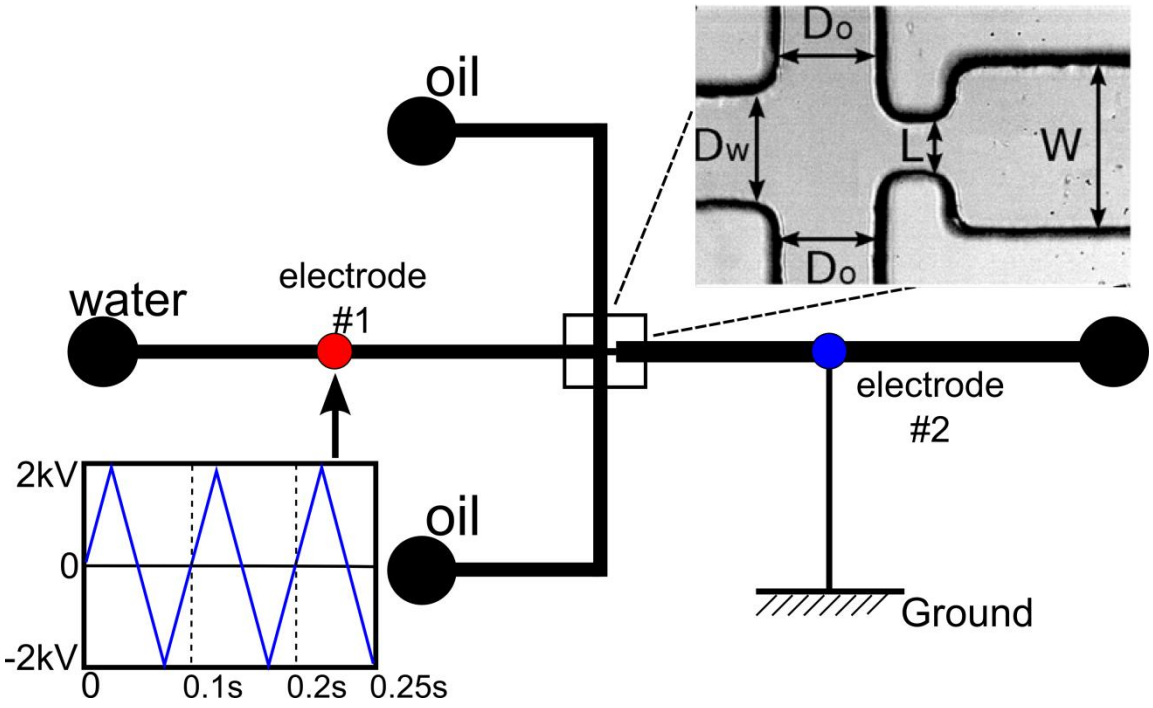

Figure 32 Scheme of AC electro-flow-focusing microfluidic device (top view). The distance between electrodes is 0.3645 cm. Triangular waveform of the AC electric field is shown in the lower-left corner. (Inset) zoom-in of the crossing junction with the dimensions: $D_w = 92.7\mu\text{m}$, $D_O = 83.6\mu\text{m}$, $L = 46.3\mu\text{m}$, $W = 140\mu\text{m}$, and the height of the channel is $h \approx 50\mu\text{m}$.

An image-processing program was developed in order to identify the droplet in the experimental images using Matlab (The Mathworks, Inc., Natick, MA) and IDL (ITT Visual Information Solutions, Boulder, CO). The video captured in the experiments were

converted to sequential images by IDL. The sequential images were smoothed by using Wavelet De-noise toolbox in Matlab, and then processed by a Matlab program using Hough Transform to locate the droplets in the images. The information of the droplet size was exported, and finally plotted in Origin V7.5 (OriginLab Corporation, Northampton, MA).

3.4. Results and Discussion

The periodic variation of droplet size under the triangular AC electric field is shown in **Figure 34** and **Figure 35**. Most interestingly, at the beginning of the voltage magnitude ramp-up stage, the droplet diameter D shows a continuous decrease (see **Figure 33a**; also A-C and J-L in **Figure 34**). The maximum droplet size is obtained at zero voltage, consistent with the results in a DC electric field [7]. The droplet diameter D shows a time dependence $D \approx \alpha / t$ (**Figure 33a**), where α is a constant and t is the experiment time ($t = 0$ at the voltage U = 0). The droplet production time τ was reported to be proportional to the jet diameter [140, 141], $\tau_n = \beta D_{n-1}$, where β is another constant and n labels the droplets in the sequence produced at the voltage ramp-up stage (n = 1 at U = 0). Hence, a discrete sequential model is built to approximate the observed continuous decrease of droplet diameter:

$$D_n = \frac{\alpha}{t_n} = \frac{\alpha}{t_{n-1} + \tau_n} = \frac{\alpha}{\alpha / D_{n-1} + \beta D_{n-1}} = \frac{\Gamma}{\Gamma / D_{n-1} + D_{n-1}} \tag{3.1}$$

Substituting the initial and final diameters in the droplet sequence, the parameter Γ is obtained as $\Gamma = \alpha / \beta \approx 1800$, and the droplet size reduction is predicted in good agreement with experimental data (**Figure 33b**).

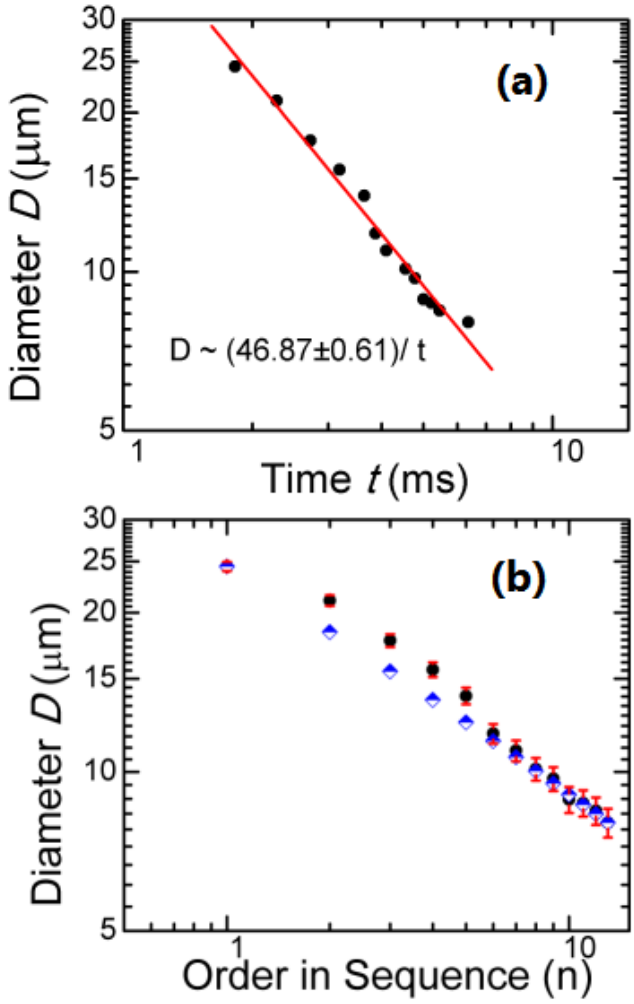

Figure 33 The decrease of droplet diameter in the series generated at the voltage ramp-up stage, corresponding to B or K in **Figure 34**. The open diamond symbols: the fitting values by equation (2.1). (a) The decrease of the droplet diameter with time. The red line is the fitting to $D \sim \alpha t^{-1}$. (b) The drop diameter variation along with its order in the sequence.

After the continuous reduction, we observe a group of droplets with roughly the same size (**Figure 34**, C-D and L-M), followed by a slight size increase until the peak voltage (F and O). The droplet size maintains a steady increase during the voltage ramp-down stage (F-I and O-R), similar to our previous DC experiment (**Figure 35**) [7]. Experimental observation (**Figure 34**) shows that the droplet formation process is only affected by the magnitude of the electric field, hence the direction of the electric field is not discussed further.

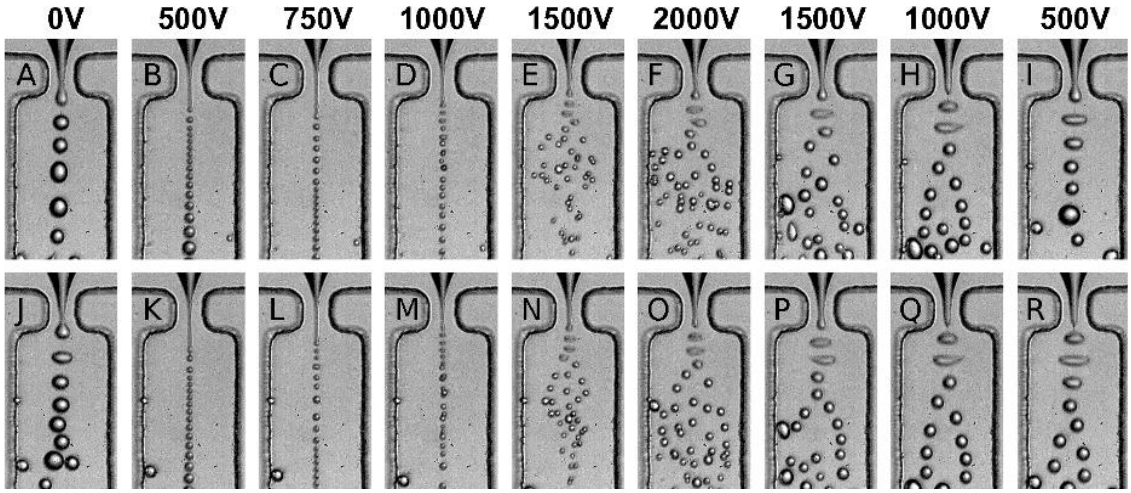

Figure 34 Droplet series generated using an AC electric field of triangular waveform. $Q_W = 35\mu$l/hr , $Q_O = 350\mu$l/hr . (a) Representative micrographs at various voltages. A-I: the first half period; J-R: the second half period.

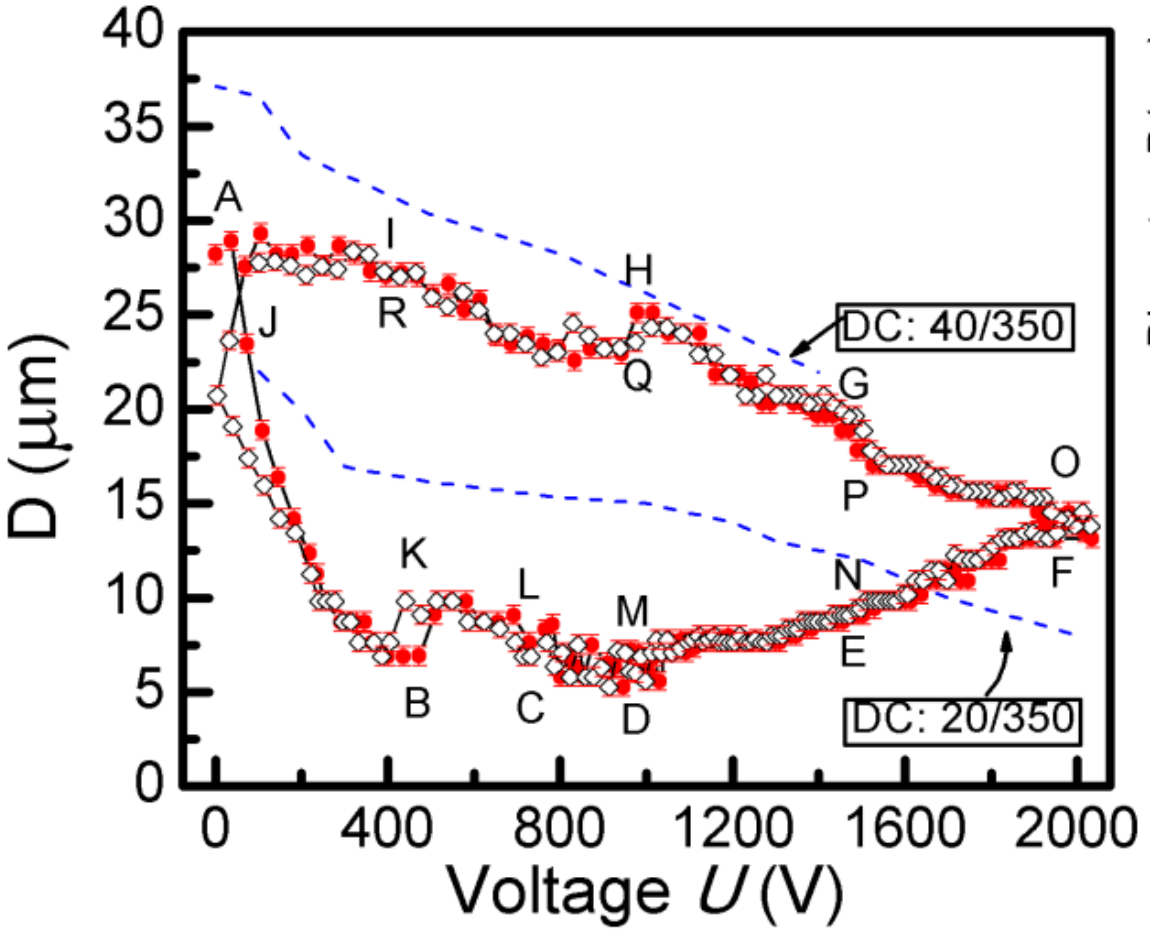

Figure 35 Droplet diameter D variation with the voltage U. Letters indicate the corresponding micrographs in **Figure 34**. Two dotted lines represents the comparable DC electro-flow-focusing results at $Q_W / Q_O = 40/350\left(\frac{\mu\text{L/hr}}{\mu\text{L/hr}}\right)$ and $20/350\left(\frac{\mu\text{L/hr}}{\mu\text{L/hr}}\right)$, respectively.

In contrast to the DC-EFF experiments [7], the water flow rate Q_j exhibits relaxation oscillation [128] in response to the voltage U of the triangular AC electric waveform (**Figure 36a**). Q_j quickly declines at the beginning of the voltage ramp-up stage, followed by a slow increase back to its original value when U returns to zero. This relaxation oscillation phenomenon can be explained using analogue to an RC electric

circuit (**Figure 37a**). Water influx Q_W is analogized to a constant current source I_{in}. An adjustable resistor $R_{E,C}$ represents the varying flow resistance of the jet issued from the Taylor cone. $R_{E,C}$ is controlled by both the electric field and the volume change of the cone. Q_j is represented by the current I_R passing through the resistor $R_{E,C}$. When U starts to ramp up, the increasing electrical field promptly closes up the passage of the water stream; hence, the jetting diameter gets smaller and smaller. As a result, water accumulates in the Taylor cone, which is similar to the charging up of a capacitor C. When $R_{E,C}$ becomes quite high at certain high voltages, the jet issued from the Taylor cone becomes so thin that the accumulated water in the Taylor cone cannot be held steady. Parallely in the analogy, the capacitor *C* discharges. Thus in the experiment, the Taylor cone begins to release the accumulated water to the jet. $R_{E,C}$ begins to drop due to the increase of the jet diameter, and Q_j switches from falling to rising. After the AC electric field passes the peak value and begins to decrease, $R_{E,C}$ keeps decreasing, evidenced by the increasing jet diameter or droplet size in **Figure 34** (F-I and O-R). Thus, the output flow rate increases due to the volume shrinkage of the Taylor cone. A resistor R_H represents the hydrodynamic resistance from the water input channel into the Taylor cone, which is quite small and does not affect the jet issued from the Taylor cone. We treat it as a constant.

The RC circuit model is verified in a simulator using Simulink (Mathworks, Natick, MA, USA) with respect to the experiment results (**Figure 38**). A current source $I_{in} = 35mA$ represents the water influx $Q_w = 35\mu L/hr$. $R_{E,C}$ is calculated by Poiseuille's law as $R_{E,C} \approx \lambda l / D^4 [\Omega]$ (**Figure 37c**), where the jet length l and diameter D are measured experimentally, and a proportional factor $\lambda \sim 3144$ is introduced for the current unit conversion from $\mu L/hr$ to mA (see **Figure 36a** and **Figure 36b**). The resistor $R_H \sim 0.994\Omega$ is determined similarly to $R_{E,C}$ but using the hydraulic diameter of the rectangular input channel.

From the scaling law analysis of droplet size in electrospray [134], we have $R \sim \rho Q_j^3 \varepsilon_0 / \sigma K^{1/6}$, where the density ρ, permittivity ε_0, and conductivity K are all constants. We measured drop size in the voltage ramp-up region, which indicates $R \sim t^{-1}$ (**Figure 34d**), and the flow rate in the same region, which indicates $Q_j \sim t^{-2}$ (**Figure 37b**). Therefore, we obtain $\sigma \sim t^0$, which means that the surfactant distribution is not affected by the electric field. Besides, the charge relaxation time is $\tau_C = \varepsilon_0 \beta / K_W \sim 0.186\ \mu$s, in which ε_0 is the vacuum permittivity and $\beta \sim 80$ is the dielectric constant of water. The period of the AC electric field is $\tau_{AC} \sim 0.1$ s. Since $\tau_C << \tau_{AC}$, the free charge relaxation is so fast that the change of charge distribution by convection is negligible and the charge equilibrium is instantaneously established in the jet issuing and the droplet pinch-off processes. The transient effect of the AC electric field on the viscosity and the surface tension of the fluids can be ignored.

Feeding these values to the RC circuit simulator, we reproduce the relaxation oscillation of I_R (in μA) in agreement with the experimental measurement of Q_j (in μL/hr), with an empirical parameter $C \sim 540 \mu F$ determined by trial and error (**Figure 37a**). We find that C increases, the current takes longer time to reach the stable oscillation, and C decreases, the current variation deviates from the experimental oscillation. Furthermore, the integral of Q_j is equal to that of the constant influx (35 μl/hr), which confirms the mass conservation. The overall flow rate in our AC experiments is merely an integral constant for each period. The relaxation oscillation is controlled by the voltage ramping, regardless of the averaged influx flow rate.

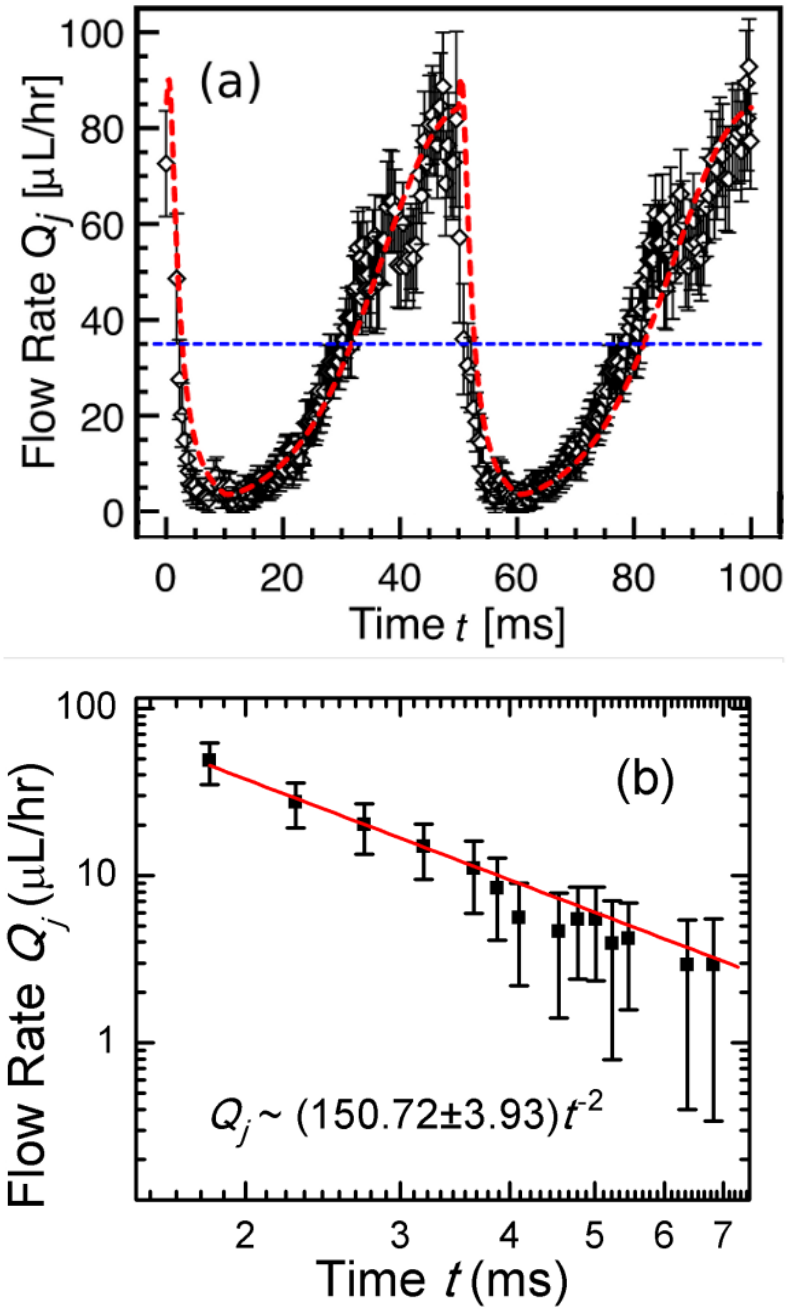

Figure 36 The flow rate variation with time. Dotted straight line (blue): the value of constant water influx. Dotted curve (red): the modeling results of I_R. (b) The flow rate decrease in the voltage ramp-up region. The red line shows the fitting by the scaling $Q_j \sim \eta t^{-2}$.

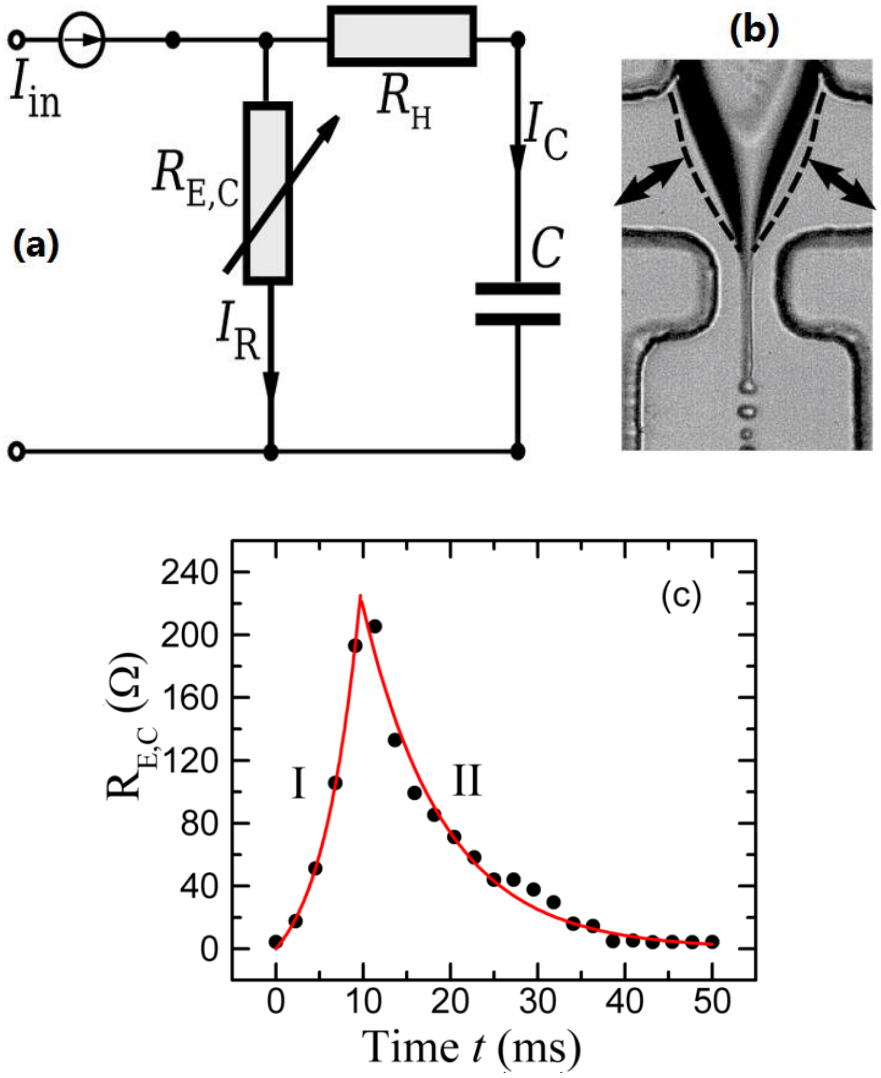

Figure 37 The relaxation oscillation of flow rate out of the Taylor cone in the low-frequency-AC-regulated emulsification. (a) The RC circuit model for low frequency AC regulated emulsification. (b) the volume variation of the Taylor cone as simulated by the charging and discharging of capacitor *C*. (c) The variation of the equivalent flow resistance $R_{E,C}$ with time. Solid lines are from the following fittings: $R_{E,C}^{I} = (28.97 \pm 3.44)[e^{t/(4.46 \pm 0.24)}-1]$ and $R_{E,C}^{II} = (217.59 \pm 8.99)e^{-(t-10)/(9.27 \pm 0.53)}$.

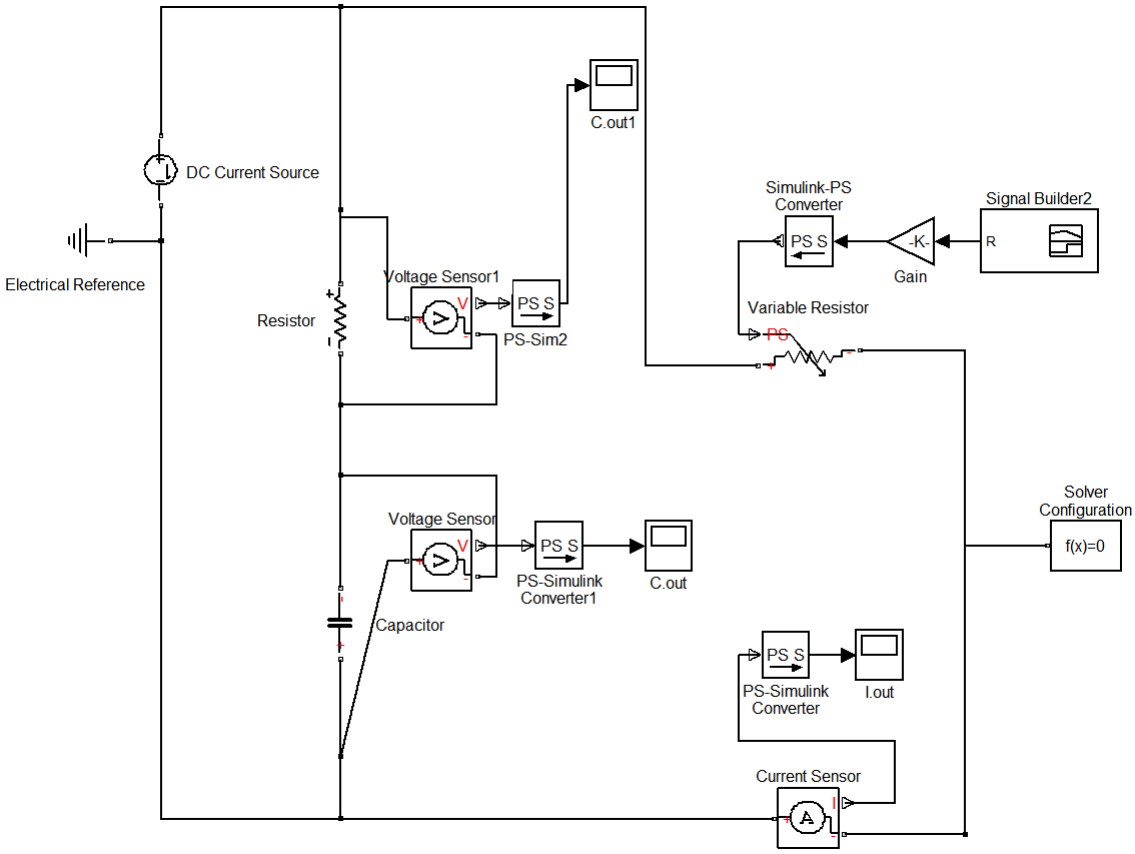

Figure 38 Simulink^{TM} flow diagram of the RC circuit model.

This nonlinear "RC circuit" characteristic is unique to the low-frequency AC electric regulation of microfluidic emulsification, leading to a closed loop in the size-voltage plot (**Figure 34b**). In comparison, the DC electric regulation only generates monotonic voltage dependence (see the dashed lines in **Figure 34b** from our previous DC experiments [7], in which the flow rates were close to those of our AC experiment). The water flow rate (35 μl/hr) was chosen to be low enough to avoid jetting at high voltage. The oil flow rate was chosen to offer sufficiently strong shear force to emulsify the water stream, in the mean time to avoid jetting. We found that the droplet size variation is mainly controlled by the strength of the electric field. Therefore, the relaxation oscillation phenomena will be better demonstrated using a linear ramping of the electric

field as in the triangular waveform , instead of the sinusoidal waveform. To verify this, two other waveforms of saw-teeth shape were used in the low-frequency AC-EFF emulsification for test.

Test waveform 1 was generated in 2 Hz, having a high-voltage plateau in the duration of 0.3 s and two ramps in the duration of 0.1 s between two cycles. The voltage reached its peak value of 2000 V at the top of the plateau, and linearly decreased to zero and increased to the peak value in the ramps, as shown in **Figure 39**. The result of the test waveform 1 is shown in **Figure 39**. The black line in in **Figure 39** shows the shape of the wave form. The red line in in **Figure 39** shows the variation of droplet size with the voltage oscillating, and the camera images sampling from the video are also shown corresponding to the blue points. In the high plateau region, uniform droplets were generated in a stable state. When it entered the ramping region, the droplet size endured an abrupt shrinkage, then quickly increased to its largest value, followed by another abrupt shrinkage, and finally restore to its stable size as the voltage become and maintained the high value. The relaxation oscillation behavior can still be noticed under this waveform, as shown in the middle of in **Figure 39**, the maximum and minimum of the droplet size were off the maximum and minimum of the electric field strength. However, on the flat plateau region, the droplet sizes remain the same, which indicates that the nonlinear behavior would not last for long period, but rather damped out quickly if the variation of the electric field strength ceases.

Test waveform 2 was generated in 5 Hz, having a high-voltage plateau in the duration of 0.06s, a zero-voltage plateau in the duration of 0.1s, and two ramps in the duration of 0.02s between the two alternating plateaus, as shown in the **Figure 40**.

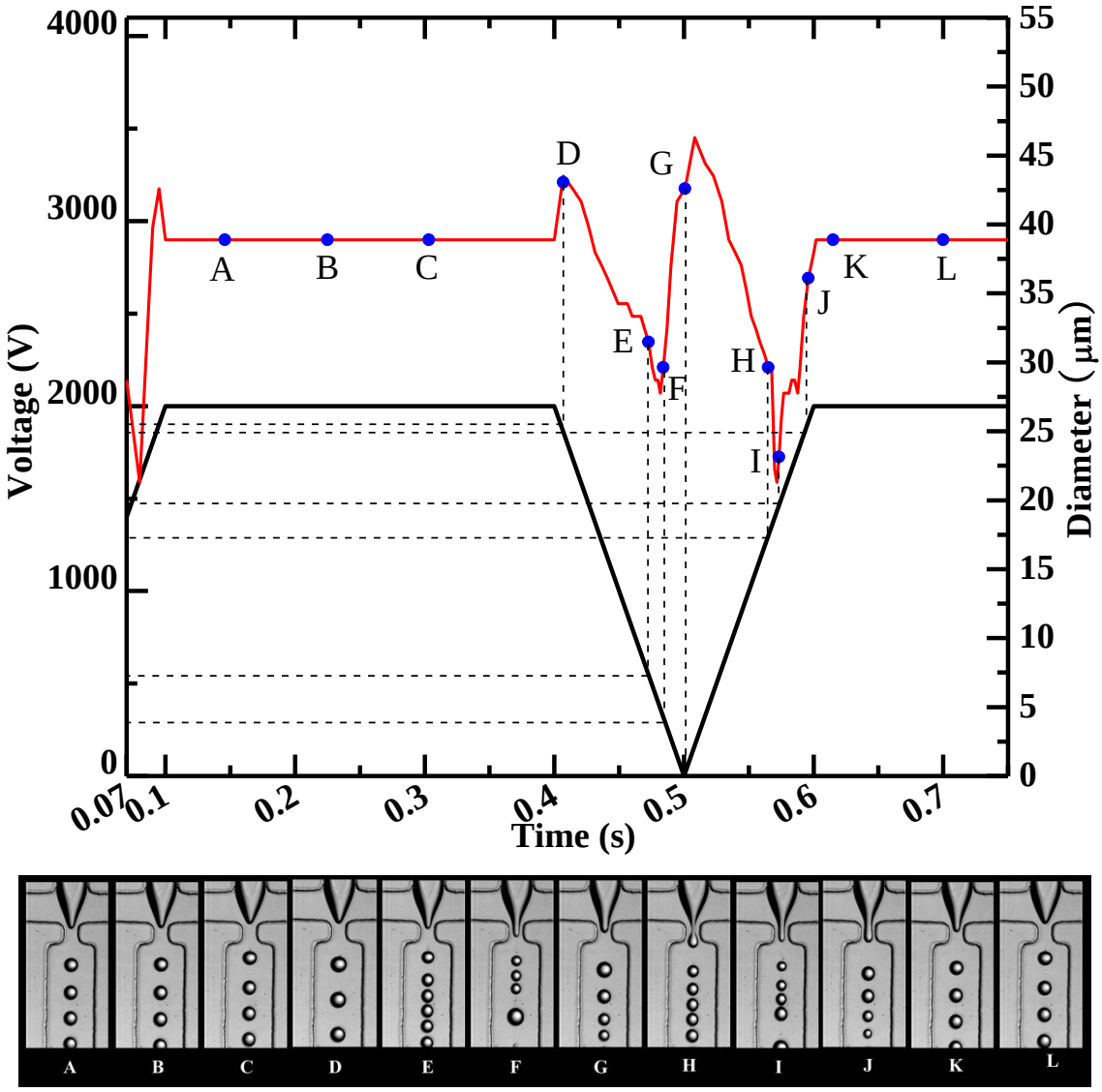

Figure 39 Droplet series generated using an AC electric field of test waveform 1. Q_W = 35μl/hr, Q_O = 350μl/hr. f = 2Hz. (Up) Drop size variation with time and voltage. (Bottom) key frames in video of drop formation in a typical period of AC electric field. The letters of each frame is shown in the upper plot.

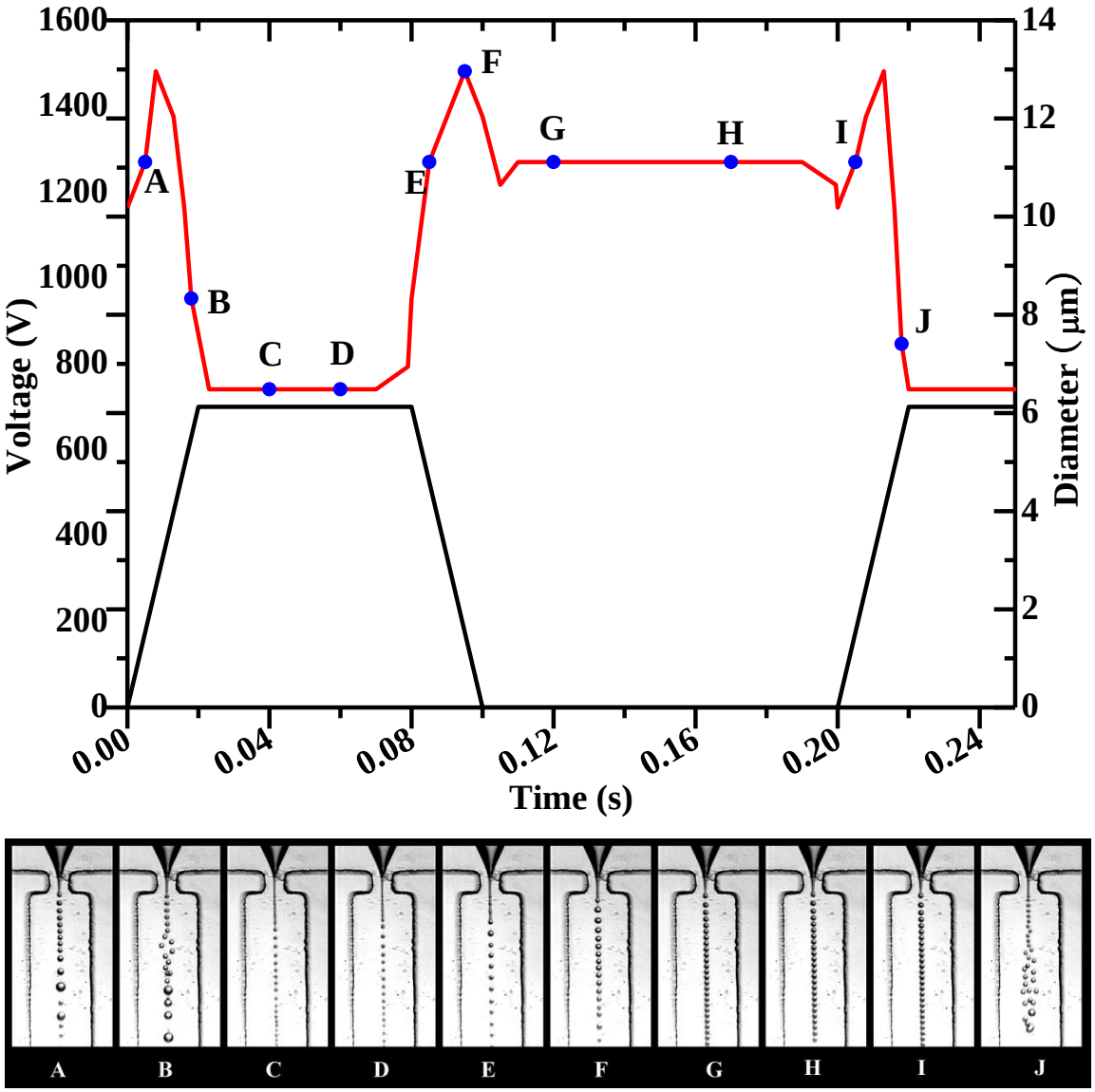

Figure 40 Droplet series generated using an AC electric field of test waveform 2. Q_W = 35μl/hr, Q_O = 350μl/hr. f = 5Hz. (Up) Drop size variation with time and voltage. (Bottom) key frames in video of drop formation in a typical period of AC electric field. The letters of each frame is shown in the upper plot.

Similar to the scenario in test waveform 1, the relaxation oscillation behavior was still noticeable in the test waveform 2, but it appears as if split into two halves, one corresponding to the down-ramp, and the other to the up-ramp. The difference with

regard to the test waveform 1 is that 1) the slop in the ramps is even higher, therefore the average drop size becomes smaller than that of the test waveform 1; 2) the weight of the ramps in the whole period of the cycle is less, therefore the relaxation oscillation is even less governing on the droplet size in the AC-EFF microfluidics.

Different coalescences could occur when the frequency is set to intermediate values. The coalesced droplets remain uniform in size and shape, and this may be useful to label, combine or mix droplets. **Figure 41** shows the coalescence of droplets under different frequency, in triangle wave form, at various frequencies, as shown in **Table 4**. Comparing drop size with regard to the low-frequency AC-EFF, the intermediate-frequency AC-EFF produces larger drops, especially after they coalescence. The drop size no longer varies with the AC electric field, as the previous time scale analysis shows, the AC frequency has become several magnitudes higher than that of the drop formation, hence the two processes decoupled in this sense. However, the coalescence indicates a change on the surface tension forces of the neighbor drops, which may related to the electro-wetting phenomena in the AC-EFF. In the classic AC electro-wetting theory [135], if the AC frequency exceeds the hydrodynamic response time of the droplet (for typical millimetre-sized droplets at frequencies exceeding a few hundred hertz), the liquid response depends only on the time average of the applied voltage, i.e. the RMS value. This statement is correct as long as the basic assumptions in the derivation of the basic equation are not violated. However, one of the basic assumptions that the liquid can be treated as a perfect conductor breaks down upon increasing the frequency. While the dissolved ions can follow the applied field at moderate frequencies and thus screen the electric field from the interior of the liquid, they are not able to do so beyond a certain critical frequency. Far below the critical frequency, the liquid behaves as a perfect conductor; far above it behaves as a dielectric. In our experiments, the low-frequency AC electric field is far below the critical value, hence we do not observe the effect of the frequency on the surface tension force. The intermediate frequency is close to the critical value (usually in the scale of several kHz for water), according to previous literature [135] the contact angle will increase with frequency, therefore we observed the

water drop will tend to coalesce to minimize the surface energy, and more drops will coalesce at higher frequency.

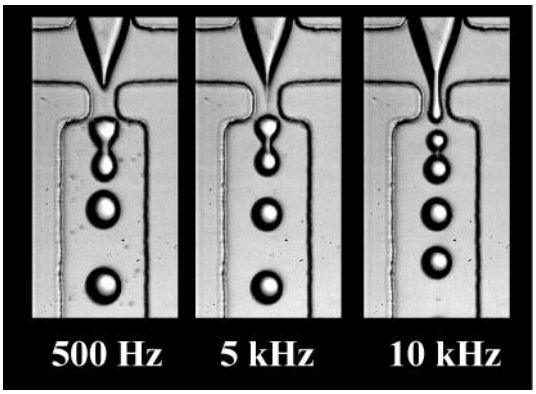

Figure 41 Snapshots of various coalescence patterns under different intermediate frequencies in AC-EFF. The flow rates of water and oil phases are the same as used in the low-frequency AC-EFF experiments, $Q_W = 35\mu$l/hr , $Q_O = 350\mu$l/hr . The frequency is labeled under each picture.

Table 4 Summary of coalescence patterns under various frequencies in AC-EFF.

Frequency (Hz)	Size Before Coalescence (μm)	Size after Coalescence (μm)	Coalescence Pattern	Coalescence Time Interval (μs)
500	51.1	64.4	2 to 1	8730
5000	50	61.1	2 to 1	7280
10000	43.3	60	3 to 1	5232.5

3.5. Conclusion

In summary, our results highlight the distinct response of the microfluidic droplet formation process to a low-frequency AC electric field. The flow rate from the Taylor cone exhibits a relaxation oscillation even though the averaged flow rates are constant. This nonlinear phenomenon originates from the competing control of the diameter of the

jet issued from the Taylor cone by the strength of the electric field and the volume of the Taylor cone. The relaxation oscillation of the flow rate is modeled using the analog of an RC electric circuit with an adjustable resistor. Using this AC microfluidic emulsification technique, we produced a continuously size-reducing droplet series by a simple triangular waveform. It would be promising to combine this rapid AC electric control with other lab-on-a-chip techniques on a microfluidic platform, such as using UV or chemicals to rapidly produce gel particles with variable sizes, and varying the quantities of reactive agents in the drop-based microreactors.

4. SEDIMENTATION OF COLLOIDAL DISKS

4.1. Summary

The first measurement of the hindrance function for sedimentation and creaming of disk-shaped colloids via the analytical centrifugation is reported. Disks align with the external flow right above the volume fraction of a few percent and this effect is extremely sensitive to the aspect ratio of disks. Due to this alignment effect, disk sedimentation/creaming demonstrate distinct trends in dilute and semi-dilute region.

4.2. Introduction

Sedimentation of colloidal particles involves in many natural and industry processes, such as in medical diagnostics [142], macromolecule morphology analysis [143], mineral processing, and environmental monitoring [144]. Understanding of sedimentation dynamics provides useful information for different physical phenomena in the suspensions such as phase separations [145], long-range velocity correlations [146], and epitaxial growth of colloidal crystals6. Sedimentation of spherical particles has been investigated for more than a century [71, 147], yet the sedimentation of anisotropic particles is less thoroughly studied, although anisotropic particles play important roles in many complex fluids [148]. Sedimentation of rod-like colloids is under the most investigations among anisotropic particles, in such topics as the sedimentation equilibrium of uniform tobacco mosaic virus [81] and sedimentation in mixture with polymers [149]. Anisotropic particle sedimentations demonstrated distinct characteristics

---

Part of the data reported in this section is reprinted with permission from (1) P. He *et al. Phys. Rev.E* **81**, 026310 (2010). Copyright (2010), American Physical Society. (2) A. F. Mejia, P. He, D. Luo, M. Marquez, and Z. Cheng, *J. Colloid Interface Sci.* **334**, 22 (2009). Copyright (2009), Elsevier.

due to the hydrodynamic interactions and long-range correlations, such as the formation of microstructure and streamer in settling rods and fibers at high Péclet number [150, 151], as well as the dependence on aspect ratio and orientation [152]. Among the anisotropic particles, discotic colloids arouses significantly interests due to the study of human red blood cells aggregation, clay platelets in soil and minerals [153], asphaltenes in petroleum production and refinery [154], and calcium oxalate crystals in the kidney stone [155]. Rheological properties of clay suspensions were intensively studied and important information about the hydrodynamic interactions and volume fraction dependence under shear flow was obtained [156]. Although this information is helpful, the knowledge and understanding of disk-like particle sedimentation behavior is still far from complete comparing to spherical and rod-like particle systems.

One of the most important sedimentation characteristics is the hindrance function, which describes the settling speed dependence on concentrations. For spheres with hard-core interactions, the first-order dependence on volume fraction ϕ, $U/U_0 = 1 - K\phi + O(\phi^2)$, with $K = 6.55$, was obtained analytically by Batchelor, assuming random distribution of particles and two-body hydrodynamic interactions [157]. Here the settling speed is normalized by Stokes velocity $U_0 = \Delta\rho g d^2/18\mu$, in which d is the diameter of the particle, $\Delta\rho$ the density difference between the particle and the solvent, g the gravity constant, and μ the solvent viscosity. This first-order dependence has been confirmed by experiments on hard spheres [145, 158]. Richardson and Zaki [159] correlated the sphere settling speed with ϕ in fluidized beds and particle suspensions by $U/U_0 = 1-\phi^n$, where empirical parameter n is around 4.65, and later Buscall et al. [160] modified n to 5.5 for wide ranges of volume fractions. Batchelor and Wen [161] obtained $U/U_0 \sim 1 - 5.6\phi$ for dilute polydisperse spherical suspensions, where the density variance is negligible in respect to the size variance.

For discotic colloidal particles, such dependence has not been systematically obtained either experimentally or theoretically. Capuani et al. [162] simulated charged discotic

colloids using a lattice-Boltzmann method. Kooij et al. [100, 102] investigated the phase transition of plate-like gibbsite colloidal suspensions with polydispersity up to 25% that showed an isotropic-nematic (I-N) transition around $\phi \sim 20\%$. The index K in analogy to Batchelor's formula was found to be greater for settling disks than rigid spheres using gibbsite platelets suspensions of $\phi < 5\%$, indicating a stronger backflow in disk sedimentation. So far, there are no data for discotic colloids sedimentation at high concentrations, $\phi > 5\%$.

4.3. Colloidal Disk Fabrication

The colloidal disk-shaped particles used in our experiments are α-eicosene (wax) particles and α-zirconium phosphate nanoplatelets (ZrP) [106-108, 163-165], whose properties are listed in **Table 5**. Various methods have been adopted to synthesize these colloidal disks, which will be briefly discussed in Section 4.

Table 5. Morphological properties of different disk samples. The aspect ratio of disk particles, ξ, is defined as the ratio between the diameter D and the thickness h. The aspect ratio of ZrP was determined by combining the measurement of TEM and X-ray diffraction (for the thickness) with DLS (for the diameter). The diameters of wax disks were measured by dynamic light scattering (DLS). Aspect ratios of wax samples were estimated by a conversion from the diameter ratio between the disks and the original emulsion droplets.

Sample	Diameter D [nm]	Thickness h [nm]	Aspect Ratio ξ
wax A	198.4 ± 47.8	72.67 ± 19.83	2.73 ± 0.35
wax B	152.9 ± 28.9	32.12 ± 7.15	4.76 ± 0.56
ZrP, non-exfoliated	350 ± 98	36 ± 5.5	9.0 ± 1.1
ZrP, exfoliated	350 ± 98	2.68	130.6 ± 35.6

4.3.1. Sample Preparation

The wax of α-eicosene (Sigma-Aldrich, St. Louis) was used as received, with 1% (w/w) of Stadis-450 (Octel Starreon, Newark, Delaware) added to increase electrical conductivity. A mixture of 200 ml of ethanol and water (80/20 w/w) was prepared, to which 0.005 wt% of Tergitol 15-S-9 (Sigma-Aldrich) and 20 mM of sodium dodecyl sulfate (SDS) was added. This mixture was used to collect the wax droplets in a 500-ml beaker.

For the analytical centrifugation measurements, wax disk suspensions were first concentrated to about 20% (v/v), and then diluted to a series of volume concentrations. The ZrP powder was used at different weight percentages, converted to volume fractions using ρ_{ZrP} = 2.55 g/cm^3. The suspensions were finally suspended in 1mM NaCl salt solutions via solvent exchange to screen the charge on the particle surface, and the resulting Debye screening length was estimated to be 9.7 ± 0.26 nm. Hence, the inter-particle interaction is assumed to be hard-core repulsion.

4.3.2. Electrospray

Liquid wax was introduced through a metallic needle using a syringe pump. An electric heater was used to maintain the temperature of α-eicosene above its melting point (26 ^{o}C). A digital signal generator (Model DS345, Stanford Research System, Sunnyvale, Calif.) and a high-voltage amplifier (Model 609E-6, Trek, Inc. Medina, NY) provided the required high electric voltage. The positive electrode was connected to the top end of the needle, beneath which was a grounded circular wire. The distance between the tip of the needle and the surface of the collection solution was kept constant at 7 cm. The solution was heated to adjust the density and surface tension of the collection fluids. A magnetic stirrer was used to homogenize the resulted emulsions. A stable Taylor cone was observed with a voltage range from 2.6 to 2.9 kV using a fast camera Phantom V4.2 (Vision Research, Wayne, NJ). For α-eicosene flow rate ranging from 1 to 30 ml/h, the jetting liquid from the cone broke into fine droplets with a fairly narrow size distribution.

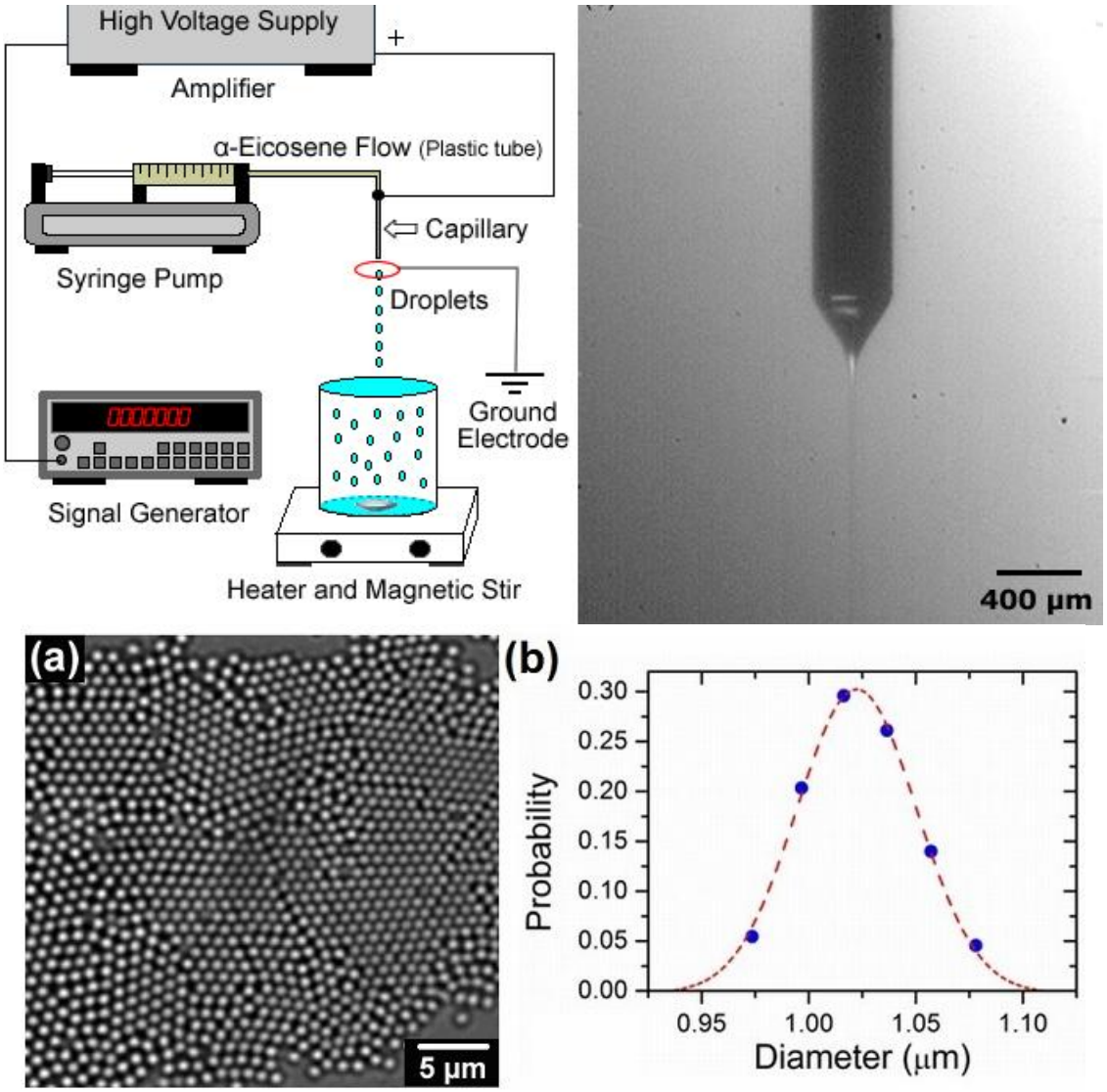

Figure 42 Experimental setup of electrospray [163].

Ethanol was added to the collection solution to match the density of wax, and was later evaporated at room temperature to reduce the solubility of α-eicosene. Before the evaporation of ethanol, another 160 ml of water was added to prevent aggregation arising from the increase of SDS concentration after evaporation. (SDS micelles will introduce depletion attraction between wax droplets.) By controlling the surfactant concentration, we were able to obtain stable emulsions. The sample was kept at low

temperature (4 ^{o}C), and checked frequently for morphological changes of wax particles using polarizing optical microscopy (TE-2000U, Nikon). The dynamic light scattering (DLS) measurement was performed on a ZetaPALS zeta potential analyzer (Brookhaven Instrumentation Corporation, Holtsville, NY).

4.3.3. Ultrasonication

The wax disks were made by ultrasonication emulsification followed by shape transition at 4 $^{\circ}$C, and various concentrations of sodium dodecyl sulfate (SDS) surfactant were used to tune the wax disk aspect ratio.

4.3.4. Capillary Microfluidics

Uniform wax emulsions were generated using a glass microfluidic device with flow focusing geometry [45]. α-eicosene wax dissolved in chloroform was used as the dispersed phase. De-ionized water with sodium dodecyl sulfate (SDS) as surfactant was used as the continuous phase. The glass device was employed because it provided the required hydrophilic wetting properties to produce oil-in-water (O/W) emulsions in this experiment. The design of the glass microfluidic device is illustrated in (**Figure 43**), showing the con-axial cylindrical and square glass capillaries. The wax solution was pumped into the center channel of the device; the aqueous SDS solution was pumped into the outside channel. When the flow of wax solution passed through the orifice, it ruptured to form droplets of uniform size. The size of the drops, typically 50 microns, can be controlled by the opening of the cylindrical capillary tip, and further fine tuned by varying the flow rate ratios. The polydispersity of the emulsion drops is less than 3%.

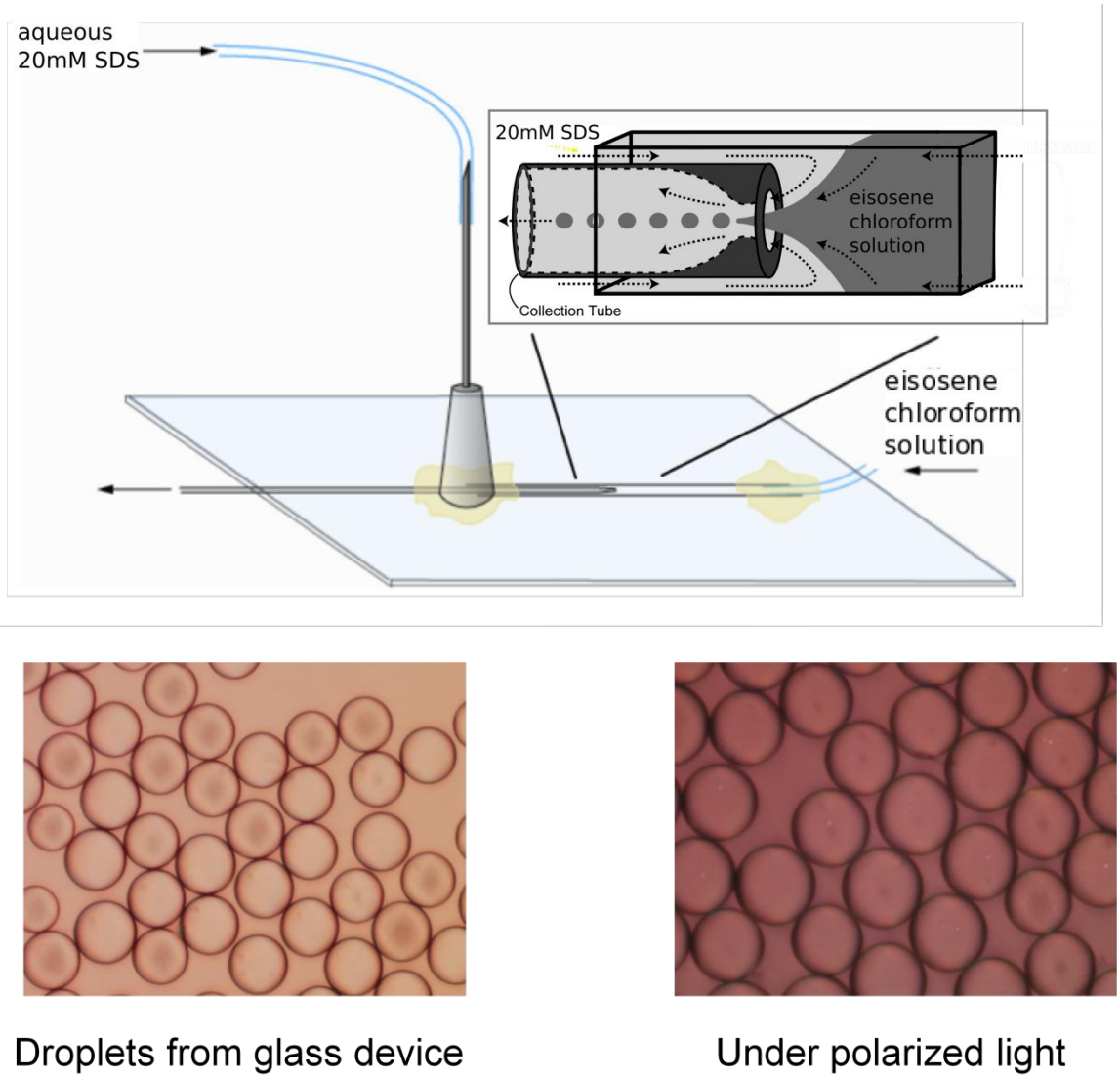

Figure 43 Illustration of the glass microfluidic device to produce uniform wax droplets in aqueous suspensions. (Inset) Zoom-in of the flow-focusing geometry. Arrow on the right shows the in-flow of the α-eicosene in chloroform solution. Circles in the middle represent the produced chloroform emulsions, which are then collected at the exit end of the inner capillary.

The whole process of shape-forming is illustrated in **Figure 44**. Uniform emulsion droplets were collected and spread on the bottom of a glass petridish to form a monolayer of droplets, covered with a thin layer of 20 mM SDS aqueous solution. Then,

the droplet monolayer was allowed to evaporate at room temperature T = 22 ^{o}C. Chloroform is volatile and slightly soluble in water, with density $\rho_{ch} = 1.483$ kg/cm^3 and a solubility of 8.22g/kg at room temperature. Due to the surface energy barrier, only the bigger wax particles can "snap into" the chloroform-water interface, and then transferred across the interface in the aid of SDS surfactants. Finally, the transfer to disk shape of the wax particles was achieved by defect annealing at 6 ^{o}C, under which the wax molecules undergo surface freezing and assemble from isotropic phase to rotator phase.

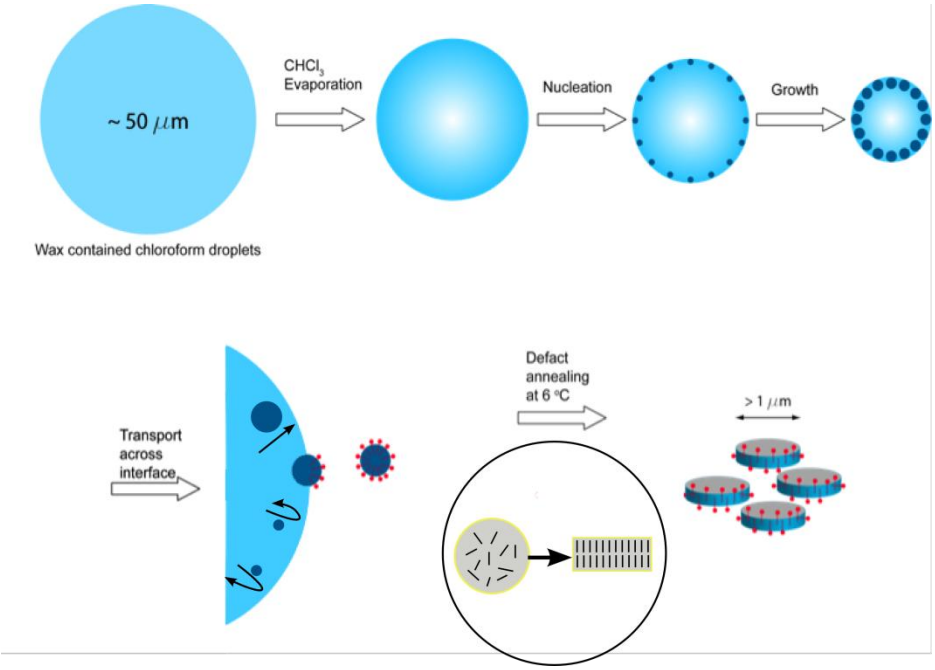

Figure 44 Illustration of the fabrication process of micro wax disks via two-step emulsification.

4.3.5. Hydro-Thermal Reaction

The ZrP nanoplatelets were synthesized by hydrothermal reactions [164, 165] and utilized to obtain data for higher aspect ratio disks ($\xi > 5$). The extremely high aspect

ratio disks were prepared by exfoliating the ZrP into monolayer platelets in an aqueous solution using tetra-n-butylammonium hydroxide (TBA) at the stoichiometric ratio where the entire ZrP surface was covered by a monolayer of TBA molecules.

4.4. Characterizations and Data Analysis

The aspect ratio of wax disks, ξ = diameter / thickness, was determined by comparing its diffusion coefficient to that of the equal volume spheres. The diffusion coefficient D^*_{disk} of wax disks was first measured, then the wax disks were heated to become spherical droplets and the diffusion coefficient D_{sphere} was measured. The radius of the spheres can be calculated using

$$r = \frac{k_B T}{6\pi\mu D_{sphere}}. \tag{4.1}$$

Here, T is the temperature, k_B is the Boltzmann constant, and μ the solvent viscosity. For a cylindrical disk of thickness t and diameter $2R$, $\xi = 2R / t$. and D^*_{disk} is approximated by the formula for oblate ellipsoids with the same aspect ratio and thickness [166],

$$t = \frac{k_B T}{3\pi\mu D^*_{disk}} \frac{\arctan\sqrt{\xi^2 - 1}}{\sqrt{\xi^2 - 1}}. \tag{4.2}$$

Since the density difference between the wax solid and liquid is negligible, we can assume that the volume does not change during the shape transition from a cylindrical disk to a sphere [100], i.e.

$$\frac{4}{3}\pi r^3 = \pi R^2 t = \frac{2\pi R^3}{\xi}. \tag{4.3}$$

Combining the equation (4.1)-(4.3), we obtain the equation for determining the wax disk aspect ratio ξ,

$$\left[\frac{\arctan\sqrt{\xi^2-1}}{\sqrt{\xi^2-1}}\right]^3 \xi^2 = \frac{2}{3}\left(\frac{D^*_{disk}}{D_{sphere}}\right). \tag{4.4}$$

The approximation of an oblate ellipsoid is adopted to calculate U_0, the terminal sedimentation/creaming speed of a single disk. For a disk with thickness 2b, diameter 2a and $\xi = a/b$, the anisotropic translational friction coefficients are given by

$$f_{\parallel} = 16\pi\mu \frac{b^2-a^2}{2b^2 - a^2\ \ S - 2b}, \tag{4.5}$$

and

$$f_{\perp} = 32\pi\mu \frac{b^2-a^2}{2b^2 - 3a^2\ \ S + 2b}, \tag{4.6}$$

where subscripts $\parallel$ and $\perp$ denote parallel and perpendicular directions to the principle symmetrical axis of the disk, respectively, and

$$S = \frac{2}{\sqrt{a^2-b^2}} \arctan\left(\frac{\sqrt{a^2-b^2}}{b}\right), \quad \text{for } b < a. \tag{4.7}$$

Hence, the averaged friction coefficient for random-oriented sedimentation/creaming is

$$f_{eff} = \frac{3}{\left(\frac{1}{f_{\parallel}} + \frac{2}{f_{\perp}}\right)}, \tag{4.8}$$

and

$$U_0 = \frac{2\Delta\rho\pi a^3 G}{f_{eff}\xi}, \tag{4.9}$$

where G is the centrifugation acceleration.

Sedimentation/creaming speeds were measured by the analytical centrifugation analyzer LUMiSizer® (LUM Corporation, CO) [167-169] (**Figure 45**). Similar instrumentations have been utilized in the characterization of gibbsite platelets [100]. The temperature of the measurement was all set at $T = 22 \pm 0.4\ ^{\circ}\mathrm{C}$ except for the spherical wax emulsions, which were measured at $T = 30 \pm 0.4\ ^{\circ}\mathrm{C}$, above the melting temperature of α-eicosene, $T_m = 26\ ^{\circ}\mathrm{C}$. The sequential space and time transmission profiles of wax disk suspensions in a single measurement at a typical rotation speed of 4000 rpm are shown in **Figure 46a**. The migration of particles led to the formation of an opaque sedimenting/creaming layer (low transmission) and a clear liquid layer (high transmission). All samples were well mixed right before the sedimentation/creaming measurement. The transmission profiles in the analysis were chosen at the beginning of the time elapse (within 20min from the starting time) such that they presented the initial volume fraction in the uniform mixture, before the significant volume fraction increase and the emerge of large-scale microstructure. The positions of the suspension-solvent interface were tracked at a specific transmission value marked by the horizontal dash-dot line in **Figure 46a**, determined by the geometric mean of the highest and lowest value of transmission. The sedimenting/creaming speed was calculated from the slope of the position vs. time plot using the specialized data analysis software provided by LUM Corporation, as shown in **Figure 46b**. An apparent slight spreading of the interfaces in **Figure 46a** was due to the relatively large polydispersity in our sample (~30% for ZrP and ~25% for wax, measured by DLS), and the analysis of this polydispersity effect revealed that it could increase the number averaged coefficient of sedimentation by a factor of $(1 + 2\sigma^2)$, where σ is the polydispersity of the samples, thus about 18% for ZrP and 12% for wax [100].

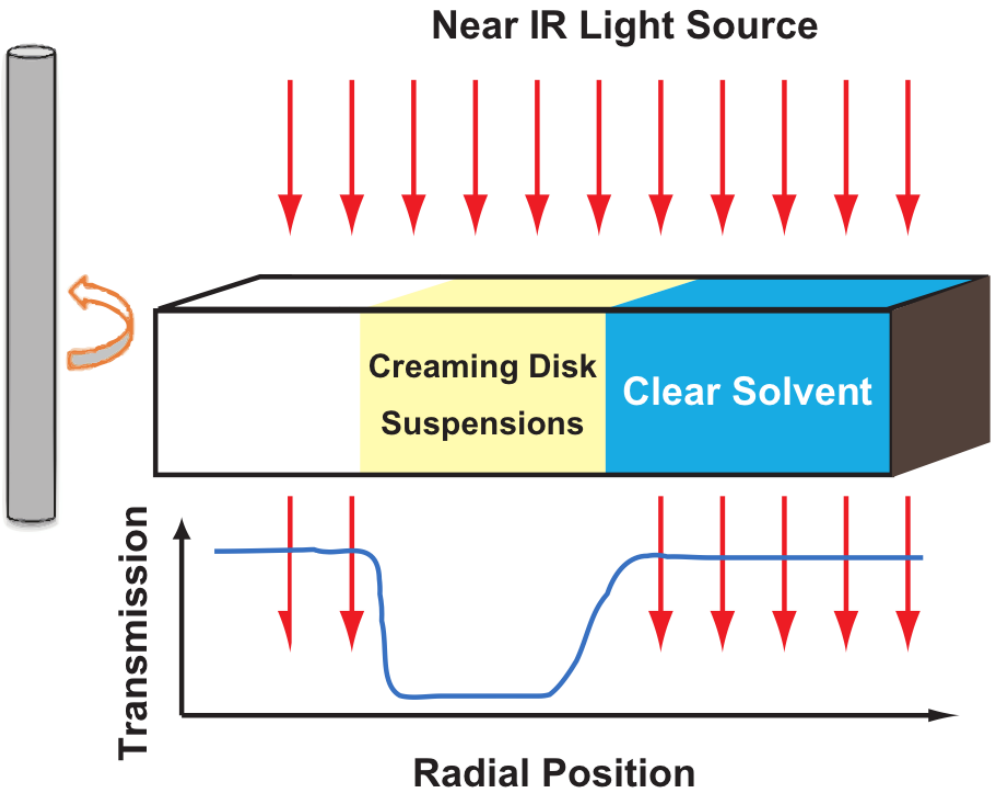

Figure 45 Creaming of colloidal disks in an analytical centrifuge. The apparatus consists of a cell chamber, a centrifugal rotor, a pulsed near-infrared light-emitting diode (880 nm) as light source, a charge-coupled device line (CCD-Line) as the light collector. Extinction profile measurements are obtained instantaneously across the whole sample range with a physical space resolution of less than 10 microns. Suspensions were pipetted into special poly-hydrocarbon measurement vials, and the sample volume was adjusted to 10 × 25 × 2 mm^3 in weight × length × height.

4.5. Results and Discussion

The measured dimensionless sedimentation/creaming speed U/U_0 is plotted in **Figure 47a**. The terminal sedimentation speed of a single disk is calculated in approximation of an oblate ellipsoid with the same thickness and diameter (c.f. Appendix) [36]. Data for spherical droplets is also shown for comparison. Error bars of the speeds are based on the linear fitting error of the solvent-suspension interface position tracking (**Figure**

46b). The error in volume fractions is calculated from sample preparation procedure. All measurements show that the normalized disk sedimentation/creaming speed is remarkably slower than that of spheres at the same volume fraction. In particular, we observe two distinct sedimentation/creaming trends for dilute and semi-dilute disk suspensions (**Figure 47**).

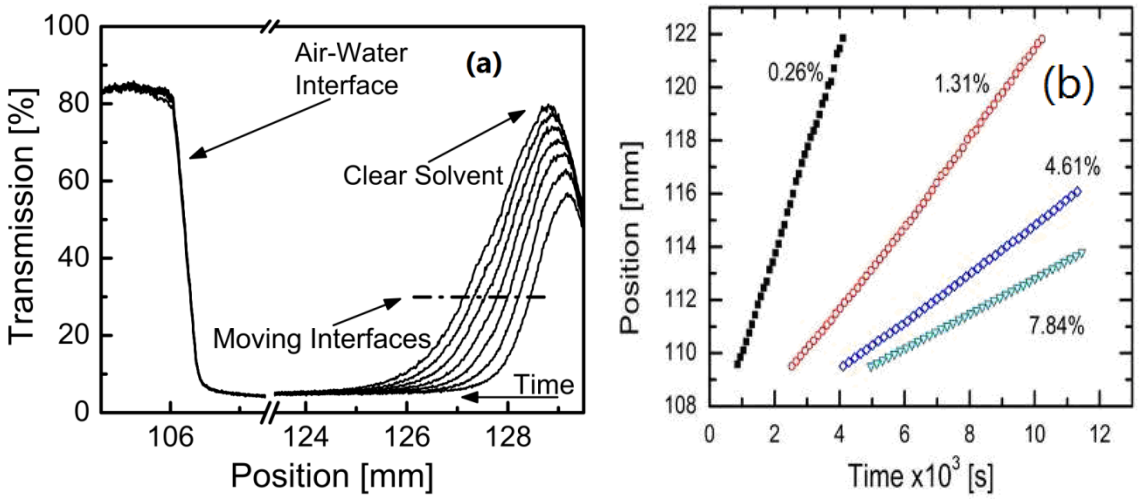

Figure 46 Analytical centrifugation measurements. (a) Sequential time transmission profiles, where the dash-dot line in the center represents the transmission intensity for tracking the position of solvent-suspension interface. (b) Measuring the radial position of the solvent-suspension interface as a function of time and the slope yields the sedimentation/creaming speed. The initial volume fractions ϕ_0 are labeled.

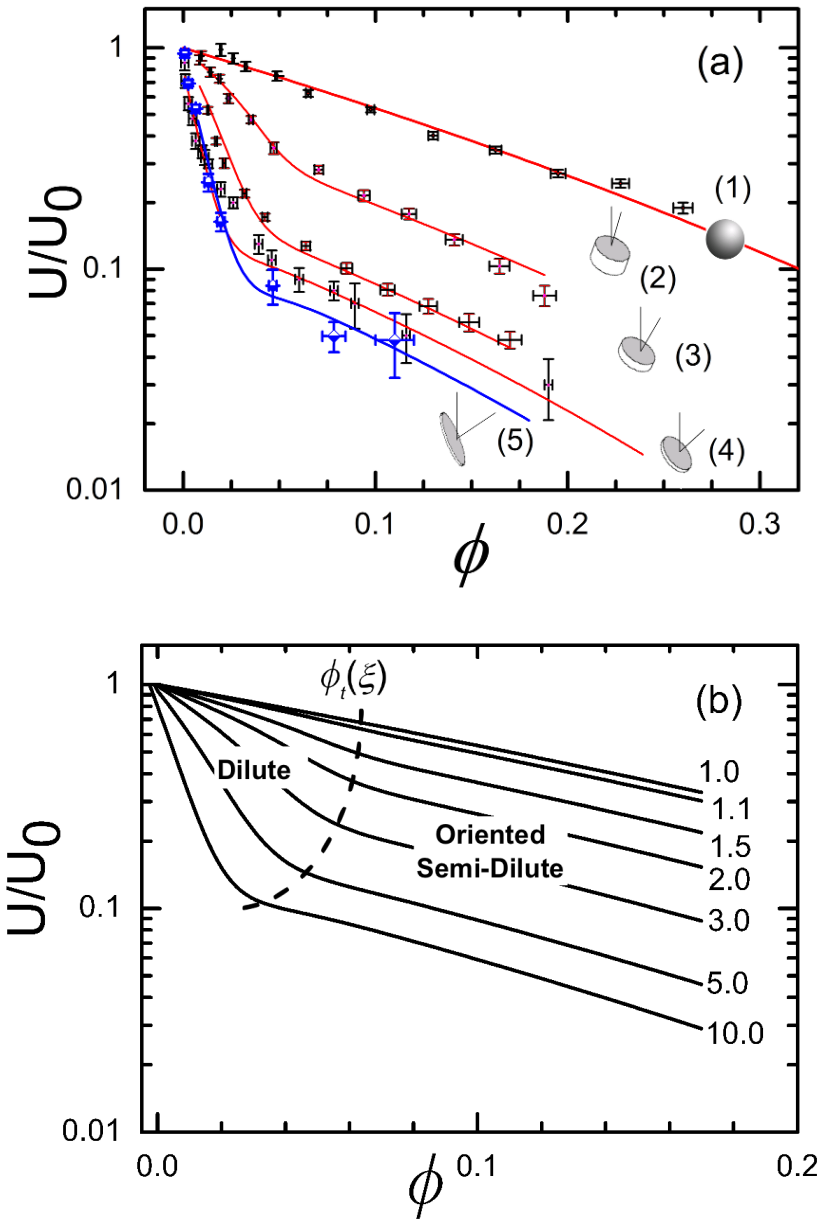

Figure 47 The dimensionless sedimentation/creaming speed as a function of particle volume fraction. For suspensions of spherical wax droplets (ξ = 1 for curve 1), ZrP platelets ($\xi \approx 9$ for curve 4 and $\xi \approx 130$ for curve 5), and wax disks ($\xi \approx 2.73$ for curve 2 and $\xi \approx 4.76$ for curve 3). (a) Experimental data. The disk orientations are illustrated according to the results in the inset of **Figure 48b**. (b) Hindrance function curves of equation (1) exhibit the influence of anisotropy. The numbers to the right of each solid curve represent the aspect ratios. A semi-concentrated region and the dilute region are separated by the dash line of $\phi_t(\xi)$.

At low volume fractions, U/U_0 displays a dramatic drop with increasing ϕ. For batch sedimentation or creaming, a solvent flux, which is called backflow, flows opposite to the sedimentation or creaming direction to compensate the volume flux of settling or creaming colloidal particles. The hydrodynamic interaction between this backflow and the moving particles will exert a force on the particles to retard their sedimentation/creaming speed, hence result in the drop of U/U_0 with increasing ϕ. A set of sphere data is given as reference (**Figure 47a**, line 1), which is directly measured using the spherical droplets in our wax emulsions (made by melting wax suspensions above 26 ℃) whose polydispersity is (13.73 ± 3.03) %, determined by DLS. The ratio U/U_0 in the sphere data is scaled as $(1 - \phi)^K$ to find the index K_{Sphere} = 5.95 ± 0.27, slightly below the theoretical value 6.5 of monodisperse spheres. For disks, the U/U_0 curves are approximately linear in this dilute region, but the slopes are much larger than that of spheres, suggesting a stronger backflow for disks sedimentation/creaming as the disks could occupy additional exclude volume comparing with spheres [100]. Our experiments also show that such slopes increase with increasing disk aspect ratio (**Figure 48a**), implying that disk shape can significantly alter their backflow. The slopes increase towards a limit value at large aspect ratio, as shown in **Figure 47a**, where the slope of ξ = 9 is very close to that of ξ = 130.

At higher volume fractions, the dramatic drop in U/U_0 with increasing ϕ abates in contrast to the dilute regime. All disk sedimentation/creaming curves are approximately parallel to one another, and their slopes are closer to sphere speed data. This is the first experimental observation that a weaker retardation of sedimentation/creaming speed occurs in disk suspensions at high volume fractions. We hypothesize that this reduction originates from the restricted orientation of the disks at high volume fractions, in agreement with the evidences in previous experimental observations of disk shear flow and sedimentation [156, 170]. Such restricted orientation could reduce the additional exclude volume of the disk particles, and alter the effect of backflow. The aspect ratio

dependence in the high volume fraction regime has the same trend as in the dilute regime, the larger the aspect ratio the smaller the normalized sedimentation/creaming speed. The differences between curves of various aspect ratios diminish at high aspect ratios. The curves move towards a limiting curve as the aspect ratio becomes very large (**Figure 47**).

Considering both trends in low and high volume fraction regimes, the following hindrance function for disk sedimentation/creaming is obtained,

$$\frac{U}{U_0} = 1 - W \quad 1 - \phi^{K_S} + W\,[1 - \phi + \phi_m\,]^{K_{sphere}} \tag{4.10}$$

$$W = [1 + \exp(-\frac{\phi - \phi_t}{\kappa})]^{-1} \tag{4.11}$$

In equation (4.10), the first term on right side is chosen to be consistent with the hindrance function of spherical particles by parameter K_S for dilute regime, and the second term on right side takes a similar form but emphasizes the effect of restricted orientation on the exclude volume through the parameter ϕ_m for the semi-dilute regime. Equation (4.11) is similar with a logistic function to describe the transition between dilute and semi-dilute regime above which the restricted orientation of disk particles emerges. The position of the transition is controlled by ϕ_t and the sharpness of the transition is controlled by κ. We used K_{Sphere} = 5.95 $\pm$ 0.27 (**Figure 49a**, line 1) from the measurement of our wax emulsions as mentioned above. The other parameters, K_S, ϕ_m, ϕ_t and κ, are obtained from fitting equation (4.10, 4.11) with experimental data and reveal the dependence of the hindrance function on the aspect ratio ξ. The values of the fitting parameters do not change significantly when ξ > 10, as shown in the insets of **Figure 49a** and **Figure 49b**.

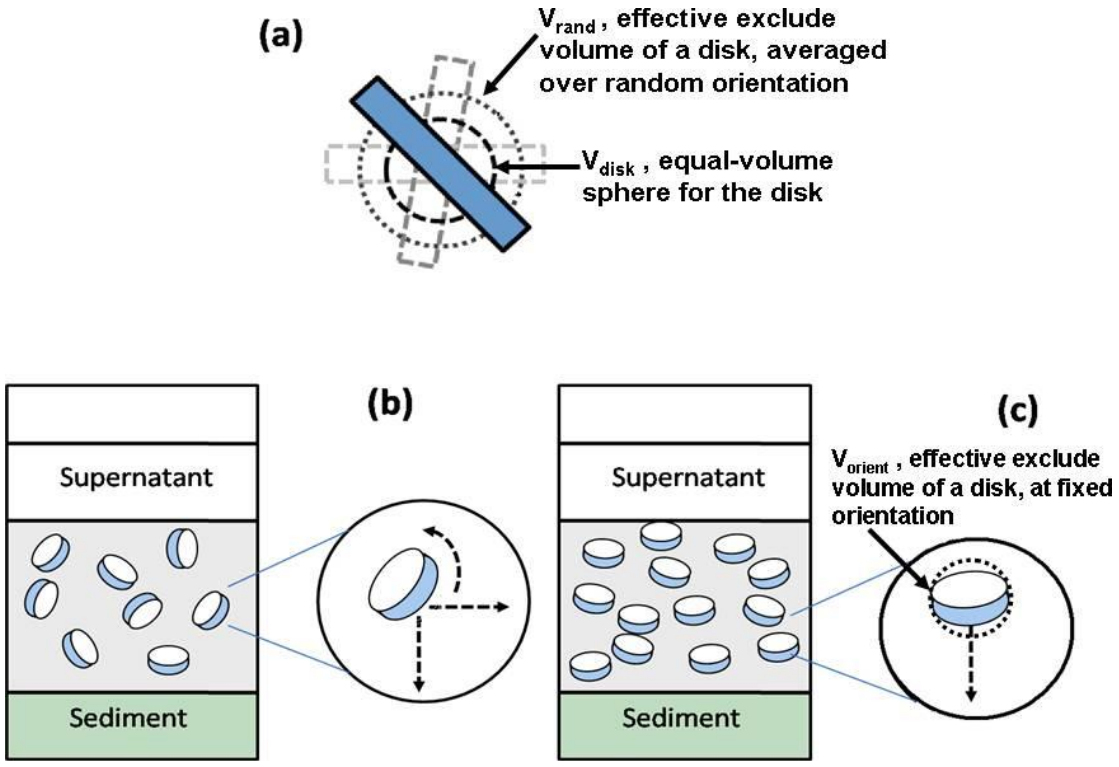

Figure 48 Orientation and motions of settling/creaming disk-shaped particles. (a) Representation of different "volumes" related to settling disks. (b) At low volume fractions, the disk-shaped particles are randomly oriented. The effective exclude volume, V_{rand}, is larger than the disk volume, V_{disk}. Hence, a higher resistance to the sedimentation/creaming speed is resulted from a stronger backflow comparing to the equal-volume spherical suspensions. (c) At high volume fractions, the disk-shaped particles tend to orient under the external force. Since $V_{disk} < V_{orient} < V_{rand}$, sedimentation/creaming speeds deviate from dilute suspensions but closes to the behavior of spheres.

At low volume fractions, the disk-shaped particles are randomly oriented due to Brownian motion. Hence, compared to spheres, disks will occupy a larger projection area than the equal-volume spheres in the plane perpendicular to the external force, thus interact more strongly with the solvent. The effective spherical volume V_{rand} for such sedimentation/creaming disk must include both the volume of the disk itself, V_{disk}, and the additional exclude volume consisting of bounded fluid carried with the particles

(**Figure 48b**). The larger exclude volume V_{rand} will require more compensation flux for balance, thus a larger backflow will be induced and the disk sedimentation/creaming is expected to be dramatically slower than that of rigid spherical particle suspensions.

The theoretical calculation of the backflow effect has not been performed for disk particles so far. Here, we attempt to estimate it using the effective spherical volume V_{rand} and a pair-correlation function g_{rand}. In our experiments, the Reynolds number Re = $\rho UD/\eta$ is very small, around 10^{-7}, and the Péclet number Pe = $\Delta mgd/k_BT$ is moderate, around 1-10. For sphere sedimentation at small Reynolds number, the index K_S can be derived from the creeping flow and the Oseen equations as [171]

$$K_S = \frac{1}{2} - 3\int_{z\geq 1} z\left[g\ z\ -1\right]\mathrm{d}z - \int_0^{\infty} z^2 g\ z\ \left[A\ z\ +2B\ z\ +C\ z\ \right]\mathrm{d}z \qquad (4.12)$$

In equation (4.12), the derivation considers only two-body hydrodynamic interactions. In the approximation of a linear dependence on ϕ, the contribution of backflow to the coefficient K_S will be 1, which is combined into the first two terms on right hand side. The last term in equation (4.12) accounts for the hydrodynamic reflection of its own backflow from all surrounding neighbor particles. In equation (4.12), $z = l/r$ is the ratio of the center-to-center distance l between a pair of spheres and the sphere radius r. $A(z)$,$B(z)$,$C(z)$ are the hydrodynamic mobility functions given by

$$A(z) = -\frac{15}{4}z^{-4} + \frac{11}{2}z^{-6} + O\ z^{-8} \qquad (4.13)$$

$$B(z) = -\frac{17}{16}z^{-6} + O\ z^{-8} \qquad (4.14)$$

$$C(z) = \frac{75}{4}z^{-6} + O\ z^{-9} \qquad (4.15)$$

and $g(z)$ is the pair-correlation function of the hard sphere potential,

$$g(z) = \begin{cases} 0, & z < 2 \\ 1, & z \geq 2 \end{cases} \tag{4.16}$$

Since $V_{rand} > V_{disk}$, the exclude distance $2R_{rand}$ will be larger than that of the equal-volume sphere suspensions, denoted as $2r_{eq}$. Due to the equal-volume relationship $\frac{4}{3}\pi r_{eq}^3 = \pi R_{rand}^2 t = 2\pi R_{rand}^3/\xi$, we have $R_{rand}/r_{eq} \sim O(\xi^{1/3})$. Substituting this into the pair-correlation function equation (4.16), we obtain the modified pair-correlation function to describe disks,

$$g_{rand}(z_{eq}) = \begin{cases} 0, & z_{eq} < 2\xi^{1/3} \\ 1, & z_{eq} \geq 2\xi^{1/3} \end{cases} \tag{4.17}$$

where z_{eq} is the ratio between center-to-center distance l and r_{eq}, instead of r. With the substitution of equation (2.16) by equation (4.17), the z in the integrals of equation (4.12) will be modified by a factor of $q = \sqrt[3]{2\xi/3}$. The numerical value 1/2 in equation (4.12) also requires an update to 1/3.

$$\begin{aligned} K_S(\xi) = {} & \frac{1}{3}\xi^{1/3} - 3\int_{z_{eq}\geq 1} qz_{eq}\left[g(z_{eq}) - 1\right]dz_{eq} \\ & - \int_0^{\infty} (qz_{eq})^2 g(z_{eq})\left[A(qz_{eq}) + 2B(qz_{eq}) + C(qz_{eq})\right]dz_{eq} \end{aligned} \tag{4.18}$$

This is equivalent to the substitution of V_{disk} by V_{rand}, thus we expect an amplification of K_{Sphere} by K_S due to the larger exclude volume for the disk sedimentation/creaming. Our experiments indeed indicate a linear dependence of K_S on ξ for $\xi < 10$, $K_S = (5.95 \pm 0.27) + (7.614 \pm 0.255) \cdot (\xi - 1)$, which can be roughly predicted by the first integral term in equation (4.18). Using equation (4.18), we obtain $K_S \approx 45$ for $\xi = 9$, in comparison to the experimental value $K_S \approx 68 \pm 12$ (**Figure 49a**). Several aspects might contribute to the discrepancy, including the polydispersity of the sample (increasing K_S

by 10% to 20%), different pair-correlations accounting for the anisotropy of disks [172], or the hydrodynamic mobility functions to be suitable for discotic colloids [21].

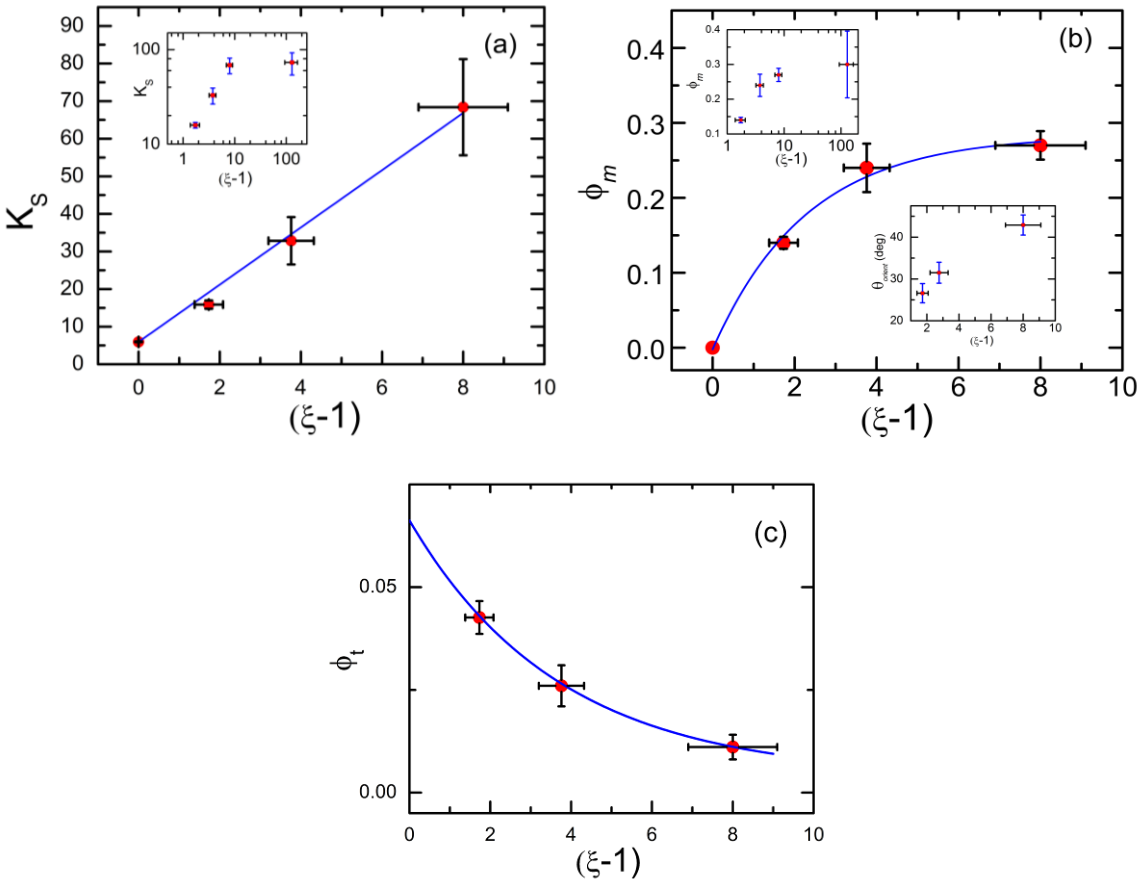

Figure 49. The dependence of hindrance function on the aspect ratio of disks. (a) K_S describes the backflow effect at dilute concentrations of disks as does in equation (2). (Inset) The limiting value of K_S with very high aspect ratio $\xi \sim 130$. (b) ϕ_m denotes the extra exclude volume for oriented disks compared to spheres. (Inset up) The limiting value of ϕ_m with very high aspect ratio $\xi \sim 130$. (Inset down) Disk orientation angle converted from the correlation of equation (2.19, 2.20) between ϕ_m and (V_{orient} / V_{disk}). (c) ϕ_t is the transition volume fraction above which disks orient.

Different from the dilute regime, previous experiments revealed that disk-shaped particles tend to align themselves with external flow at high volume fractions [21], and have a restricted orientation. In equation (4.11), the parameter ϕ_m accounts for the extra exclude volume for the oriented disks comparing to the equal-volume spheres, and our experiment indicates its dependence on ξ for $\xi < 10$, $\phi_m = (0.284 \pm 0.021)[1 - \exp(\frac{1-\xi}{2.29\pm0.487})]$. With a similar meaning, we define the projection volume of oriented disks perpendicular to the external force as V_{orient}. For a rigid sphere and an oriented disk with equal volume, the ratio between their cross section areas in the plane perpendicular to the external force varies with this orientation angle θ,

$$4\pi r^3/3 = \pi R^2 t = 2\pi R^3/\xi \qquad \Rightarrow \qquad r = \sqrt[3]{\frac{3}{4}R^2 t}\ , \tag{4.19}$$

$$\frac{A_{orient}}{A_{disk}} = \frac{\pi R^2}{\pi R\sqrt[3]{\frac{9}{16}Rt^2}} \cdot \cos\theta \approx 0.763\xi^{2/3} \cdot \cos\theta,\ \theta \in [0, \pi/2]\ . \tag{4.20}$$

Converting this ratio from cross section area to exclude volumes by assuming spherical shapes, we obtain $(V_{orient}/V_{disk}) \sim (A_{orient}/A_{disk})^{3/2} \sim 0.67\xi(\cos\theta)^{3/2}$. The oriented disk has a smaller effective exclude volume than random-oriented disks, i.e. $V_{disk} < V_{orient} < V_{rand}$, hence the compensation flux of backflow is smaller and the U/U_0 normalization is higher compared to random oriented disks, which is reflected as the weaker retardation of sedimentation/creaming speed occurring in disk suspensions at high volume fractions (**Figure 47a**).

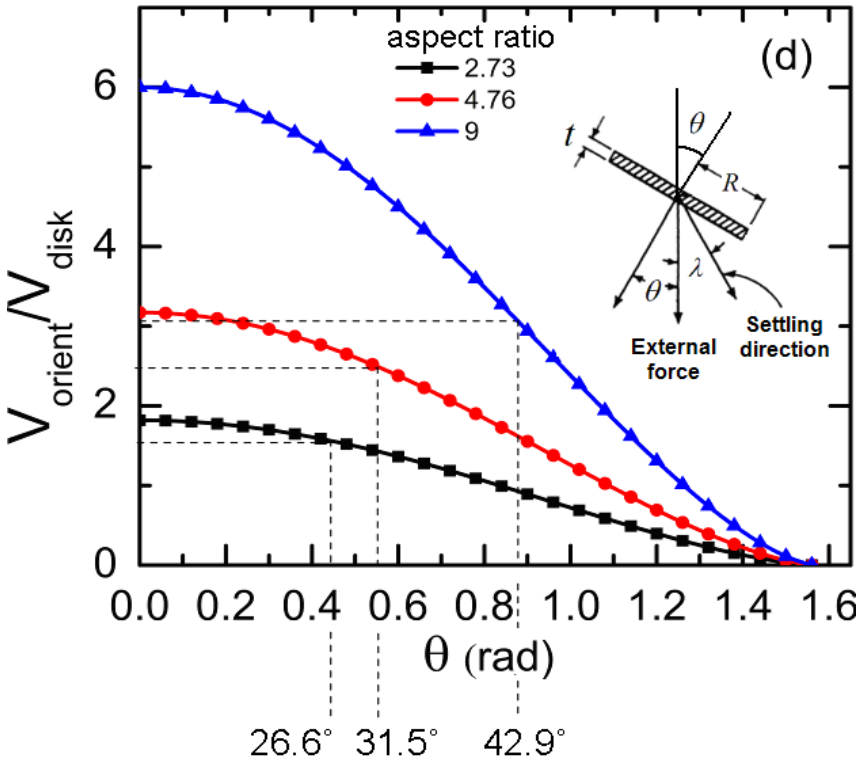

Figure 50 Angular dependence of (V_{orient} / V_{disk}) on the disk orientation angle θ . (Inset) Scheme of oblique falling of a disk.

Plotting V_{orient}/V_{disk} in **Figure 50**, we can see that as the aspect ratio of the disks increases, the change in this volume ratio becomes more remarkable with orientation angle. The volume fraction range of oriented disk sedimentation/creaming is approximately [0.05, 0.3], with a normalized speed U/U_0 corresponding to the sphere sedimentation/creaming in a volume fraction range [0.3, 0.5] (**Figure 47a**). Selecting the middle point in this range as a typical value, we obtain a correlation, $V_{orient} / V_{disk} \sim 0.4/(0.4 - \phi_m)$, which compares the gained exclude volume in the oriented disks, V_{orient}, with the equal-volume spheres, V_{disk}. The orientation angles θ_{orient} can then be estimated from the V_{orient} / V_{disk} function (**Figure 50**) and are plotted in the inset of **Figure 48b**. We

observe that the orientation angles θ_{orient} increase with the disk aspect ratio. This suggests that the small aspect ratio disks tends to settle/cream with their surfaces more or less perpendicular to the migration direction, while the disks with larger aspect ratio will be more willing to orient themselves with the surrounding flow field. Our normalized settling speed plot also shows that, for particles with the same aspect ratio, above the dilute to semi-dilute transition the slope of the U/U_0 curve does not change with increasing volume fractions, which indicates that the alignment and the orientation angle do not depend on volume fractions, similar with the results in clay suspension shearing experiments [156].

In our hindrance function equation (4.11), the trends in the dilute regime and semi-dilute regimes are connected at the transition point ϕ_t. All curves show a dramatic retardation in the dilute regime for random oriented disks, and moderate reductions in the semi-dilute regime for oriented disks. ϕ_t depends on the disk aspect ratio ξ for $\xi < 10$ as $\phi_t(\xi) = 0.062 - 0.0123(\xi - 1) + 7.4571 \times 10^{-4}(\xi - 1)^2$. It becomes smaller as the disk aspect ratio increases, which means the disks of higher aspect ratio are more willing to possess an orientation in settling compared to the disks having a smaller aspect ratio. Therefore, the orientation effect will manifest itself at lower volume fractions for high aspect ratio disks. This dependence on aspect ratio is also consistent with the prediction of clay suspensions under shearing flow [156], which explained that the transition volume fraction is an inverse function of the aspect ratio of particle when the Debye length is much smaller than the dimension of the particle:

$$\phi^* = 0.64\left(\frac{3}{2}\right)\left(\frac{h}{D}\right)\left[\frac{1}{1+2/D\kappa}^3\right] \tag{4.21}$$

where ϕ^* is the critical volume fraction for volume exclude interactions to occur, h and D are respectively the thickness and the diameter of particle, and κ^{-1} is the Debye length.

At low aspect ratios, the disks align nearly perpendicular to the external field, in contrast to a large tilt angle at high aspect ratio (Inset in **Figure 49b**). Hence, a small deviation in aspect ratio from that of a rigid sphere ($\xi = 1$) will greatly change the magnitude of the sedimentation/creaming speed curve (e.g. the curves for $\xi = 1.5$ and $\xi = 2$). It is important to further investigate this region in order to reveal the onset of the anisotropic effect for disks and oblate spheroids. There, the stability and hydrodynamic interactions will be significantly altered. Due to the difficulties of synthesizing disks in our experiments, it is hard to assess the deviation at small aspect ratio with $\xi < 2$, but numerical simulations might reveal more interesting aspects and behaviors in this region.

If the concentration of the disk colloidal suspensions goes higher above the semi-dilute region, under the heavy centrifugation field the particles will be compressed in the dense layer at the end of the testing tube, where crystallization occurs indicated by a growing peak in the transmission profiles as indicated in **Figure 51**. Crystalline phase possesses better optical properties, and the ordered-structure is more transparent to incident light than the random suspensions, which is the reason that a region of higher transmission is observed at the top of sediment.

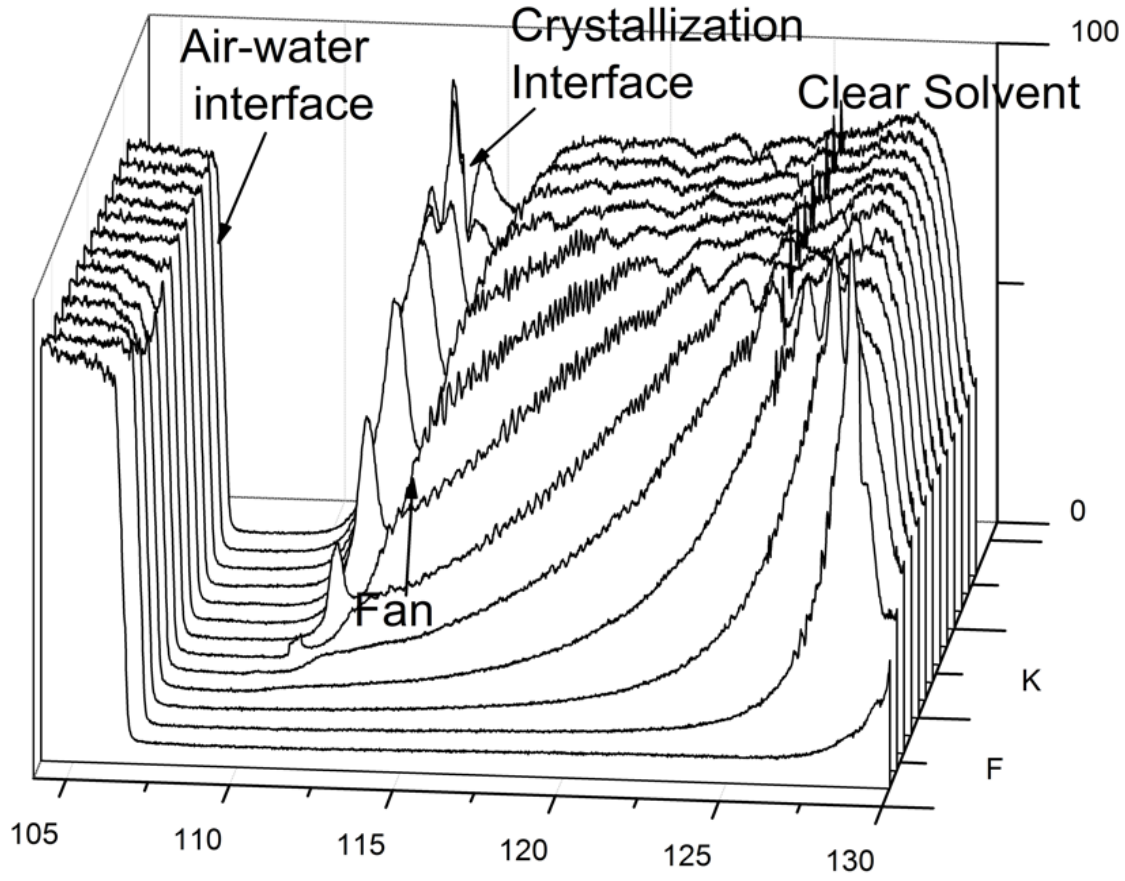

Figure 51 Emerging interfaces indicating new liquid crystalline phase growth in discotic colloidal suspensions.

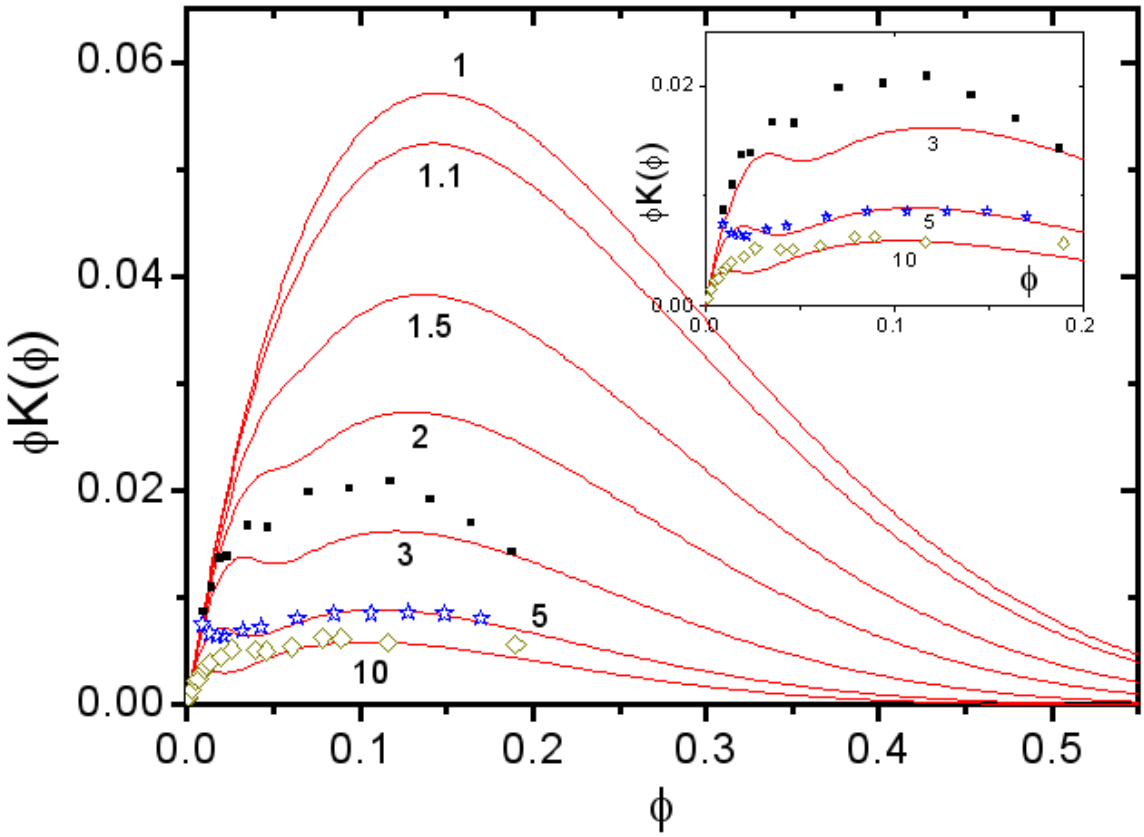

Figure 52 Non-monotonic change of settling flux curve in discotic colloidal suspensions.

The mass flux curves, which characterizes the rate of crystallization, are also calculate using both the experimental data as well as the hindrance function prediction, under various concentration and disk aspect ratio, as shown in **Figure 52**. The symbols labeled on the plot is calculated using experimental data as $\phi K(\phi) = \phi \frac{U(\phi)}{U_0}$, where $U(\phi)$ is the settling velocity at volume fraction ϕ, and U_0 is the Stokes velocity. The black dots, blue stars, and green diamonds correspond to aspect ratio 2.73, 4.76, and 9 respectively. The curves in **Figure 52** are calculated by using "$K(\phi)$ = equation (4.10)" (the hindrance function) at different aspect ratio of disk particles as labeled near the curves. It shows that the experimental data and the calculation from the hindrance functions generally

overlap with each other, and they both demonstrate a unique “2-step” shape with the increasing volume fraction instead of a smooth curve as in the spherical particle settling. The “step” in the flux curves is related to the transition of settling between dilute and semi-dilute region, therefore it has similar behavior as the hindered settling, more significant at higher aspect ratio, and happens at lower volume fraction at higher aspect ratio. This feature is unique to anisotropic particle suspension, hence is interesting to further investigations.

4.6. Conclusion

In summary, we propose a general hindrance function to describe sedimentation or creaming over the whole volume fraction regime of discotic fluid phase. This hindrance function includes the strong backflow in dilute suspensions due to the random orientation under Brownian motion, and the reduction of backflow effect at high volume fractions due to the restricted orientation. Our experiments indicate that the aspect ratio of discotic colloids plays an important role in their sedimentation/creaming behavior. For disk suspensions, the effective exclude volume, the restricted orientation, and the transition between dilute and semi-dilute regime are all sensitive to their aspect ratios. Especially, with a small deviation from the spherical shape, the disks will behave dramatically different. As a systematic investigation, this hindrance function will serve as a guide to better understand the stability and dynamics of discotic complex fluids commonly found in nature and industry.

5. SUMMARY

This thesis is to investigate the principle and proper controlling parameters in microfluidic emulsification, especially using electric field. Closely related to this is the dynamics of droplet formation. The latter is essential for the understanding of droplet formation theories, and also for the control of experiment to synthesize discotic colloids in this thesis.

The electric technique for controlling of droplet formation is explored by a detailed study on low-frequency AC Electro-Flow-Focusing (EFF) emulsification in microfluidic channels. This is the extension of previous work on DC Electro-Flow-Focusing, and we find: (1) the droplet size variation is not a monotonic function of the electric field as in the case of DC-EFF emulsification, which originates from the relaxation oscillation of the flow rate through the Taylor cone; and (2) a power-law droplet size distribution was obtained at the voltage ramping-up stage. A model in analog to the charge accumulation and release in an RC electric circuit with an adjustable resistor is set up to simulate the emulsification process, and the simulated data meet good agreement with the experiments and exhibit relaxation oscillation behavior. Using this model, it is found that the droplet size variation is mainly controlled by the strength of the electric field. Therefore, the relaxation oscillation phenomena will be better demonstrated using a linear ramping of the electric field such as a triangular waveform, instead of the sinusoidal waveform.

In the Section 2, in an attempt to understand the dynamics of drop formation in microfluidic channels, especially for the transition from periodic dripping to chaotic dripping observed in the experiments, numerical simulation is developed to use the VOF (volume of fraction) method to model the drop formation process. Using this technique, the simulation results help to interpret the transition in the theory of saddle-node transition in drop formation. It is found that the transition from a uniform droplet size to

a bimodal emulsification is due to the evolution of the water tips compared with a critical length, which governs the saddle-node bifurcation in the droplet formation process. The results show that the bimodal emulsification occurs when the water tip is greatly deformed and elongated such that, by just emitting a single drop, the tip length cannot return back to original value (which is smaller than critical length). By the bimodal emulsification, the water tip can meet the requirement of resetting the system to original conditions, therefore it is an intrinsic characteristics of a given microfluidic channel design. Further numerical investigation of various orifice design confirms the analysis, and provides the guideline that the design of the microfluidic flow-focusing channels needs cautious consideration such as for the orifice length. A small and short orifice would provide better performance to produce uniform droplet size in microfluidic emulsification, which is often desired in various applications like particle synthesis and micro-chemical-analysis systems.

As an application of the microfluidic emulsification, a method of fabricating disk-like wax colloidal particle suspensions using electrospray is reported. Various methods for the fabrication of disk-like colloidal particle using emulsification are also described, which meets the fundamental demands for the future experiments to prepare anisotropic particles. Based on this technique, the first measurement of the hindrance function is reported for sedimentation and creaming of disk-shaped colloids via the analytical centrifugation. Our results shows disk-like colloidal particles strongly align with the external flow right in the centrifugal fields above the volume fraction of a few percent and this effect is extremely sensitive to the aspect ratio of disks. For disk suspensions, the effective exclude volume, the restricted orientation, and the transition between dilute and semi-dilute regime are all sensitive to their aspect ratios. Especially, with a small deviation from the spherical shape, the disks will behave dramatically different. Due to this alignment effect, disk sedimentation/creaming demonstrate distinct trends in dilute and semi-dilute region. As a systematic investigation, this hindrance function will serve as a guide to better understand the stability and dynamics of discotic complex fluids commonly found in nature and industry, and also help to design and select better

techniques for separation and concentration of disk-like particles with a concern of their shape parameters.

REFERENCES

[1] D. J. Beebe, G. A. Mensing, and G. M. Walker, *Annu. Rev. Biomed. Eng.* **4**, 261 (2002).

[2] K. Chung *et al.*, *Nat. Methods* **8**, 171 (2011).

[3] K.-y. Chung, N. C. Mishra, C.-c. Wang, F.-h. Lin, and K.-h. Lin, *Biomicrofluidics* **3**, 022403 (2009).

[4] B. G. De Geest, J. P. Urbanski, T. Thorsen, J. Demeester, and S. C. De Smedt, *Langmuir* **21**, 10275 (2005).

[5] P. S. Dittrich, and A. Manz, *Nat. Rev. Drug Discovery* **5**, 210 (2006).

[6] E. Gerstner, *Nat. Phys.* **7**, 98 (2011).

[7] H. Kim *et al.*, *Appl. Phys. Lett.* **91**, 133106 (2007).

[8] H. Kim, T. L. Weiss, T. P. Devarenne, and A. Han, in *Proceedings of the 14th International Conference on Miniaturized Systems for Chemistry and Life*2010).

[9] J.-W. Kim, A. S. Utada, A. Fernández-Nieves, Z. Hu, and D. A. Weitz, *Angew. Chem., Int. Ed.* **46**, 1819 (2007).

[10] K. R. King, S. Wang, A. Jayaraman, M. L. Yarmush, and M. Toner, *Lab Chip* **8**, 107 (2008).

[11] P. Marmottant, and J.-P. Raven, *Soft Matter* **5**, 3385 (2009).

[12] Y. S. Song *et al.*, *Anal. Bioanal. Chem.* **395**, 185 (2009).

[13] H. A. Stone, A. D. Stroock, and A. Ajdari, *Annu. Rev. Fluid Mech.* **36**, 381 (2004).

[14] T. Thorsen, R. W. Roberts, F. H. Arnold, and S. R. Quake, *Phys. Rev. Lett.* **86**, 4163 (2001).

[15] G. M. Whitesides, *Nature* **442**, 368 (2006).

[16] C. N. Baroud, F. Gallaire, and R. Dangla, *Lab Chip* **10**, 2032 (2010).

[17] Z. Cheng *et al.*, in *Proceeding of the 4th International conference on computing, communications and control technologies, Orlando, FL*2006).

[18] J. Eggers, *Rev. Mod. Phys.* **69**, 865 (1997).

[19] A. M. Gañán-Calvo, C. Ferrera, M. Torregrosa, M. A. Herrada, and M. Marchand, *Microfluid Nanofluid* (2011).

[20] P. Garstecki, M. J. Fuerstman, H. A. Stone, and G. M. Whitesides, *Lab Chip* **6**, 437 (2006).

[21] J. Happel, and H. Brenner, *Low Reynolds number hydrodynamics: with special applications to particulate media* (Kluwer Academic, New York, 1991).

[22] H. A. Stone, *Annu. Rev. Fluid Mech.* **26**, 65 (1994).

[23] K. R. King *et al.*, *Lab Chip* **7**, 77 (2006).

[24] H. Yu, C. M. Alexander, and D. J. Beebe, *Lab Chip* **7**, 388 (2007).

[25] F. K. Balagaddé, L. You, C. L. Hansen, F. H. Arnold, and S. R. Quake, *Science* **309**, 137 (2005).

[26] E. Eriksson *et al.*, *Lab Chip* **7**, 71 (2006).

[27] E. Eriksson *et al.*, *J. Opt. A: Pure Appl. Opt.* **9**, S113 (2007).

[28] Y. C. Toh *et al.*, *Lab Chip* **7**, 302 (2007).

[29] Y. K. Cheung, B. M. Gillette, M. Zhong, S. Ramcharan, and S. K. Sia, *Lab Chip* **7**, 574 (2007).

[30] D. Di Carlo, L. Y. Wu, and L. P. Lee, *Lab Chip* **6**, 1445 (2006).

[31] H. H. Lee, J. Smoot, Z. McMurray, D. A. Stahl, and P. Yager, *Lab Chip* **6**, 1163 (2006).

[32] S. Cran-McGreehin, T. F. Krauss, and K. Dholakia, *Lab Chip* **6**, 1122 (2006).

[33] M. G. L. Van den Heuvel, M. P. De Graaff, and C. Dekker, *Science* **312**, 910 (2006).

[34] H. Lee, Y. Liu, D. Ham, and R. M. Westervelt, *Lab Chip* **7**, 331 (2007).

[35] Y. Huang, P. Castrataro, C. C. Lee, and S. R. Quake, *Lab Chip* **7**, 24 (2006).

[36] S. K. W. Dertinger, D. T. Chiu, N. L. Jeon, and G. M. Whitesides, *Anal. Chem.* **73**, 1240 (2001).

[37] K. Campbell, and A. Groisman, *Lab Chip* **7**, 264 (2006).

[38] X. Jiang *et al.*, *Anal. Chem.* **77**, 2338 (2005).

[39] S. K. Cho, and Y. Zhao, *Lab Chip* **7**, 490 (2007).

[40] M. Krishnan, N. Agrawal, M. A. Burns, and V. M. Ugaz, *Anal. Chem.* **76**, 6254 (2004).

[41] G. M. Whitesides, E. Ostuni, S. Takayama, X. Jiang, and D. E. Ingber, *Annu. Rev. Biomed. Eng.* **3**, 335 (2001).

[42] Y. Xia, and G. M. Whitesides, *Angew. Chem., Int. Ed.* **37**, 550 (1998).

[43] S. L. Anna, N. Bontoux, and H. A. Stone, *Appl. Phys. Lett.* **82**, 364 (2003).

[44] H. Song, D. L. Chen, and R. F. Ismagilov, *Angew. Chem., Int. Ed.* **45**, 7336 (2006).

[45] A. Utada *et al.*, *Science* **308**, 537 (2005).

[46] J. Shim *et al.*, *J. Am. Chem. Soc.* **129**, 8825 (2007).

[47] M. Joanicot, and A. Ajdari, *Science* **309**, 887 (2005).

[48] D. R. Link *et al.*, *Angew. Chem., Int. Ed.* **118**, 2618 (2006).

[49] P. Garstecki, M. J. Fuerstman, and G. M. Whitesides, *Phys. Rev. Lett.* **94** (2005).

[50] M. J. Jensen, H. A. Stone, and H. Bruus, *Phys. Fluid* **18**, 077103 (2006).

[51] M. Muradoglu, and H. A. Stone, *Phys. Fluid* **17**, 073305 (2005).

[52] A. Utada *et al.*, *MRS Bull.* **32**, 702 (2007).

[53] J. A. Gerbec, D. Magana, A. Washington, and G. F. Strouse, *J. Am. Chem. Soc.* **127**, 15791 (2005).

[54] J. D. Tice, H. Song, A. D. Lyon, and R. F. Ismagilov, *Langmuir* **19**, 9127 (2003).

[55] C. H. Chen, H. Lin, S. K. Lele, and J. G. Santiago, *J. Fluid Mech.* **524**, 263 (2005).

[56] W. J. Luo, K. F. Yarn, and S. P. Hsu, *Jap. J. Appl. Phys.* **46**, 1608 (2007).

[57] S. Okushima, T. Nisisako, T. Torii, and T. Higuchi, *Langmuir* **20**, 9905 (2004).

[58] J. Takagi, M. Yamada, M. Yasuda, and M. Seki, *Lab Chip* **5**, 778 (2005).

[59] M. Yamada, M. Nakashima, and M. Seki, *Anal. Chem.* **76**, 5465 (2004).

[60] D. Link, S. Anna, D. Weitz, and H. Stone, *Phys. Rev. Lett.* **92** (2004).

[61] B. S. Lee *et al.*, *J. Colloid Interface Sci.* **302**, 294 (2006).

[62] T. Ward, M. Faivre, M. Abkarian, and H. A. Stone, *Electrophoresis* **26**, 3716 (2005).

[63] I. Barbulovic-Nad, X. Xuan, J. S. H. Lee, and D. Li, *Lab Chip* **6**, 274 (2005).

[64] P. Umbanhowar, V. Prasad, and D. Weitz, *Langmuir* **16**, 347 (2000).

[65] L. Xu, S. Davies, A. B. Schofield, and D. A. Weitz, *Phys. Rev. Lett.* **101**, 94502 (2008).

[66] E. Quevedo, J. Steinbacher, and D. T. McQuade, *J. Am. Chem. Soc.* **127**, 10498 (2005).

[67] D. Dendukuri, D. C. Pregibon, J. Collins, T. A. Hatton, and P. S. Doyle, *Nat. Mater.* **5**, 365 (2006).

[68] W. B. Russel, W. Russel, D. A. Saville, and W. R. Schowalter, *Colloidal dispersions* (Cambridge University Press, Cambridge, 1992).

[69] A. Einstein, *Investigations on the Theory of the Brownian Movement* (Dover Publications, New York, 1905).

[70] J. H. Masliyah, S. Bhattacharjee, and J. Wiley, *Electrokinetic and colloid transport phenomena* (Wiley, New York, 2006).

[71] J. Perrin, *Rendus de lAcad émie des Sciences* **146**, 967 (1908).

[72] J. Perrin, *Brownian movement and molecular reality* (Taylor and Francis, New York, 1910).

[73] W. Hardy, *Proc. R. Soc. London* **66**, 110 (1899).

[74] G. Gouy, *J. Phys.* **9**, 457 (1910).

[75] D. L. Chapman, *Philos. Mag.* **25**, 475 (1913).

[76] M. Smoluchowski, *Bull. Intl Acad. Sci. Cracovie* **8**, 182 (1903).

[77] H. Hamaker, *Physica* **4**, 1058 (1937).

[78] B. Derjaguin, and L. Landau, *Acta Physicochim. URSS* **14**, 633 (1941).

[79] E. J. W. Verwey, and J. T. G. Overbeek, *Theory of the stability of lyophobic colloids* (Dover Publications, New York, 1999).

[80] R. Larson, (Oxford University Press, New York, 1999).

[81] F. Weber *et al.*, *Science* **140**, 1090 (1963).

[82] V. F. Puntes, D. Zanchet, C. K. Erdonmez, and A. P. Alivisatos, *J. Am. Chem. Soc.* **124**, 12874 (2002).

[83] W. U. Huynh, J. J. Dittmer, and A. P. Alivisatos, *Science* **295**, 2425 (2002).

[84] L. L. Munn, and M. M. Dupin, *Ann. Biomed. Eng.* **36**, 534 (2008).

[85] P. Mongondry, J. F. Tassin, and T. Nicolai, *J. Colloid Interface Sci.* **283**, 397 (2005).

[86] A. Mohraz, and M. J. Solomon, *J. Colloid Interface Sci.* **300**, 155 (2006).

[87] E. Belamie, P. Davidson, and M. Giraud-Guille, *J. Phys. Chem. B* **108**, 14991 (2004).

[88] S. Kim, and S. J. Karrila, *Microhydrodynamics* (Dover Publications, New York, 1991).

[89] M. E. Leunissen *et al.*, *Nature* **437**, 235 (2005).

[90] L. Onsager, *Ann. N. Y. Acad. Sci.* **51**, 627 (1949).

[91] J. Valverde, M. Quintanilla, and A. Castellanos, *Phys. Rev. Lett.* **92**, 258303 (2004).

[92] A. E. Nel *et al.*, *Nat. Mater.* **8**, 543 (2009).

[93] R. Cush, D. Dorman, and P. S. Russo, *Macromolecules* **37**, 9577 (2004).

[94] L. Hong, S. Jiang, and S. Granick, *Langmuir* **22**, 9495 (2006).

[95] C. M. van Kats, P. M. Johnson, J. E. A. M. van den Meerakker, and A. van Blaaderen, *Langmuir* **20**, 11201 (2004).

[96] G. M. Whitesides, and M. Boncheva, *Proc. Natl. Acad. Sci. U. S. A.* **99**, 4769 (2002).

[97] L. Rayleigh, *Nature* **44**, 249 (1891).

[98] M. A. Horsch, Z. Zhang, and S. C. Glotzer, *Nano Lett.* **6**, 2406 (2006).

[99] M. B. Sigman Jr *et al.*, *J. Am. Chem. Soc.* **125**, 16050 (2003).

[100] F. van der Kooij, A. Philipse, and J. Dhont, *Langmuir* **16**, 5317 (2000).

[101] F. M. van der Kooij, E. S. Boek, and A. P. Philipse, *J. Colloid Interface Sci.* **235**, 344 (2001).

[102] F. M. van der Kooij, K. Kassapidou, and H. N. W. Lekkerkerker, *Nature* **406**, 868 (2000).

[103] F. M. van der Kooij, and H. N. W. Lekkerkerker, *J. Phys. Chem. B* **102**, 7829 (1998).

[104] A. Brown, S. Clarke, and A. Rennie, *Langmuir* **14**, 3129 (1998).

[105] S. Badaire, C. Cottin-Bizonne, W. Joseph, A. Yang, and A. D. Stroock, *J. Am. Chem. Soc.* **129**, 40 (2007).

[106] Z. Cheng, P. Chaikin, and T. Mason, *Phys. Rev. Lett.* **89**, 108303 (2002).

[107] T. Mason, *Phys. Rev. E* **66**, 060402 (2002).

[108] Z. Cheng, and T. Mason, *Phys. Rev. Lett.* **90**, 18304 (2003).

[109] C. J. Hernandez, and T. G. Mason, *J. Phys. Chem. C* **111**, 4477 (2007).

[110] C. J. Hernandez, K. Zhao, and T. G. Mason, *Soft Mater.* **5**, 1 (2007).

[111] S. Chandrasekhar, B. Sadashiva, and K. Suresh, *Pramana* **9**, 471 (1977).

[112] H. Brenner, *J. Fluid Mech.* **11**, 604 (1961).

[113] H. Brenner, *J. Colloid Interface Sci.* **23**, 407 (1967).

[114] R. Cox, *J. Fluid Mech.* **23**, 625 (1965).

[115] A. S. Khair, and J. F. Brady, *J. Rheol.* **52**, 165 (2008).

[116] E. W. Merrill, *Physicol. Rev.* **49**, 863 (1969).

[117] S. Chien, *Annu. Rev. Physiol.* **49**, 177 (1987).

[118] M. Dao, C. Lim, and S. Suresh, *J. Mech. Phys. Solids* **51**, 2259 (2003).

[119] A. Drochon, *Eur. Phys. J. Appl. Phys.* **22**, 155 (2003).

[120] C. Lim, M. Dao, S. Suresh, C. Sow, and K. Chew, *Acta Mater.* **52**, 1837 (2004).

[121] J. Sleep, D. Wilson, R. Simmons, and W. Gratzer, *Biophys. J.* **77**, 3085 (1999).

[122] K. Svoboda, C. Schmidt, D. Branton, and S. Block, *Biophys. J.* **63**, 784 (1992).

[123] M. Abkarian, and A. Viallat, *Soft Matter* **4**, 653 (2008).

[124] J. Higgins, D. Eddington, S. Bhatia, and L. Mahadevan, *Proc. Natl. Acad. Sci. U. S. A.* **104**, 20496 (2007).

[125] R. D. Jaggi, R. Sandoz, and C. S. Effenhauser, *Microfluid Nanofluid* **3**, 47 (2007).

[126] P. Coullet, L. Mahadevan, and C. Riera, *Prog. Theor. Phys. Suppl.* **139**, 507 (2000).

[127] P. Coullet, L. Mahadevan, and C. S. Riera, *J. Fluid Mech.* **526**, 1 (2005).

[128] M. Hazewinkel, *Encyclopaedia of mathematics: Supplement* (Springer, Amsterdam, 2001).

[129] S. Hardt, *Phys. Fluid* **17**, 100601 (2005).

[130] J. Bławzdziewicz, V. Cristini, and M. Loewenberg, *Phys. Fluid* **14**, 2709 (2002).

[131] A. M. Gañán-Calvo, *Phys. Rev. Lett.* **80**, 285 (1998).

[132] R. T. Collins, J. J. Jones, M. T. Harris, and O. A. Basaran, *Nat. Phys.* **4**, 149 (2007).

[133] A. M. Gañán-Calvo, *Phys. Rev. Lett.* **98**, 134503 (2007).

[134] A. M. Gañán-Calvo, and J. M. Montanero, *Phys. Rev. E* **79**, 066305 (2009).

[135] H. Gu, F. Malloggi, S. A. Vanapalli, and F. Mugele, *Appl. Phys. Lett.* **93**, 183507 (2008).

[136] D. Lastochkin, and H. C. Chang, *J. Appl. Phys.* **97**, 123309 (2005).

[137] L. Y. Yeo, D. Lastochkin, S. C. Wang, and H. C. Chang, *Phys. Rev. Lett.* **92**, 133902 (2004).

[138] J. B. Fenn, M. Mann, C. K. Meng, S. F. Wong, and C. M. Whitehouse, *Science* **246**, 64 (1989).

[139] M. Cloupeau, and B. Prunet-Foch, *J. Aerosol Sci.* **25**, 1021 (1994).

[140] W. Zhang, *Phys. Rev. Lett.* **93** (2004).

[141] W. W. Zhang, and J. R. Lister, *Phys. Rev. Lett.* **83**, 1151 (1999).

[142] T. W. Oppel, W. K. Myers, and C. S. Keefer, *J. Clin. Invest.* **12**, 291 (1933).

[143] P. Cheng, and H. Schachman, *J. Polym. Sci.* **16**, 19 (1955).

[144] D. Lakehal, *Int. J. Multiphase Flow* **28**, 823 (2002).

[145] K. Davis, W. Russel, and W. Glantschnig, *J. Chem. Soc., Faraday Trans.* **87**, 411 (1991).

[146] P. Segre, E. Herbolzheimer, and P. Chaikin, *Phys. Rev. Lett.* **79**, 2574 (1997).

[147] G. G. Stokes, *On the effect of the internal friction of fluids on the motion of pendulums* (Pitt Press, Pittsburgh, 1851).

[148] S. C. Glotzer, and M. J. Solomon, *Nat. Mater.* **6**, 557 (2007).

[149] Z. Dogic, A. Philipse, S. Fraden, and J. Dhont, *J. Chem. Phys.* **113**, 8368 (2000).

[150] M. B. Mackaplow, and E. S. G. Shaqfeh, *J. Fluid Mech.* **376**, 149 (1998).

[151] B. Metzger, J. E. Butler, and E. Guazzelli, *J. Fluid Mech.* **575**, 307 (2007).

[152] R. H. Davis, *Phys. Fluid* **3**, 2051 (1991).

[153] V. Salokhe, and N. Quang, *J. Terramech.* **32**, 231 (1995).

[154] M. Gray, Z. Xu, and J. Masliyah, *Phys. Today* **62**, 31 (2009).

[155] O. W. Moe, *Lancet* **367**, 333 (2006).

[156] S. Jogun, and C. Zukoski, *J. Rheol.* **43**, 847 (1999).

[157] G. Batchelor, *J. Fluid Mech.* **52**, 245 (1972).

[158] S. Paulin, and B. J. Ackerson, *Phys. Rev. Lett.* **64**, 2663 (1990).

[159] J. Richardson, and W. Zaki, *Chem. Eng. Sci.* **3**, 65 (1954).

[160] R. Buscall, J. Goodwin, R. Ottewill, and T. F. Tadros, *J. Colloid Interface Sci.* **85**, 78 (1982).

[161] G. Batchelor, and C. S. Wen, *J. Fluid Mech.* **124**, 495 (1982).

[162] F. Capuani, I. Pagonabarraga, and D. Frenkel, *J. Chem. Phys.* **124**, 124903 (2006).

[163] A. F. Mejia, P. He, D. Luo, M. Marquez, and Z. Cheng, *J. Colloid Interface Sci.* **334**, 22 (2009).

[164] D. Sun, H. J. Sue, Z. Cheng, Y. Martínez-Ratón, and E. Velasco, *Phys. Rev. E* **80**, 041704 (2009).

[165] L. Sun, W. J. Boo, D. Sun, A. Clearfield, and H. J. Sue, *Chem. Mater.* **19**, 1749 (2007).

[166] H. Shimizu, *J. Chem. Phys.* **37**, 765 (1962).

[167] D. Fromer, and D. Lerche, *Arch. Appl. Mech.* **72**, 85 (2002).

[168] D. Lerche, *J. Dispersion Sci. Technol.* **23**, 699 (2002).

[169] T. Sobisch, and D. Lerche, *Colloid Polym. Sci.* **278**, 369 (2000).

[170] W. Whalley, and C. Mullins, *J. Soil Sci.* **43**, 531 (1992).

[171] J. K. G. Dhont, *An introduction to dynamics of colloids* (Elsevier Science, Amsterdam, 1996).

[172] D. Costa, J. P. Hansen, and L. Harnau, *EPL* **53**, 729 (2001).

APPENDIX A

FLUENT Simulation Setup

The details of the setup in FLUENT simulation are described in this appendix. The following description shows a step-by-step setup of a typical three-dimensional (3D) simulation case from scratch, whose calculation results demonstrate the bimodal droplet formation in flow-focusing geometry (see **Figure 23**). The software package used here is the ANSYS FLUENT 13.0.0 (commercial numerical package), Linux 64-bit version, single-precision, and the case is created for running on parallel environment using four CPU cores. The overview of the procedure is listed below:

Step 1: Start FLUENT.

Step 2: Load and process mesh.

Step 3: Set up VOF model.

Step 4: Set material properties.

Step 5: Set up phases and interface tension.

Step 6: Load user-defined function (UDF) and set user-defined scalar (UDS).

Step 7: Set up bulk fluid properties and source term.

Step 8: Set up boundary conditions.

Step 9: Set up solver.

Step 10: Set up convergence monitor.

Step 11: Initialization and patch.

Step 12: Set up the iteration parameters.

Step 1: Start FLUENT.

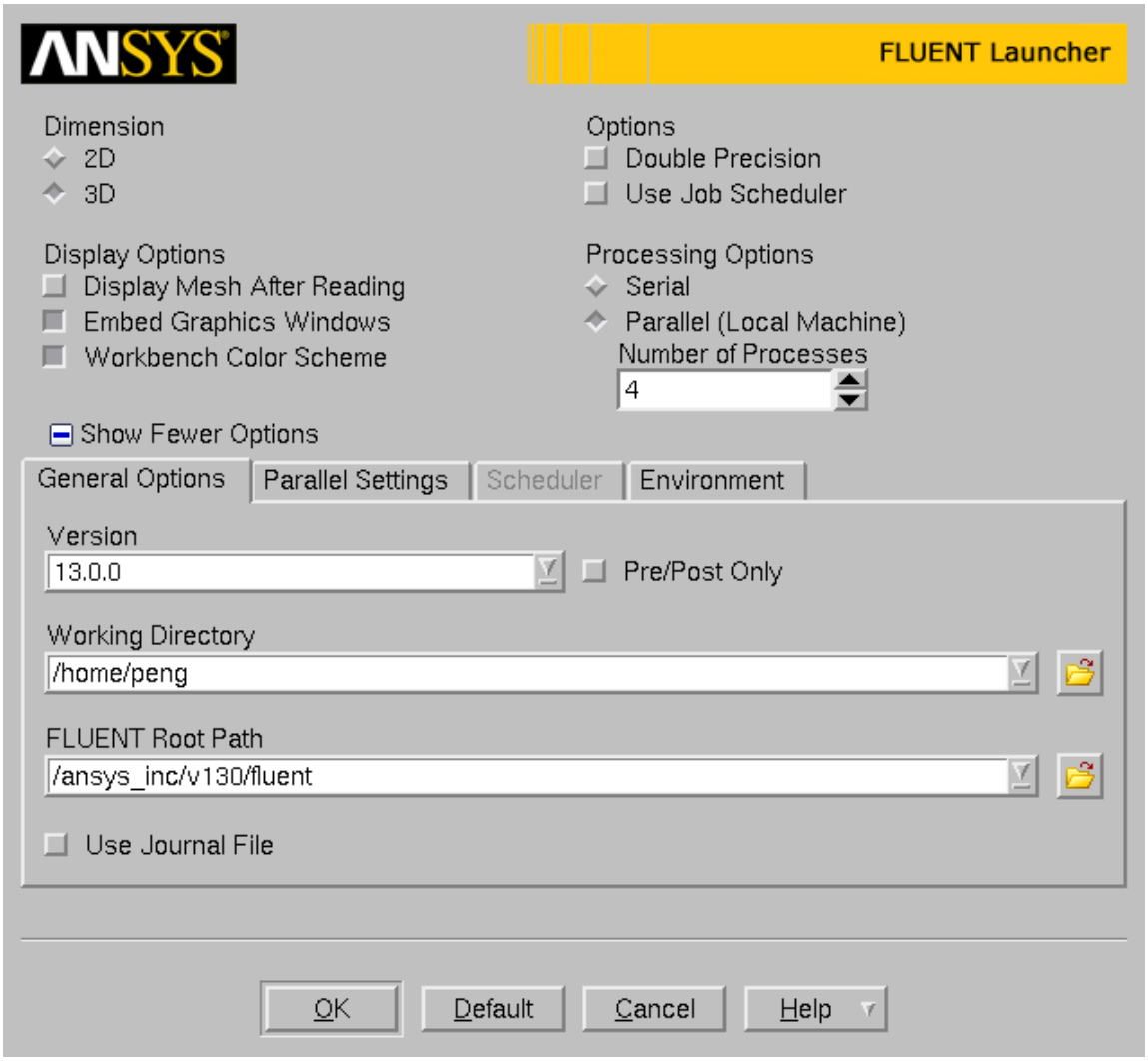

Figure A1 FLUENT launcher settings: General Options.

The simulator is started using the "FLUENT launcher" interface, in which the following options could be selected or altered: dimension information (2D or 3D), Single-/Double-precision switch, Serial/Parallel processing switch, (if parallel selected) number of processes (cores) to be used, and miscellaneous display options. In the

advanced option tabs, from the “General Options” tab (see **Figure A1**) the working directory could be set, and (if parallel selected) from the “Parallel Settings” tab the communication method between nodes and MPI type could be set. In this example, 3D, single-precision, parallel, 4 processes are selected, and other options are left to default values without change.

Step 2: Load and process mesh.

The mesh file generated by GAMBIT (see Appendix C) is loaded through menu: File -> Read -> Mesh (**Figure A2**), and the loaded mesh will be displayed as in **Figure A3**. In this example, the mesh created in GAMBIT is in the unit of meter by default, therefore it requires a conversion into the unit of micrometer by multiplying a scaling factor of 1e-6 (**Figure A4**) in the scaling dialog in “General” panel (**Figure A5**). As shown in **Figure A5**, besides the routines of “check mesh” and “report mesh quality”, it is crucial to run “reorder domain” at least once after import the mesh. The “reorder domain” will optimize the arrange and order of cells in the memory cache by reducing the bandwidth, which is the maximum difference between neighboring cells in the memory, so that the neighboring cells are close to each other in the memory and reduce the cost of memory access and disk swapping. This might enhance the calculation efficiency, especially in parallel use. In the end, the basic solver settings (**Figure A6**) are also adjust in the “General” panel: Pressure-based solver (default), Absolute velocity formulation (default), and Transient calculation.

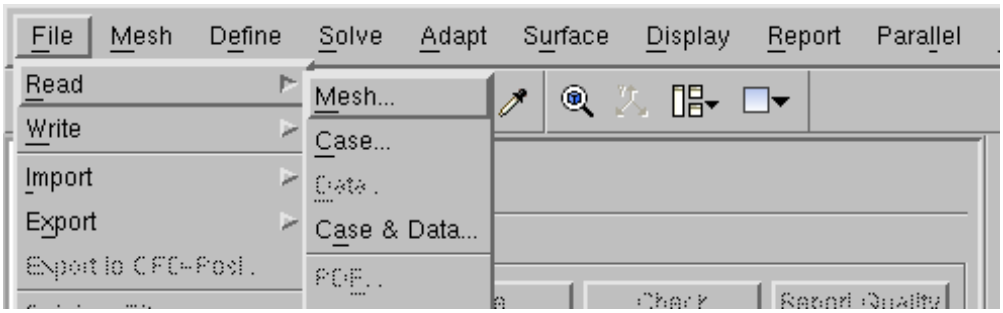

Figure A2 Load mesh files using menu: File -> Read -> Mesh…

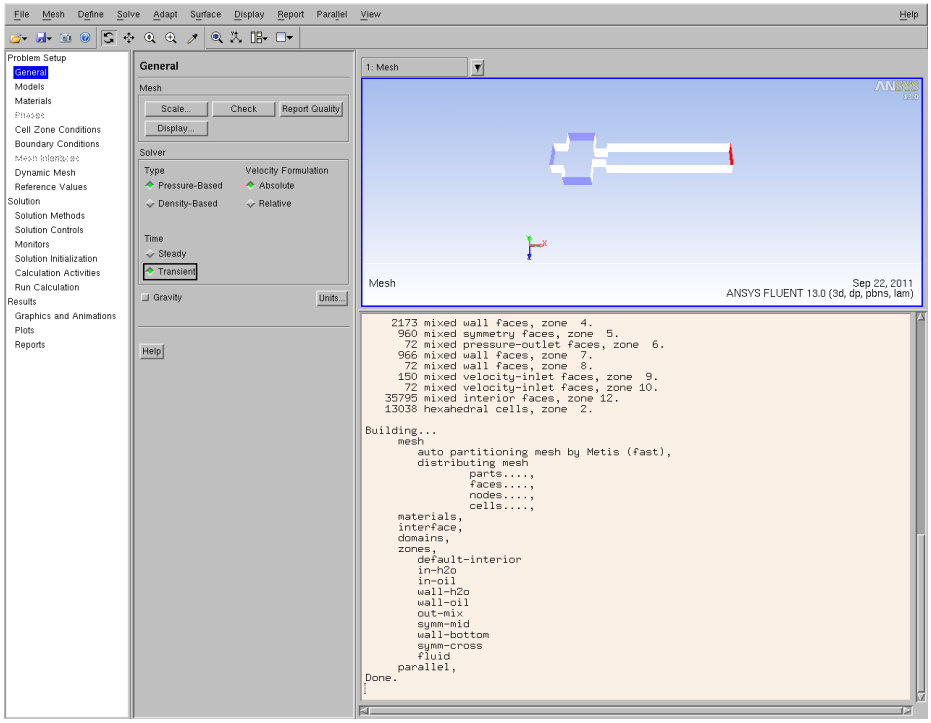

Figure A3 Display of loaded mesh in FLUENT.

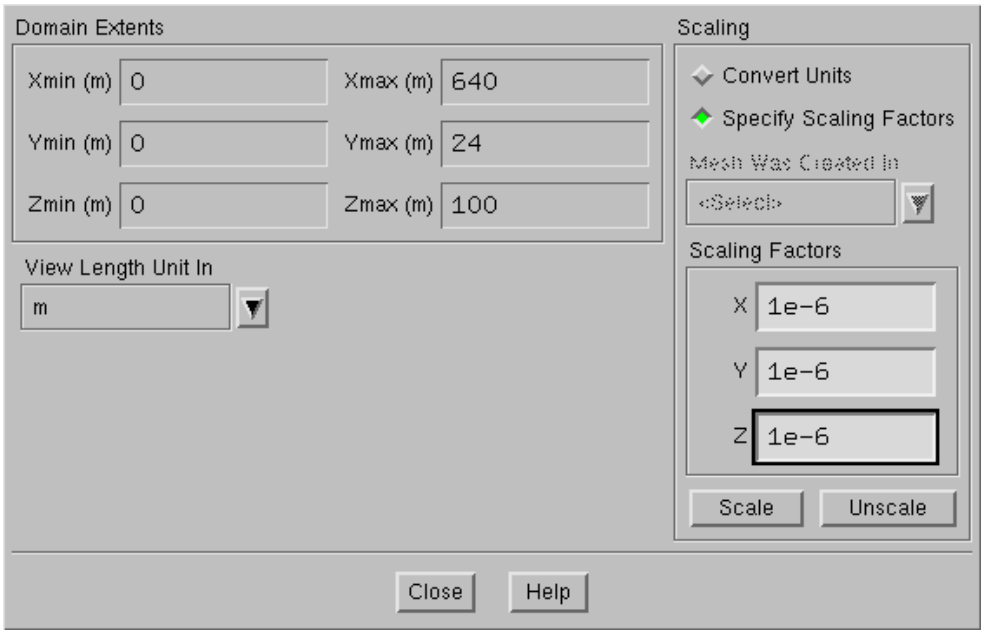

Figure A4 Scaling of imported mesh.

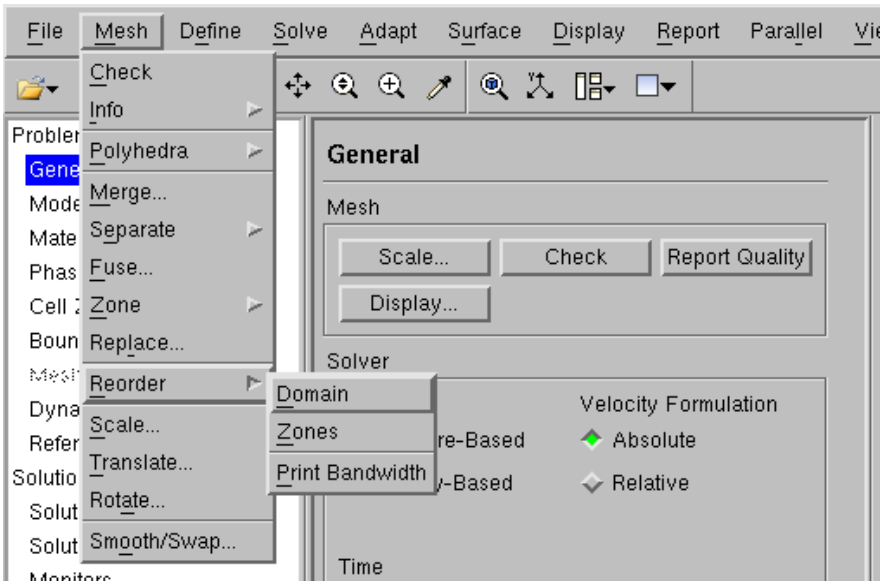

Figure A5 Reorder domain in the mesh.

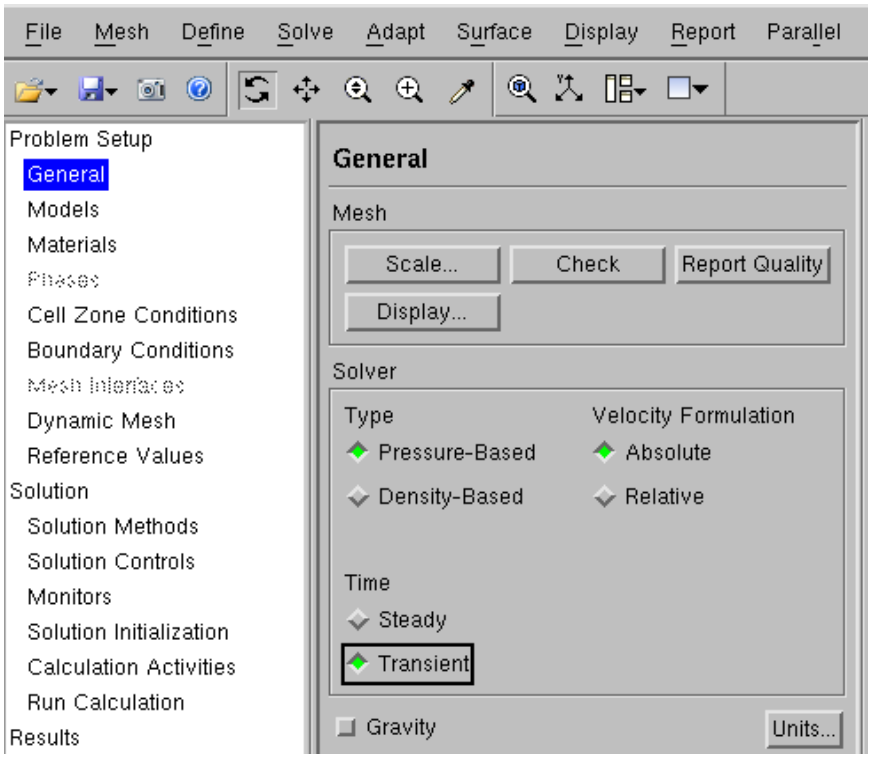

Figure A6 Basic solver settings in "General" panel.

Step 3: Set up VOF model.

In the next "Models" panel, various physics models are mostly turned off by defaults. In this example, the "Viscous" model will be left as "Laminar", and other models will be left in the "off" condition by default, except for "Multiphase" model, which will be set to Volume-of-Fluid (VOF) method (**Figure A7**). The details of the VOF model settings are shown in **Figure A8**. In this example, the default values are used for the calculation: explicit VOF scheme, cutoff value of volume fraction = 1e-6, and Courant number = 0.25. Other switches, such as implicit body force, level set coupling, and open channel flow, are all kept in "off" condition.

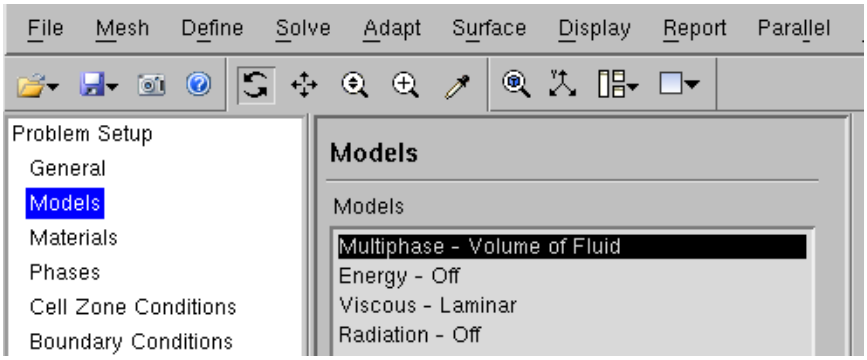

Figure A7 Multiphase settings in "Models" panel.

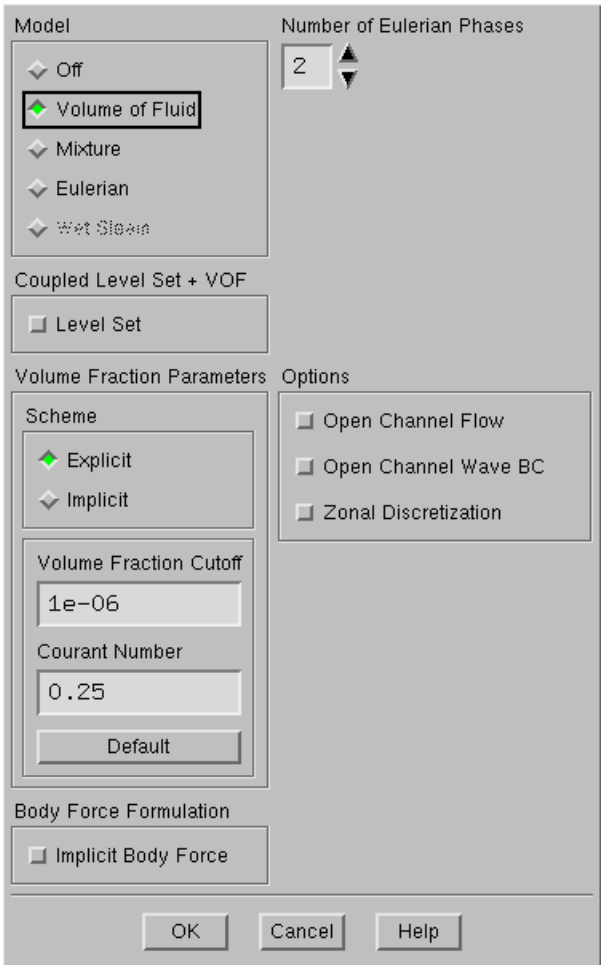

Figure A8 Details of VOF model settings.

Step 4: Set material properties.

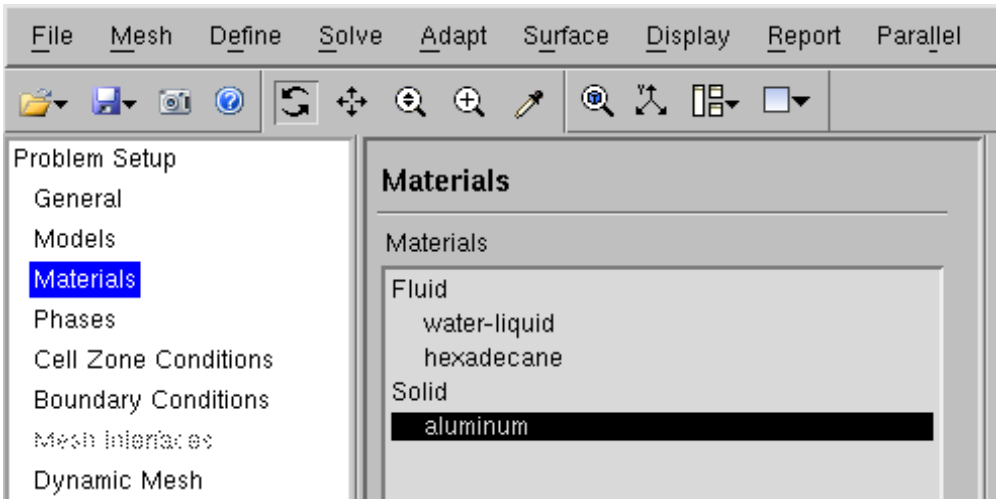

Figure A9 Set up material properties in the "Materials" panel.

The material properties are set up in the "Materials" panel (**Figure A9**). The properties of water is built in the database of FLUENT, therefore could be directly accessed through "create/change" -> "Fluent Database"-> "water-liquid" -> "copy" (**Figure A10**), which holds density of 998.2 kg/m^3 and viscosity of 0.001003 kg/m-s (**Table 4**). The default material properties of air does not apply to this example, hence it is overwritten by the properties of hexadecane (oil). Only density and viscosity are used in the simulation, and they are set to density of 773 kg/m3, and viscosity = 0.00334 kg/m-s (**Figure A11**).

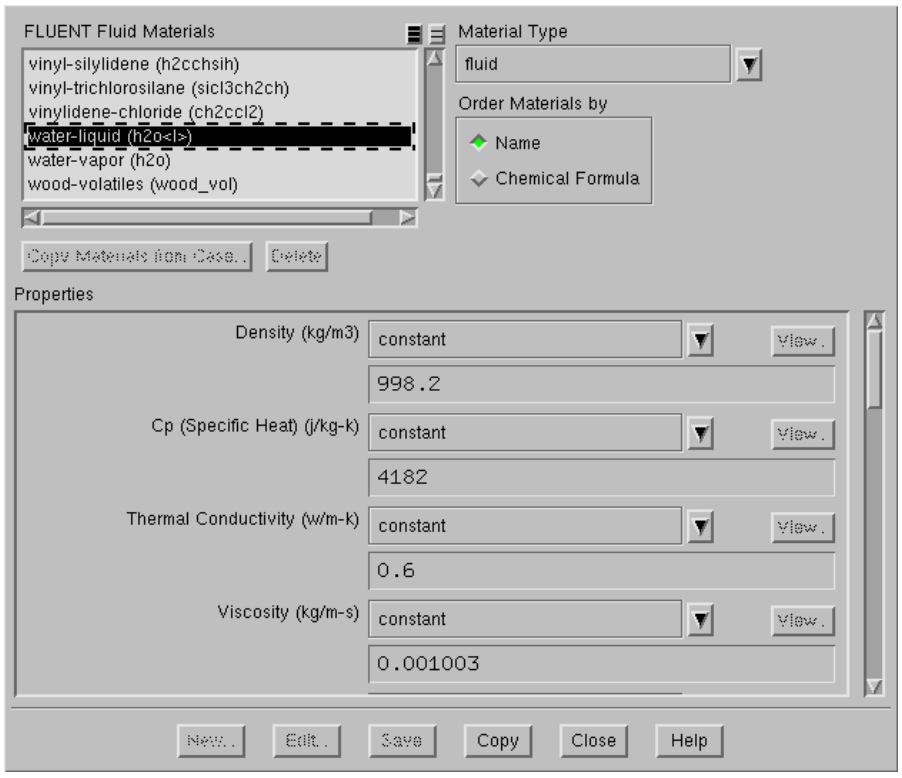

Figure A10 Set up of water properties.

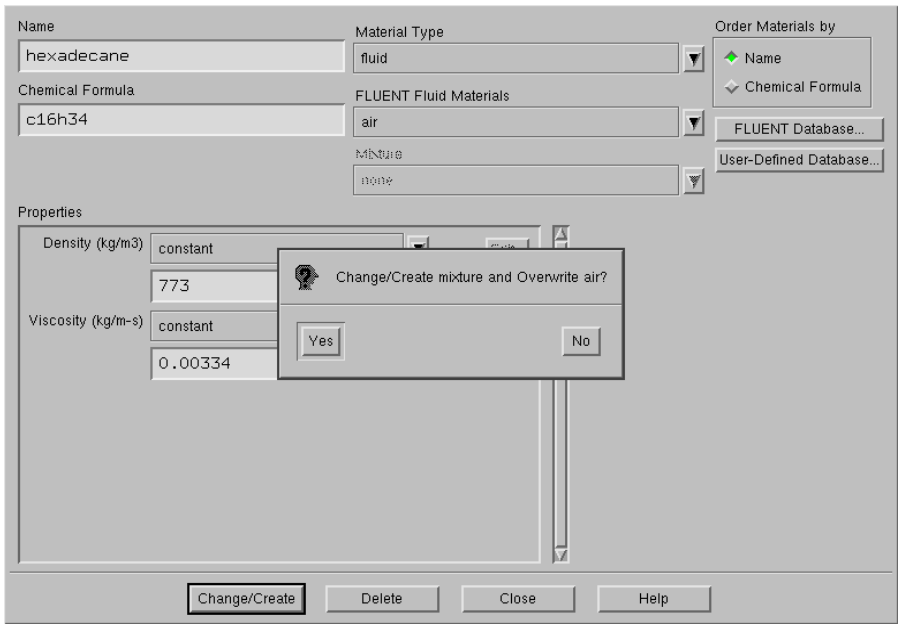

Figure A11 Set up of oil properties.

Step 5: Set up phases and interface tension.

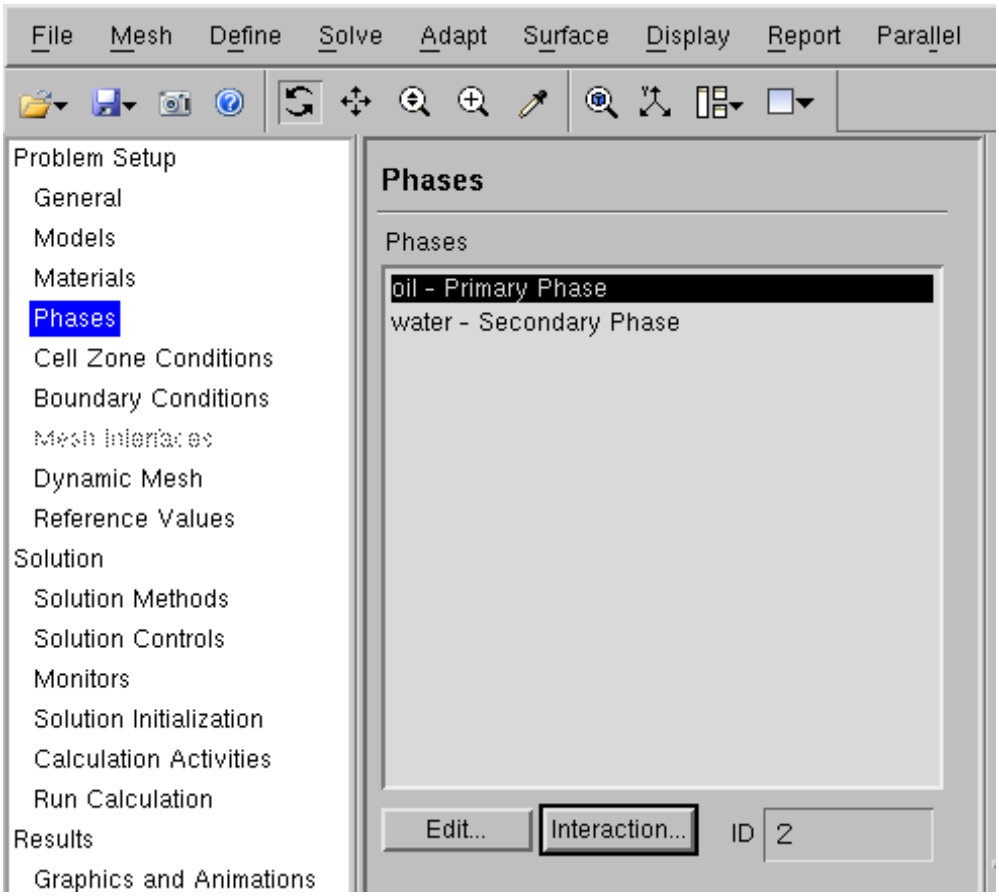

Figure A12 Set up of phase properties.

Next, in the "Phases" panel, the materials defined in the previous step needs to be assigned to corresponding phases (**Figure A12**). According to the manual, the fluid with lower density (oil) is assigned to be the primary phase, and water is assigned to be the secondary phase (**Figure A13**). Into the "Interactions" dialog on "Phases" panel, in the "Surface Tension" tab, the "Wall Adhesion" option needs to be turned on, and a constant surface tension = 0.015 N/m is given in this example (**Figure A14**).

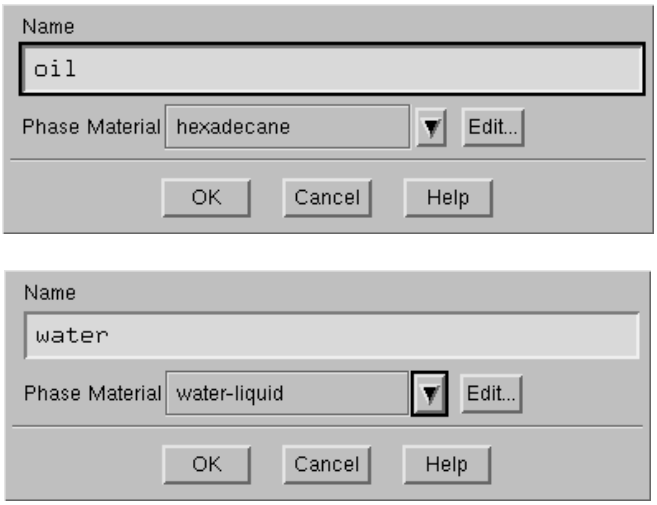

Figure A13 Assign different materials to corresponding phases.

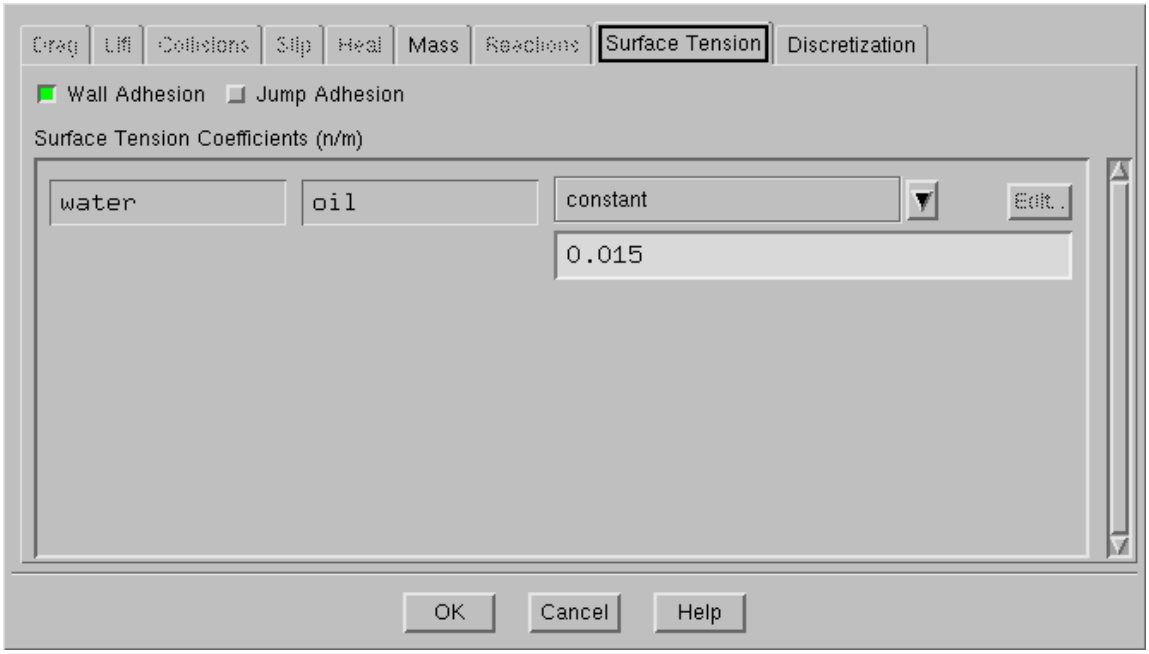

Figure A14 Setup of surface tension..

Step 6: Load user-defined function (UDF) and set user-defined scalar (UDS).

Before entering the setup of boundary conditions (BC), the user-defined function (UDF) and user-defined scalar (UDS) need to be loaded and defined at this point to provide the necessary options in BC settings (**Figure A15** and **Figure A16**). The UDF is loaded through menu: "Define" -> "User-Defined" -> "Functions" -> "Compiled" (**Figure A15**). In this example, a C source code file (see Appendix B) named "uds.c" is used, and no header file is needed. The name of the compiled library is given "libudf" here. By clicking the "Build" button, the "uds.c" will be compiled using the proper C compilers corresponding to the platform and solver settings (**Figure A17**). In this example, the C compiler is gcc (linux) 4.5.4, 64-bit version, the default hook to the FLUENT package on the Linux platform. If running on the windows platform, Visual C++ Express Edition is recommended as the compiler, and the FLUENT package is recommended to be started from a 64-bit command line prompt if the 64-bit FLUENT is used (common command line prompt in Windows is 32-bit, therefore a special command line tool, such as in .NET Framework 2.0 SDK (x64), needs to be installed). The windows system path also needs to be set correctly, such that the tool "nmake" could be found by the compiler. After compiling the UDF source code, the library is loaded by clicking "Load" button in the same dialog. The UDS is defined through menu: "Define" -> "User-Defined" -> "Scalars" (**Figure A16**). One UDS is defined in this example to represent the electrostatic potential, as described in (2.16). Because in (2.16), there is no

unsteady term nor flux term, these two terms are also turned off as “none” in the settings (**Figure A18**). Other terms are kept with the default settings.

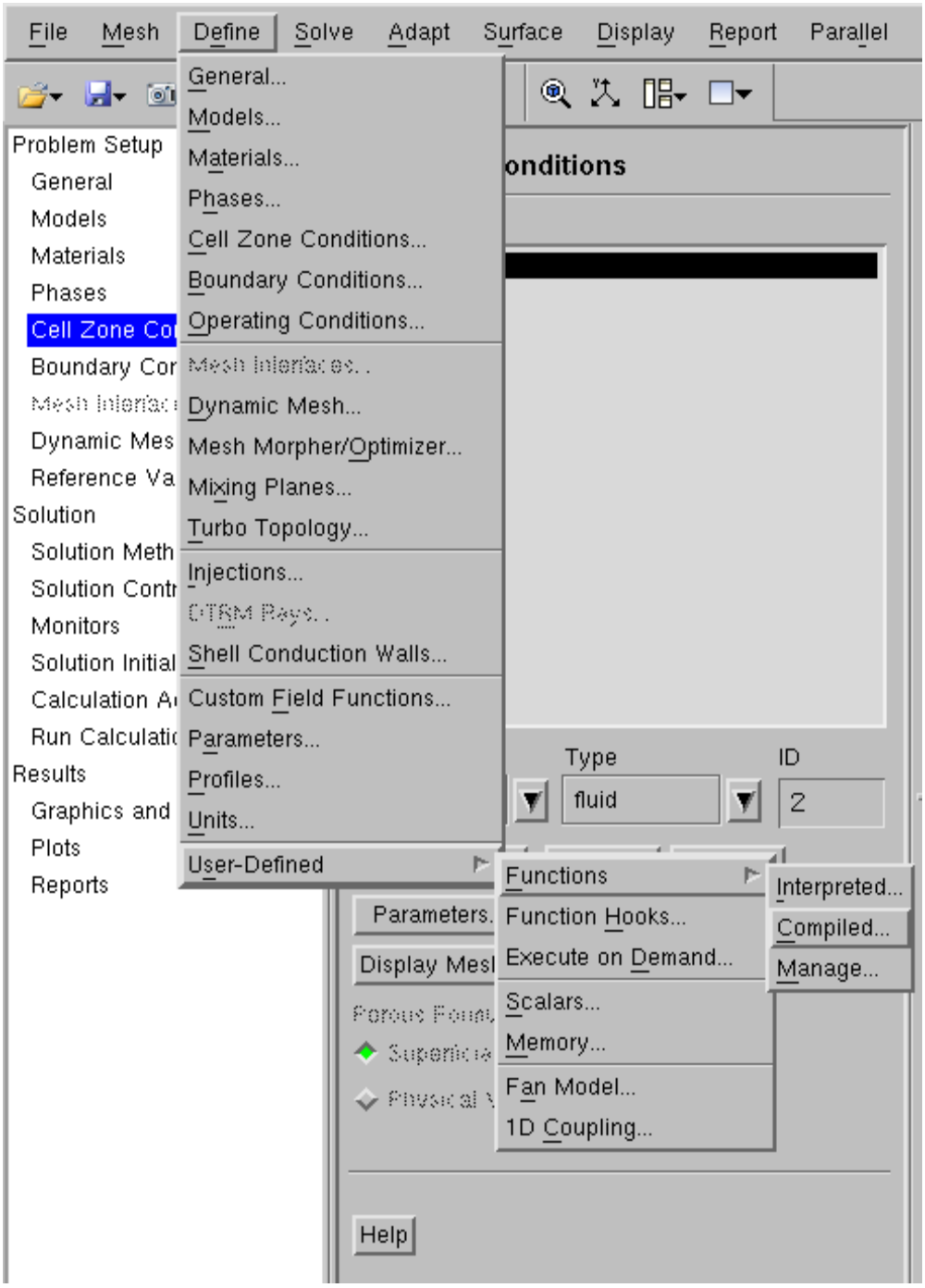

Figure A15 Load the User-Defined Function (UDF) source code.

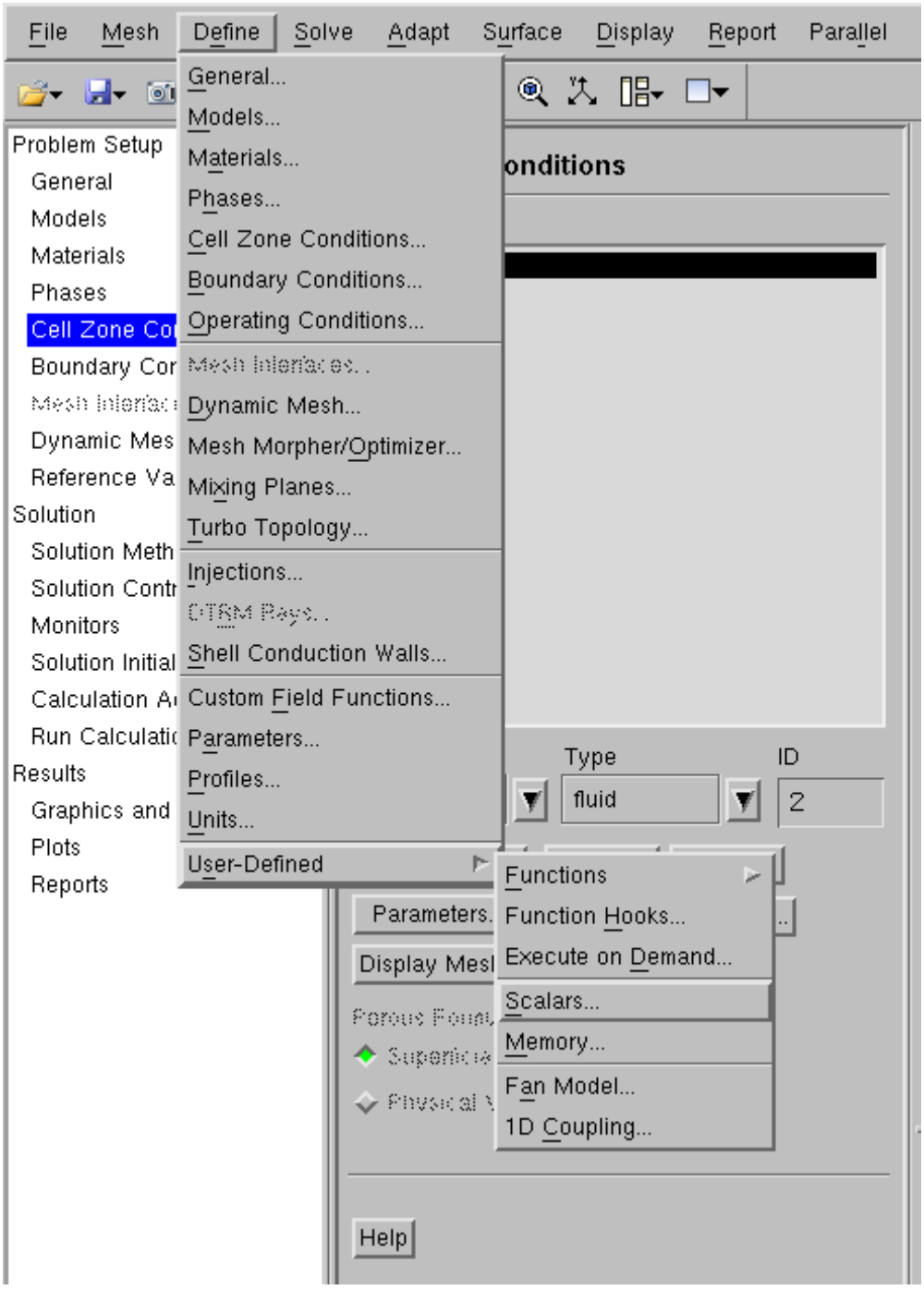

Figure A16 Add the user-defined scalar of electrostatic potential.

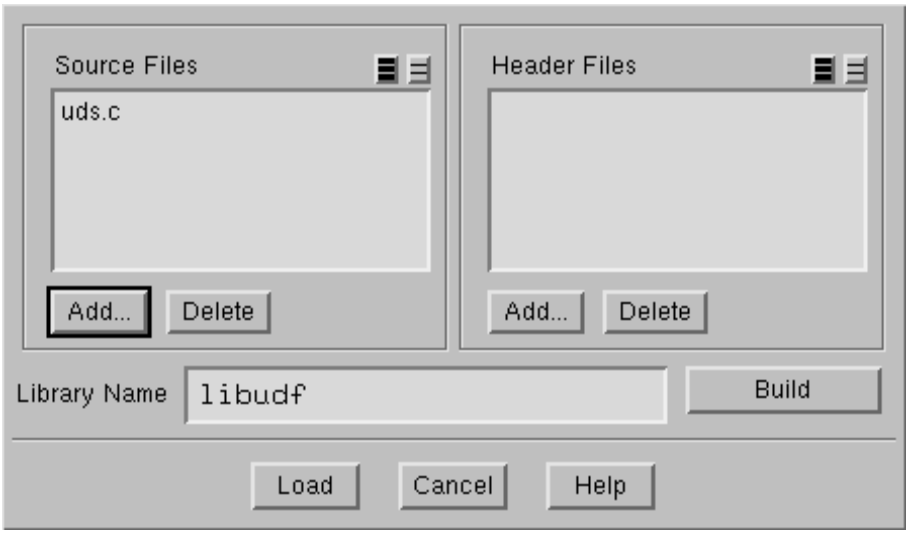

Figure A17 The UDF compiling settings.

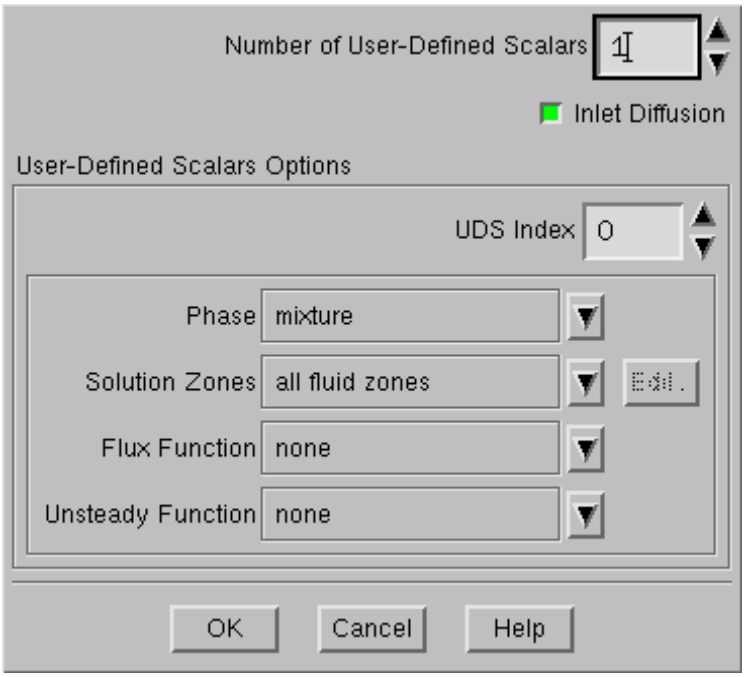

Figure A18 Details of definition of UDS.

Step 7: Set up source term in the bulk fluid properties.

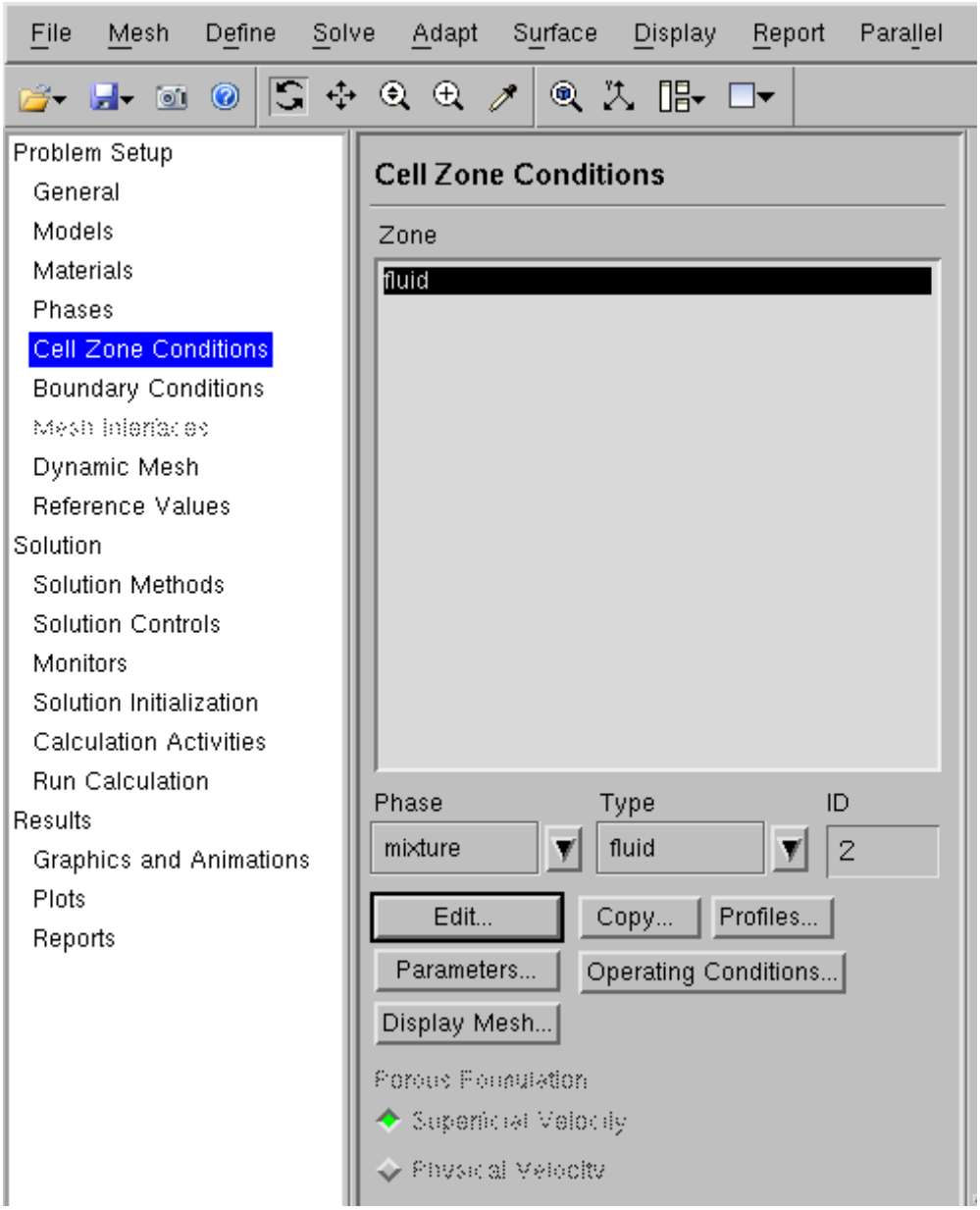

Figure A19 "Cell Zone Conditions" panel.

After defining the UDS for the electrostatic potential, the boundary conditions of the source term is defined in the "Cell Zone Conditions" panel as shown in **Figure A19**. First, the "Source Terms" is turned on in the "Edit" dialog of bulk cells, then switching to the "Source Terms" tab. By default, no source term is defined. In this example, a force density source ("udf force_dens::libudf") is calculated by the UDF and added to the momentum term in all directions, as shown in **Figure A20**. Similarly, a source term is also needed for the just-defined UDS, which is given "udf phi_source::libudf" as shown in **Figure A21**.

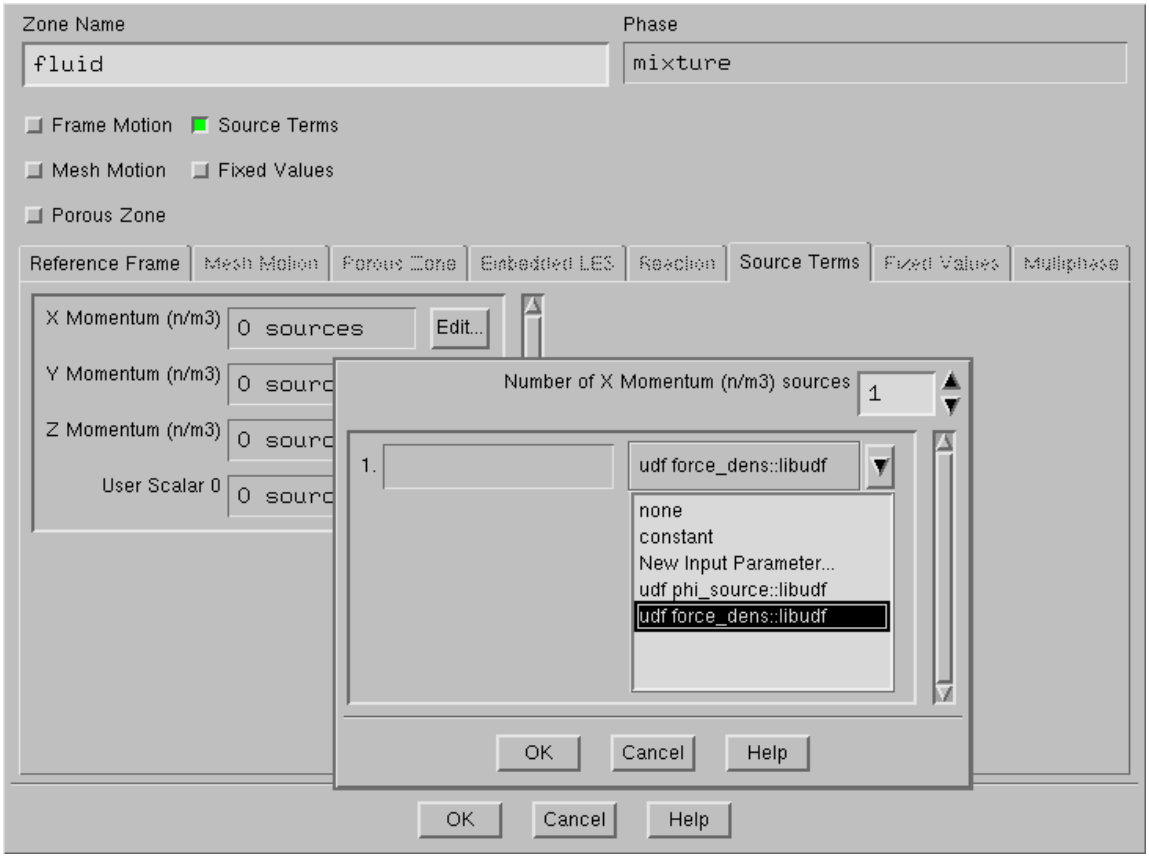

Figure A20 Define force density source in momentum terms.

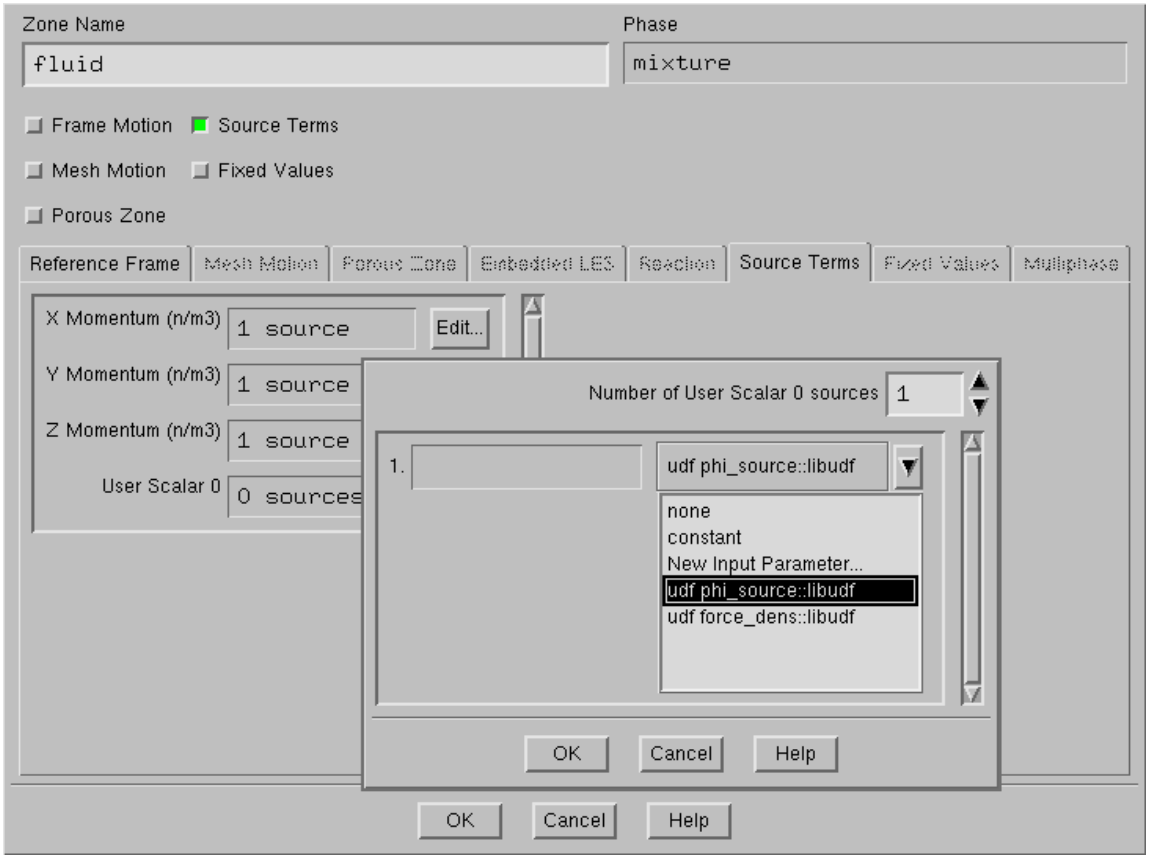

Figure A21 Define UDS source in UDS terms.

Step 8: Set up boundary conditions.

In the "Boundary Conditions" panel (**Figure A22**), different BCs are defined according to **Table 4**. Due to the definition of UDS, a zero-value BC is defined in the "UDS" tab on all interfaces except for a zero-flux BC defined on the outlet (**Figure A23**). Generally speaking, most of the BCs are defined in the "mixture" phase, except for the water inlet, of which an extra BC needs to be defined on "water" phase to set the inward flow as secondary phase (water) (**Figure A24**).

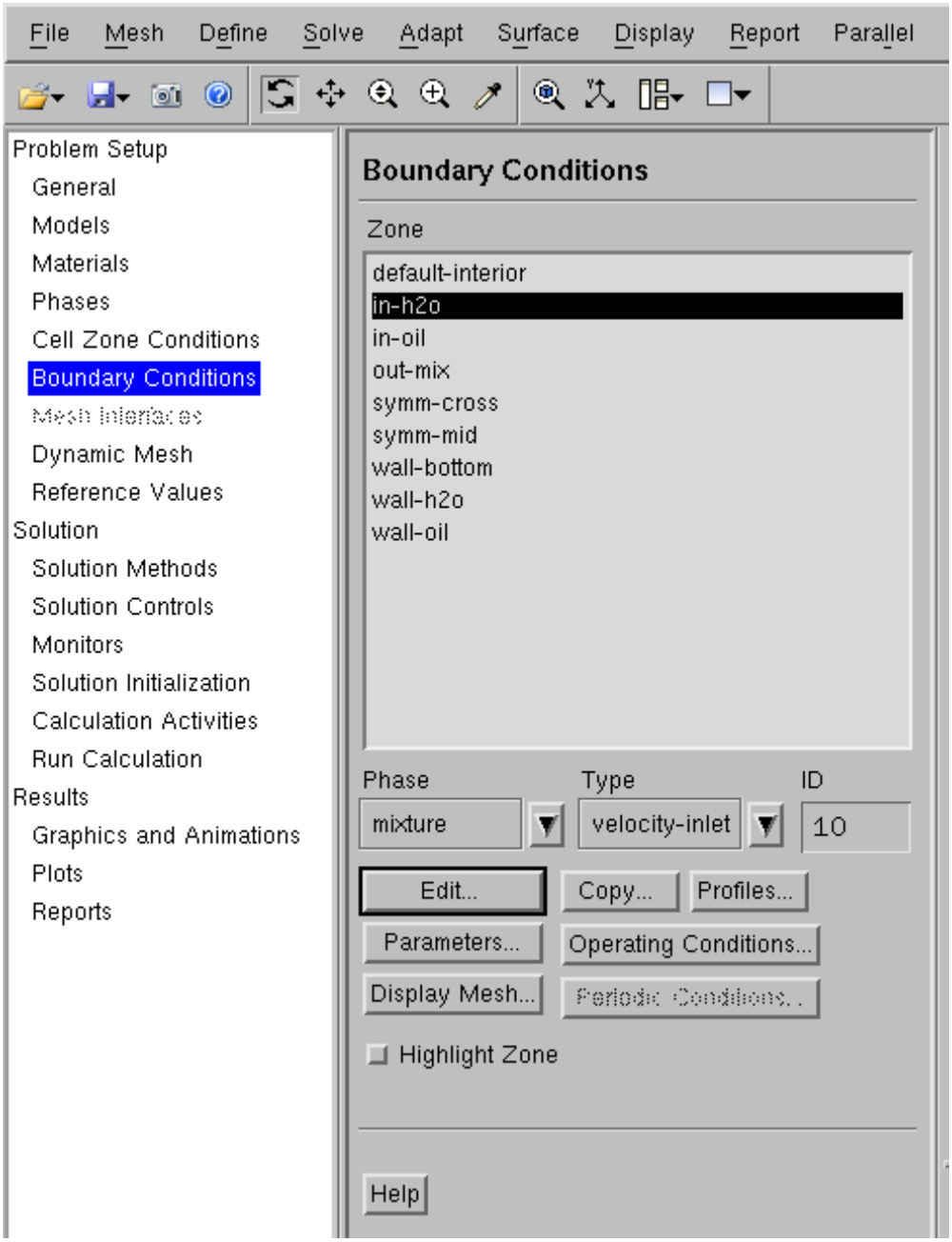

Figure A22 "Boundary Conditions" panel.

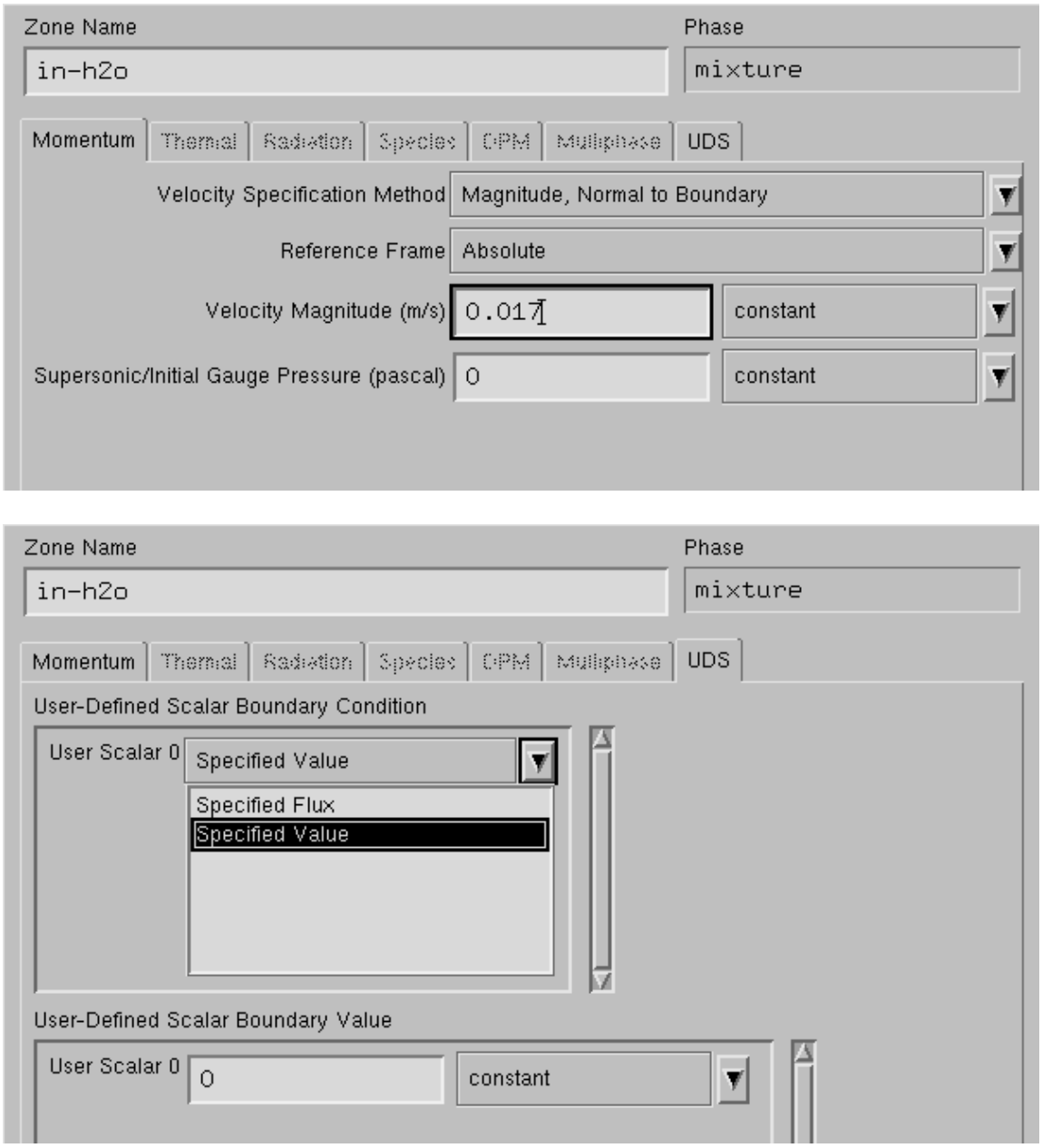

Figure A23 Definition of boundary condition on the water inlet (mixture phase).

Figure A24 Definition of boundary condition on the water inlet (water phase).

Step 9: Set up solver.

In **Figure A25** the details of solver settings are illustrated as summarized in **Table 4**. The pressure-velocity coupling scheme is set to be Pressure-Implicit with Splitting of Operators (PISO), which features two additional corrections, neighbor correction and skewness correction, besides the pressure-correction. The additional corrections take a little more CPU time for per iteration but significantly decrease the number of iterations required to reach convergence, hence increase the calculation efficiency. The skewness-neighbor coupling option is mainly helpful to meshes with high degree of skewness. For the orthogonal mesh used in this example, there is no significant efficiency or accuracy loss with this option turned off. The spatial discretization schemes are set as Green-Gause cell based scheme for gradient, PREssure STaggering Option (PRESTO!) scheme for pressure, Second-Order Upwind scheme for both momentum and UDS, and Geo-Reconstruct scheme for Volume Fraction. The transient formulation is automatically set to first-order implicit scheme as a limitation of VOF method implemented in FLUENT. The settings of under-relaxation factors are shown in **Figure A26**, where the default settings are used in this example. The change in the "Advanced Solution Controls" dialog is shown in **Figure A27**, where most settings are left to the default values except that the "Smoother Type" is changed to "ILU" from "Gauss-Seidel" to improve the accuracy and efficiency for multiphase simulation.

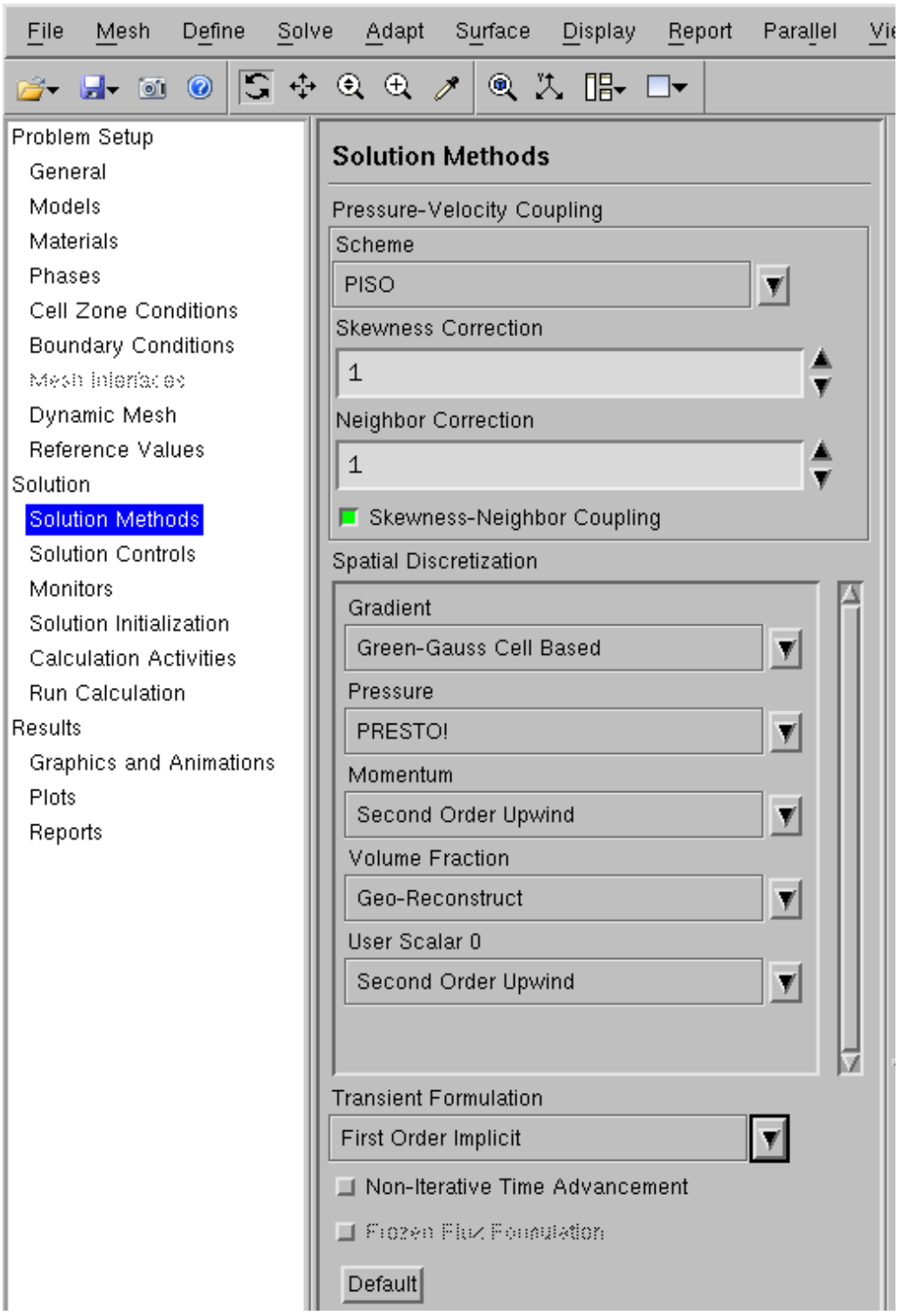

Figure A25 Details of solver settings in "Solution Methods" panel.

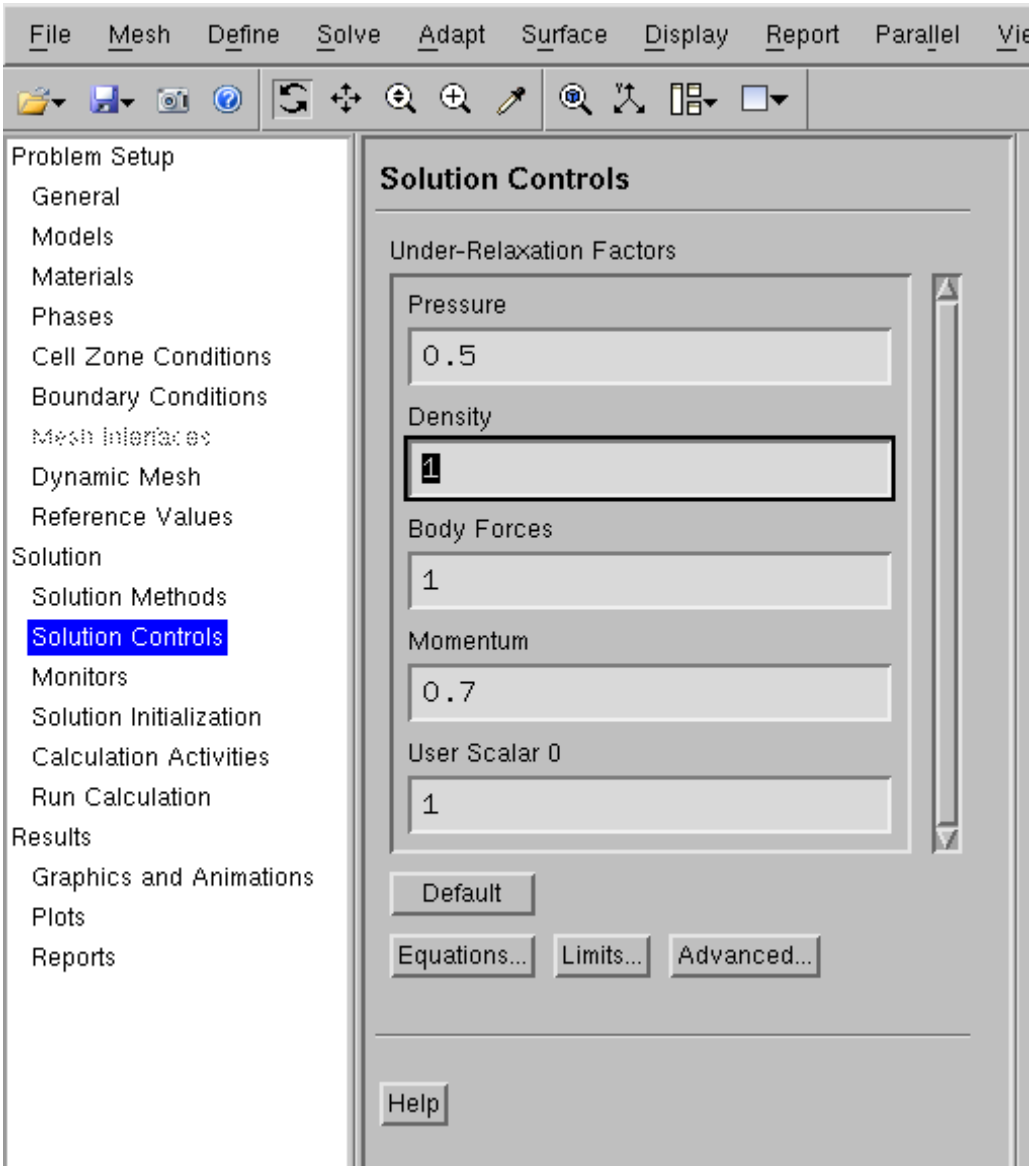

Figure A26 Details of under-relaxation factors setting in “Solution Controls” panel.

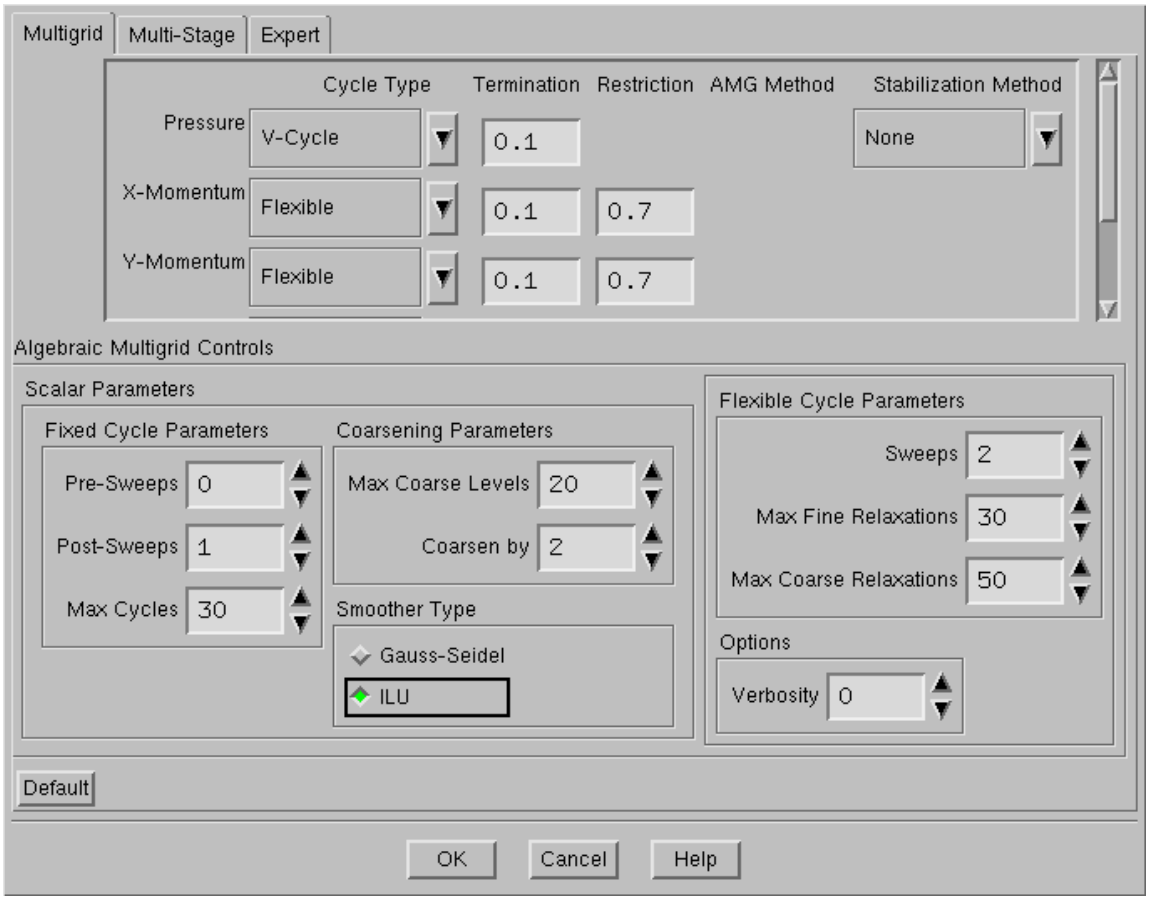

Figure A27 Details of settings in "Advanced Solution Controls" dialog.

Step 10: Set up convergence monitor.

After the setting of solution methods and controls, the iteration and convergence monitor are set in the "Monitors" panel, as shown in **Figure A28**. The plot function is turn off to save the system resource and improve the calculation running efficiency. Convergence criteria are set to 0.000001 for continuity variable, 0.00001 for all velocity variables, and 0.001 for UDS, according to the trial and error in the iteration process. It is worth noticing that the residual may shows oscillation during the iterations, as it is not

the absolute criteria to determine the end of simulation as in the steady simulations, but no significant divergence in residual should happen in the process, either.

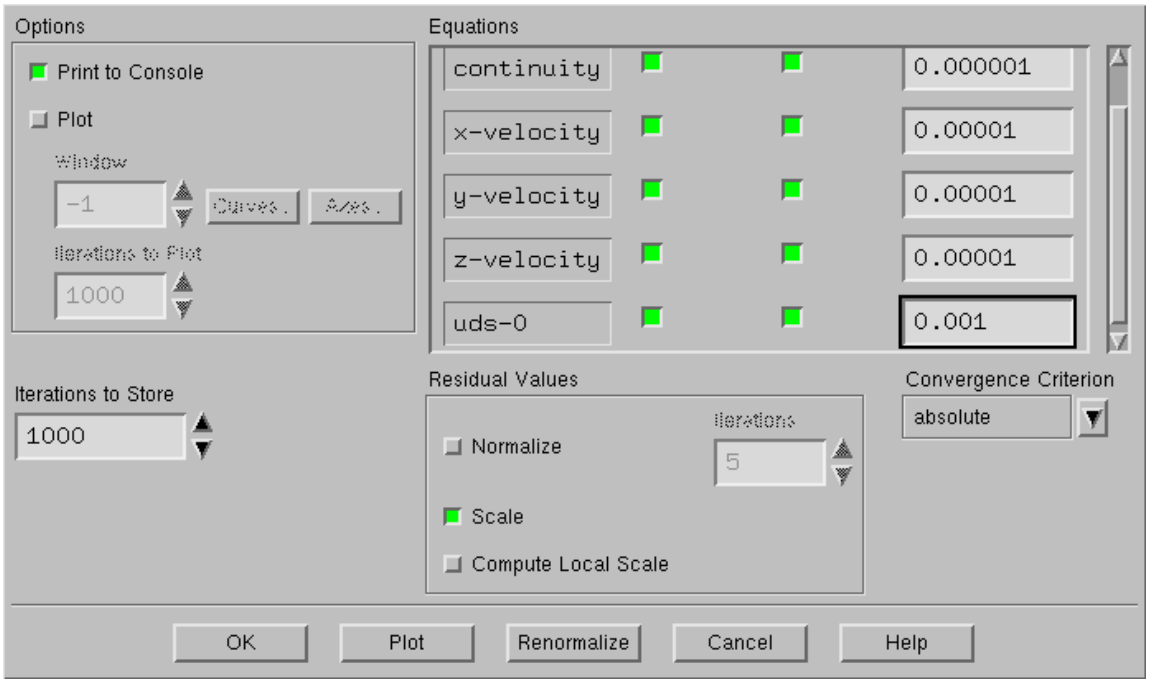

Figure A28 Details of the convergence monitor settings.

Step 11: Initialization and patch.

With all the model setup finished in the previous steps, the flow field in the mesh is initialized using default values as shown in **Figure A29**. To expedite the simulation progress in the initial stage, the region in the water inlet channel is patched to fill up with water fluid. The mark-up of this region is shown in **Figure A30** and **Figure A31**, and the marked region is patched with water (volume fraction of water = 1) as shown in **Figure A32**, and the patched result is illustrated in **Figure A33**.

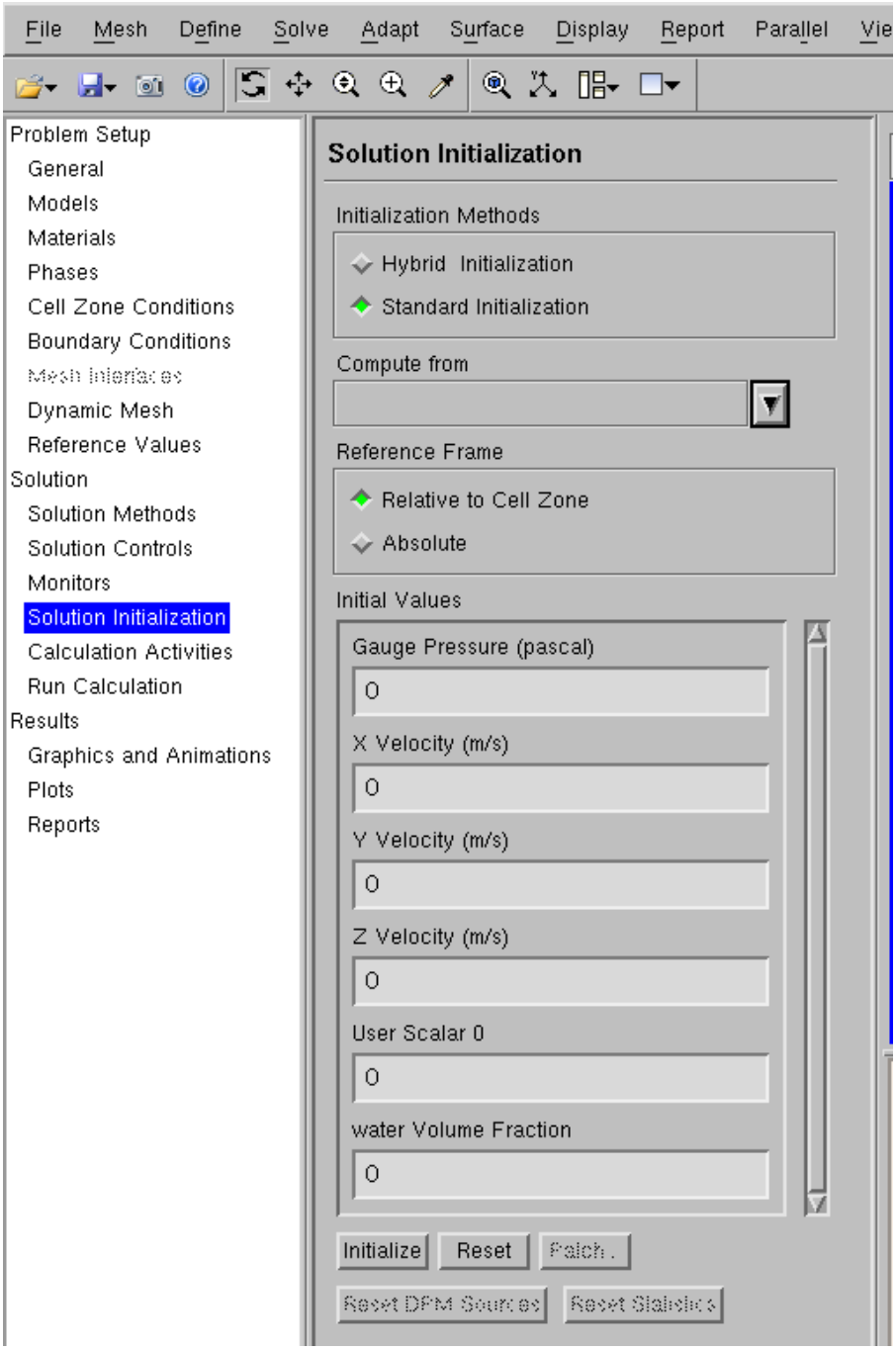

Figure A29 Details of initialization settings in “Solution Initialization” panel

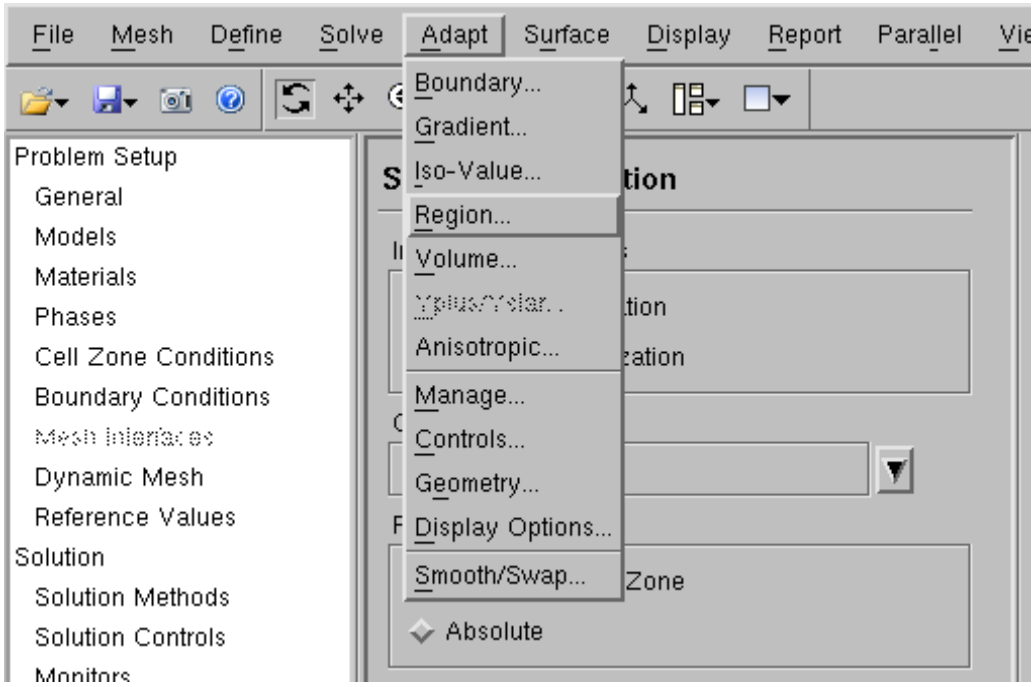

Figure A30 Selection of menu item to mark region for patch on the water inlet region

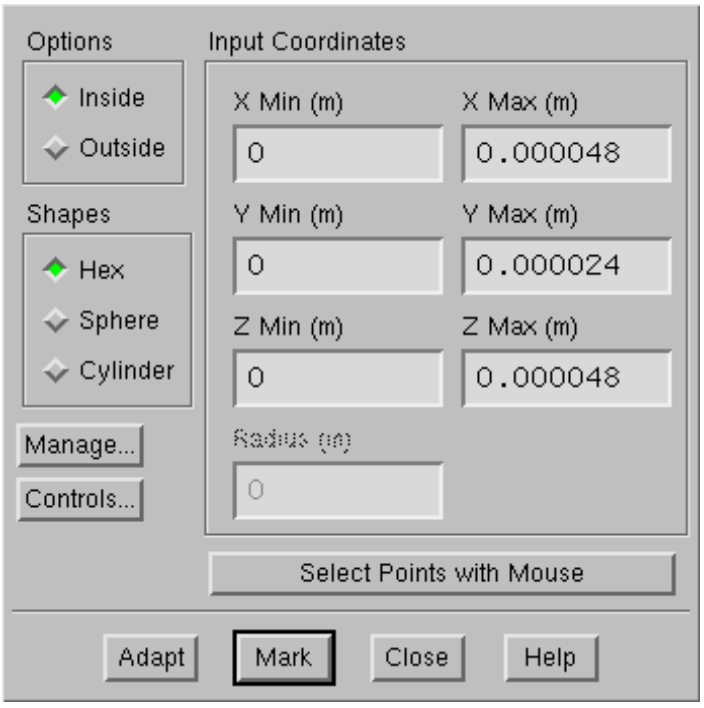

Figure A31 Details of marking the hexagonal region for patch in the water inlet

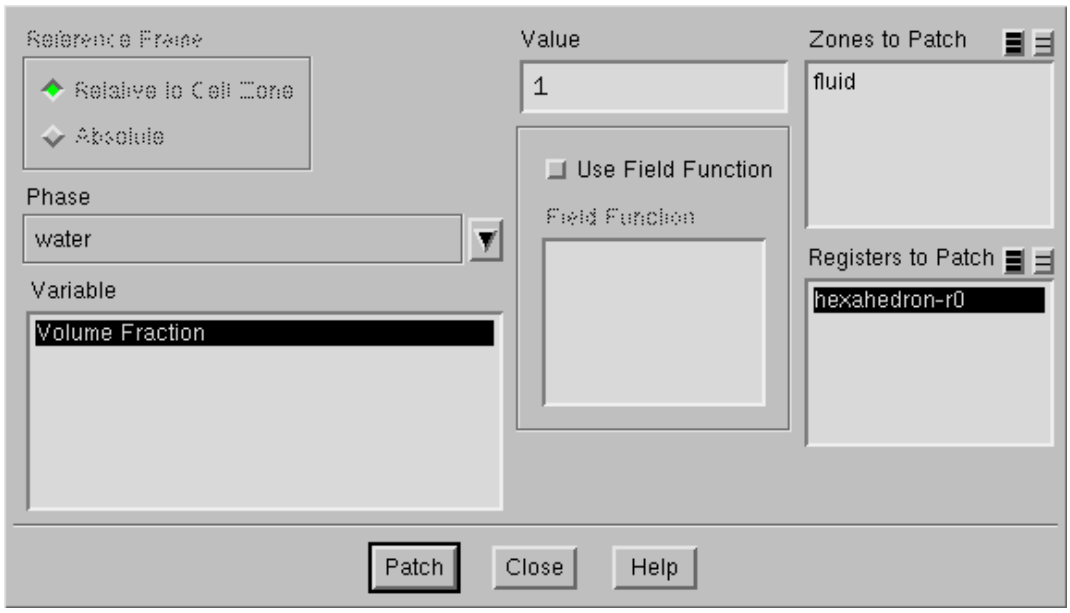

Figure A32 Details of patching the marked region in the water inlet.

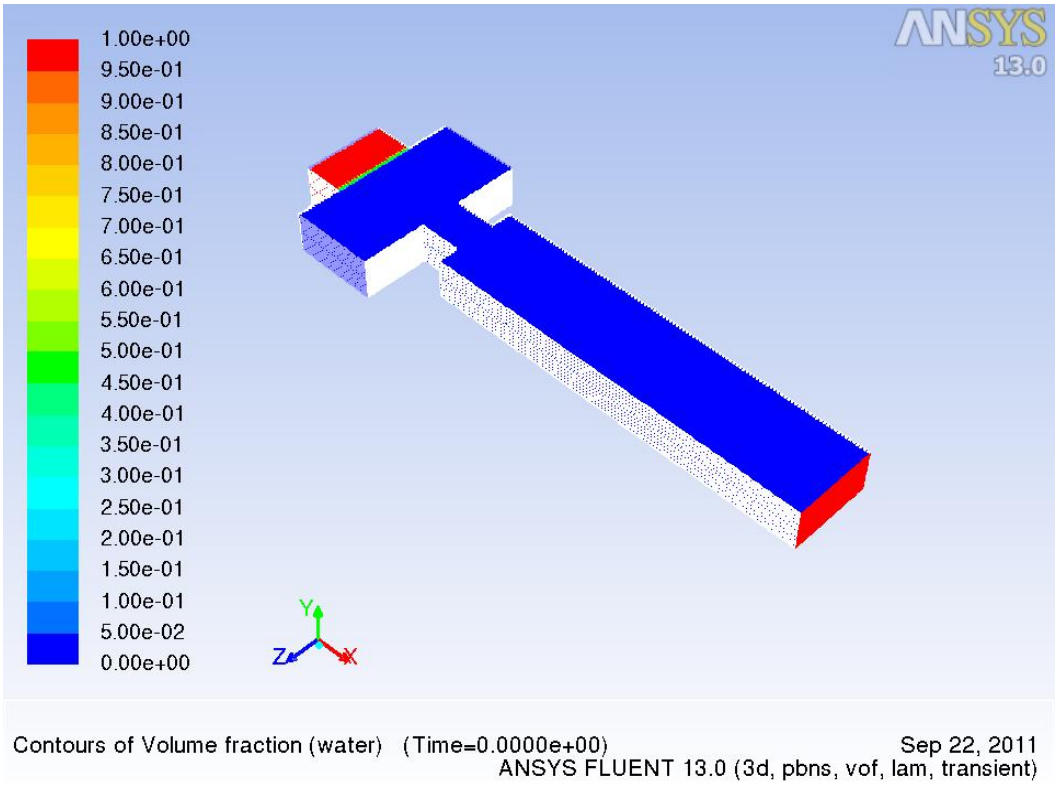

Figure A33 Illustration of initialized simulation case with patch in water inlet.

Step 12: Set up the iteration parameters.

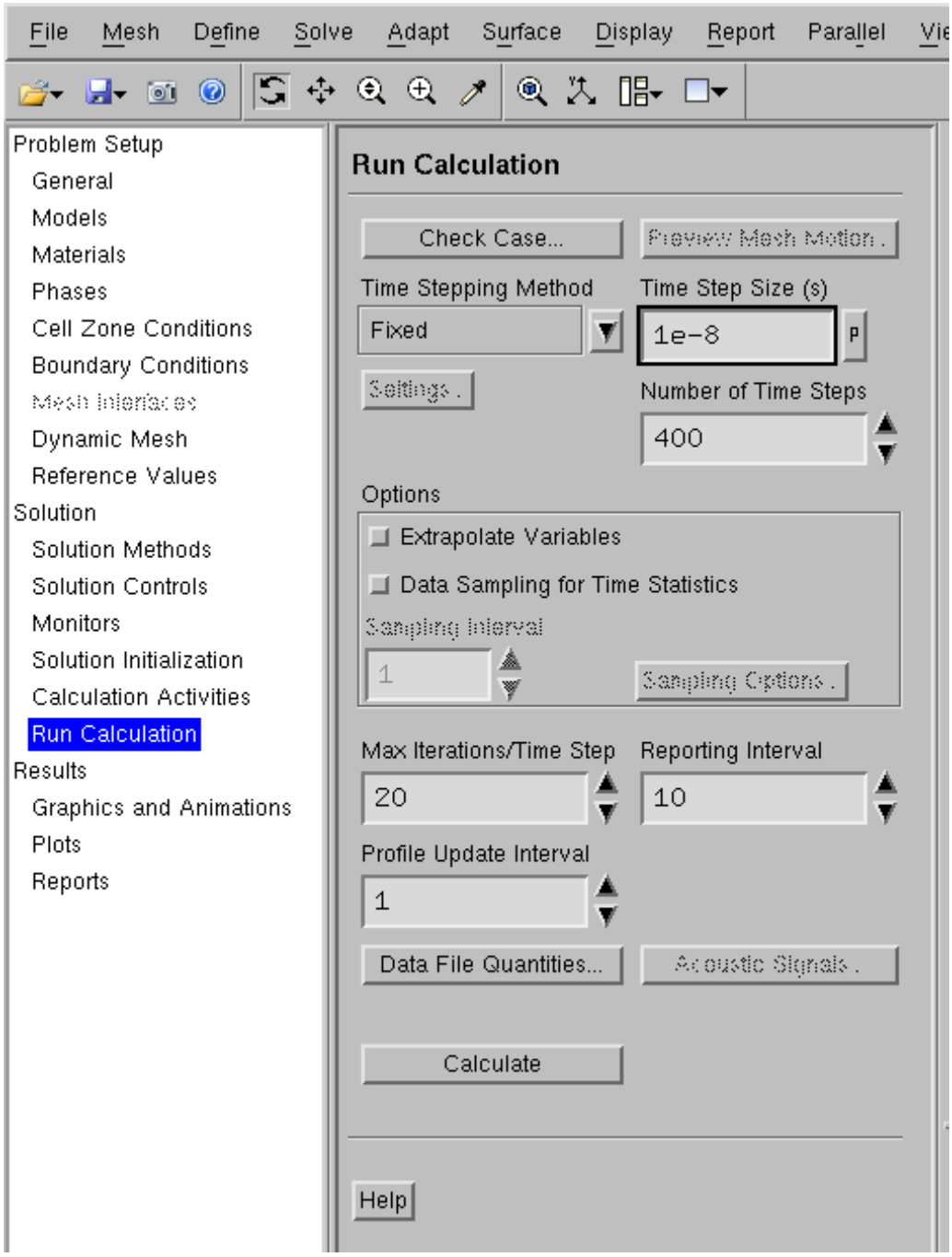

Figure A34 Details of settings for initiating the simulation run with fixed time-step.

Finally, the iteration setting of the simulation case is finished in the "Run Calculation" panel. To reduce the excess output information, the reporting interval is set to be 10 time steps, in order to expedite the iteration. The running is initiated with small fixed time-step such as 1e-8 seconds to stabilize the iteration (**Figure A34**). After several hundreds of steps, the time-step is gradually increased by factor 2-5 until 4e-6 second. When the iteration process is basically stabilized, according to the residual output report, the iteration process is switched to variation time-step method, as shown in **Figure A35**. The global courant number is limited to 0.5, and the maximum time-step size is limited to 4e-6 second, to maintain the accuracy of iteration while keeping the simulation in a fast pace. In the end, the simulated case and data file need to be automatically saved to avoid loss of results.

Figure A35 Details of settings of running simulation with time-step variation methods

APPENDIX B

FLUENT User-Defined-Function (UDF) Code

The following c code is used as UDF in FLUENT simulation to express the electrostatic repulsion force, as shown in equations (2.16).

```
/* BEGIN OF SOURCE CODE */

#include "udf.h"

  DEFINE_SOURCE(phi_source,c1,t1,dS1,eqn1)
  {
    double source_phi, rho0, rho;
    Thread *t2;

    t2 = THREAD_SUB_THREAD(t1, 0);

    rho0 = 0.001;

    /* source term for the UDS,
       rho = rho0 * Heaviside(f - 0.5)
    */
    if (C_VOF(c1,t2)<0.5)
      rho = rho0;
    else
      rho = 0.0;

    /* UDS convection equation,
       ∇²(phi) = k²*phi - rho
    */
    source_phi = 2.5e8*C_UDSI(c1,t1,0) - rho;
    dS1[eqn1] = 2.5e8;

    return source_phi;

  }

  DEFINE_SOURCE(force_dens,c,t,dS,eqn)
  {
    double source_f, phi0, f_source;

    phi0 = 2.4E-15;
    f_source = 1.8E7;

    if (fabs(C_UDSI(c,t,0))<phi0)
      source_f = 0.0;
```

```
    else if (C_UDSI(c,t,0)<0)
      source_f = -f_source;
    else
      source_f = f_source;

    /* define a constant force */
    dS[eqn] = 0.0;

    return source_f;
  }

/* END OF SOURCE CODE */
```

APPENDIX C

GAMBIT Scripts For Mesh Generation

The following scheme script is used in GAMBIT software package to generate the flow-focusing channels used in Appendix A.

```
/ BEGIN OF SCRIPT
/
/ Journal File for GAMBIT 2.4.6, Database 2.4.4, ntx86 SP2007051421
/ Identifier "Normal"
/
/ Creation of vertex. V0X are vertex in the lower plane,
/ and V1X are the corresponding vertex in the upper plane.
/
vertex create "V01" coordinates 0 0 0
vertex create "V11" coordinates 0 24 0
vertex create "V02" coordinates 0 0 48
vertex create "V12" coordinates 0 24 48
vertex create "V03" coordinates 48 0 48
vertex create "V13" coordinates 48 24 48
vertex create "V04" coordinates 48 0 100
vertex create "V14" coordinates 48 24 100
vertex create "V05" coordinates 148 0 100
vertex create "V15" coordinates 148 24 100
vertex create "V06" coordinates 148 0 24
vertex create "V16" coordinates 148 24 24
vertex create "V07" coordinates 196 0 24
vertex create "V17" coordinates 196 24 24
vertex create "V08" coordinates 196 0 48
vertex create "V18" coordinates 196 24 48
vertex create "V09" coordinates 640 0 48
vertex create "V19" coordinates 640 24 48
vertex create "V0A" coordinates 640 0 0
vertex create "V1A" coordinates 640 24 0
/
/ Creation of edges. E0X are edges in the lower plane,
/ E1X are edges in the upper plane, and EhX are vertical edges.
/
edge create "E012" straight "V01" "V02"
edge create "E023" straight "V02" "V03"
edge create "E034" straight "V03" "V04"
edge create "E045" straight "V04" "V05"
edge create "E056" straight "V05" "V06"
edge create "E067" straight "V06" "V07"
edge create "E078" straight "V07" "V08"
edge create "E089" straight "V08" "V09"
```

```
edge create "E09A" straight "V09" "V0A"
edge create "E01A" straight "V01" "V0A"



edge create "E112" straight "V11" "V12"
edge create "E123" straight "V12" "V13"
edge create "E134" straight "V13" "V14"
edge create "E145" straight "V14" "V15"
edge create "E156" straight "V15" "V16"
edge create "E167" straight "V16" "V17"
edge create "E178" straight "V17" "V18"
edge create "E189" straight "V18" "V19"
edge create "E19A" straight "V19" "V1A"
edge create "E11A" straight "V11" "V1A"
edge create "Eh1" straight "V01" "V11"
edge create "Eh2" straight "V02" "V12"
edge create "Eh3" straight "V03" "V13"
edge create "Eh4" straight "V04" "V14"
edge create "Eh5" straight "V05" "V15"
edge create "Eh6" straight "V06" "V16"
edge create "Eh7" straight "V07" "V17"
edge create "Eh8" straight "V08" "V18"
edge create "Eh9" straight "V09" "V19"
edge create "EhA" straight "V0A" "V1A"
/
/ Creation of faces. FXY are faces between EhX and EhY,
/ F-bot is the bottom surface, and F-top is the top surface.
/
face create "F12" wireframe "E012" "E112" "Eh1" "Eh2" real
face create "F23" wireframe "E023" "E123" "Eh2" "Eh3" real
face create "F34" wireframe "E034" "E134" "Eh3" "Eh4" real
face create "F45" wireframe "E045" "E145" "Eh4" "Eh5" real
face create "F56" wireframe "E056" "E156" "Eh5" "Eh6" real
face create "F67" wireframe "E067" "E167" "Eh6" "Eh7" real
face create "F78" wireframe "E078" "E178" "Eh7" "Eh8" real
face create "F89" wireframe "E089" "E189" "Eh8" "Eh9" real
face create "F9A" wireframe "E09A" "E19A" "Eh9" "EhA" real
face create "FA1" wireframe "E01A" "E11A" "EhA" "Eh1" real
face create "F-bot" wireframe "E012" "E023" "E034" "E045" "E056" "E067" \
  "E078" "E089" "E09A" "E01A" real
face create "F-top" wireframe "E112" "E123" "E134" "E145" "E156" "E167" \
  "E178" "E189" "E19A" "E11A" real
/
/ Creation of the body of mesh.
/
volume create "Vbody" stitch "F12" "F23" "F34" "F45" "F56" "F67" "F78" \
  "F89" "F9A" "FA1" "F-bot" "F-top" real
undo begingroup
```

```
/
/ Mesh the edges, faces and body of mesh with uniform size 2
/
edge picklink "E012" "E023" "E034" "E045" "E056" "E067" "E078" "E089" \
  "E09A" "E01A" "E112" "E123" "E134" "E145" "E156" "E167" "E178" "E189" \
  "E19A" "E11A" "Eh1" "Eh2" "Eh3" "Eh4" "Eh5" "Eh6" "Eh7" "Eh8" "Eh9" \
  "EhA"
edge mesh "EhA" "Eh9" "Eh8" "Eh7" "Eh6" "Eh5" "Eh4" "Eh3" "Eh2" "Eh1" \
  "E11A" "E19A" "E189" "E178" "E167" "E156" "E145" "E134" "E123" "E112" \
  "E01A" "E09A" "E089" "E078" "E067" "E056" "E045" "E034" "E023" "E012" \
  successive ratio1 1 size 2
undo endgroup
face mesh "F12" "F23" "F34" "F45" "F56" "F67" "F78" "F89" "F9A" "FA1" \
  "F-bot" "F-top" submap size 2
volume mesh "Vbody" submap
/
/ Set boundary physical types
/
physics create "In-H2O" btype "VELOCITY_INLET" face "F12"
physics create "In-Oil" btype "VELOCITY_INLET" face "F45"
physics create "Wall-H2O" btype "WALL" face "F23"
physics create "Wall-Oil" btype "WALL" face "F34" "F56" "F67" "F78" "F89"
physics create "Out-Mix" btype "PRESSURE_OUTLET" face "F9A"
physics create "Symm-Mid" btype "SYMMETRY" face "FA1"
physics create "Wall-Bottom" btype "WALL" face "F-bot"
physics create "Symm-Cross" btype "SYMMETRY" face "F-top"
save
export fluent5 "Normal.msh"
save
/ END OF SCRIPT
```

VITA

Peng He received his Bachelor of Engineering degree in thermal science and energy engineering from The University of Science and Technology of China in 2005. He joined the chemical engineering program at Texas A&M University in September 2005 and graduated with his Ph.D degree in December 2011. His research interests include colloidal science and microfluidics.

Dr. He may be reached through his email: birdy.hp@gmail.com, or his TAMU department address:

Department of Chemical Engineering

c/o Dr. Zheng Cheng

Texas A&M University

College Station, TX 77843-3122

Publications

1. "*Surface-controlled shape design of discotic micro-particles*" Andres F. Mejia, **Peng He**, Mark Netemeyer, Dawei Luo, Manuel Marquez and Zhengdong Cheng, *Soft Matter*, 2010, (6), 4885-4894
2. "*Low-frequency AC electro-flow-focusing emulsification*" **Peng He**, Haejune Kim, Dawei Luo, Manuel Marquez and Zhengdong Cheng, *Applied Physical Letters*, 2010, (96), 174103
3. "*Hindrance Function for Sedimentation of Colloidal Disks*" **Peng He**, Andres F. Mejia, Dazhi Sun, Hung-Jue Sue, Dean S. Dinair, Z. Cheng, *Physical Review E*, 2010, (81), 026310
4. "*Uniform Discotic Wax Particle Synthesis by Electrospray Emulsification*" Andres F. Mejia, **Peng He**, Dawei Luo, Manuel Marquez and Zhengdong Cheng, *Journal of Colloid and Interface Science*, 2009, (334), 22-28
5. "*Temperature dependence of the Oregonator model for the Belousov-Zhabotinsky reaction*" S. R. Pullela, D. Cristancho, **Peng He**, K. R. Hall, and Zhengdong Cheng, *Phys. Chem. Chem. Phys.*, 2009, (11), 4236
6. "*Discotic Colloids: An emerging frontier in Colloid and Interface Science*" **Peng He** and Zhengdong Cheng, *CACS(Chinese American Chemical Society) Communications*, 2009 (Spring), 21
7. "*Drug Discovery: Advances in Microfluidics*", **Peng He**, Jingyi Shen, and Zhengdong Cheng, *Drug Discovery 2007***.**, Touchbriefings, 36